

DISSERTATION

DESIGN OF A COMPACT INTEGRATED HIGH-POWER SUPERCONDUCTING RADIO
FREQUENCY ELECTRON BEAM SOURCE AND KLYSTRON-INSPIRED TERAHERTZ
POWER SOURCE

Submitted by

Nihan Sipahi

Department of Electrical and Computer Engineering

In partial fulfillment of the requirements

For the Degree of Doctor of Philosophy

Colorado State University

Fort Collins, Colorado

Spring 2018

Doctoral Committee:

Advisor: Anthony A. Maciejewski

George J. Collins
Edwin K. P. Chong
Norm Buchanan

Copyright by Nihan Sipahi 2018

All Rights Reserved

ABSTRACT

DESIGN OF A COMPACT INTEGRATED HIGH POWER SUPERCONDUCTING RADIO FREQUENCY ELECTRON BEAM SOURCE AND KLYSTRON-INSPIRED TERAHERTZ POWER SOURCE

There exists a need for compact, reliable, high-power electron sources for applications including those in industry, basic science, medical science and security. There also exists a need for compact electron-beam based light and power sources of various power levels and at different frequencies (mm-wave to gamma rays) for applications also in the fields of basic science, industry, and security. Today's examples of high-average-power electron sources are neither very compact nor highly efficient. The same may be said for many of the electron-beam based light sources operated worldwide for a myriad of applications. Recent breakthroughs in superconducting (SC) materials technology, radio-frequency (RF) power systems, specialized cathodes, and RF cavity designs offer ways to overcome the above-mentioned shortcomings. In this dissertation, all of these new features are integrated in a comprehensive design into one promising concept for a compact superconducting RF (SRF) high-average power electron linear accelerator. This integrated design is capable of 5-50 kW average electron beam power and continuous-wave operation with the corresponding electron beam energy up to 10 MeV. In addition, the community also has a need for compact sources for many different wavelength regimes, as well as a variety of peak and average powers. Specifically, we are also exploring a novel continuous wave terahertz source designed from using basic principles of the beam manipulation methods used in free-electron laser (FEL) light sources.

ACKNOWLEDGEMENTS

I would like to thank my advisor and my committee members all their support and encouragement during my PhD studies.

I would like to thank Vyacheslav Yakovlev for his valuable guidance as being my URA advisor during my research at Fermilab. I would like to give a special thanks to Ivan Gonin for his availability to answer all of my questions during my research. Another special thanks is to Alexander Sukhanov for his valuable help on coding during my design studies. I also would like to thank Fermilab colleagues, Timergali Khabiboulline and Nikolay Solyak for the valuable discussions during my studies, and IARC and OPTT teams for their hospitalities during my stay at Fermilab.

I especially would like to thank Michael Borland and Philippe Piot for their endless help and technical discussions on my beam dynamics studies. They were always available for my questions and gave generously their time and knowledge. I also would like to thank my colleague Jonathan Edelen for his helpful discussions during my beam dynamics simulations.

I also would like to thank all of my friends for their valuable friendship during my studies and my life.

My greatest and deepest thanks are to my parents for believing in me and their invaluable support in every step of my life. This dissertation would not have been possible without your never-ending support and encouragement.

My warmest thanks is to my brother for always being there for me. I am the luckiest person in the world to have a brother like you. You have been an awesome friend and support in my life.

My grateful thanks are to my grandparents for their valuable support during my life.

My heartfelt thanks is to my love, my husband and my colleague Taylan. You always believe in me and encourage my work all the time. Thank you for your endless love and support in every second of my life.

TABLE OF CONTENTS

ABSTRACT.....	ii
ACKNOWLEDGEMENTS	iii
LIST OF TABLES.....	vi
LIST OF FIGURES.....	vii
1. INTRODUCTION	1
1.1. OVERVIEW OF CHARGED PARTICLE ACCELERATORS	1
1.2. OVERVIEW OF THE DISSERTATION.....	3
1.2.1. <i>Integrated and Compact High Average Power Superconducting Electron Source</i>	5
1.2.2. <i>Klystron-Inspired Concept for the Generation of Electromagnetic Radiation in the Terahertz (THz) Regime</i>	15
2. RADIO FREQUENCY (RF) CAVITY FUNDAMENTALS.....	20
2.1. DESIGN PARAMETERS OF AN RF CAVITY	20
2.1.1. <i>Figures of Merit</i>	22
2.2. OPTIMIZATION PARAMETERS FOR DESIGNING AN RF CAVITY	31
3. DESIGN OF A COMPACT INTEGRATED HIGH-POWER SUPERCONDUCTING RADIO FREQUENCY (SRF) ELECTRON BEAM SOURCE.....	34
3.1. ELECTROMAGNETIC DESIGN OF THE INTEGRATED SYSTEM	35
3.1.1. <i>Design of the Gun and Overall Accelerating Structure</i>	35
3.1.2. <i>Design of the Cathode Region</i>	41
3.1.3. <i>Design Combination of the Cathode and the Gun into a Single Structure</i>	48
4. BEAM DYNAMICS SIMULATIONS FOR THE INTEGRATED SRF ELECTRON SOURCE.....	51
4.1. SIMULATION RESULTS USING SMASON	52
4.2. BEAM DYNAMICS SIMULATIONS USING SPIFFE.....	55
5. DESIGN OF A COMPACT, CW KLYSTRON-INSPIRED TERAHERTZ (THZ) ELECTROMAGNETIC RADIATION SOURCE	63
5.1. THE PRINCIPLES OF A KLYSTRON.....	63
5.2. THE PRINCIPLE OF THE ECHO-ENABLED HARMONIC GENERATION (EEHG) METHOD.....	64
5.3. DESIGN OF A KLYSTRON-INSPIRED THZ SOURCE.....	69
5.3.1. <i>Adaptation of the Theory of EEHG Method into the Compact Klystron-inspired THz System</i>	70
5.3.2. <i>RF Design of the THz Klystron</i>	77
6. CONCLUSIONS.....	86
REFERENCES.....	89
APPENDIX A. ADDITIONAL DESIGN RESULTS FOR THE GUN-CELL AND OVERALL ACCELERATING STRUCTURE FOR THE COMPACT SRF ELECTRON SOURCE.....	96
APPENDIX B. ADDITIONAL DESIGN RESULTS FOR THE CATHODE ASSEMBLY FOR THE COMPACT SRF ELECTRON SOURCE.....	100
APPENDIX C. ADDITIONAL DESIGN RESULTS FOR THE INTEGRATED STRUCTURE OF FOR THE COMPACT SRF ELECTRON SOURCE.....	103
APPENDIX D. BEAM DYNAMICS SIMULATIONS USING ASTRA FOR THE COMPACT SRF ELECTRON SOURCE.....	107

LIST OF TABLES

Table 1: Analytical and SUPERFISH cavity parameter results for SRF pillbox cavity.....	30
Table 2. The design parameters of the modified (gun) cell	37
Table 3: The results of SUPERFISH for two different lengths of the first cell (0.3 and 0.4 of a full-cell length)	41
Table 4: The optimized beam parameters at the end of first cell as simulated by SMASON.	54
Table 5: Basic parameters of the System (Details to be described later.).....	74
Table 6: SW and TW cavity parameters for maximum relative velocity ($\beta = 1$)	78
Table 7: SW and TW cavity parameters for maximum relative velocity ($\beta = 0.14$)	79
Table 8: Design parameters of the π -mode standing-wave (SW) buncher cavity	81
Table 9: Design parameters of the π -mode standing-wave (SW) catcher cavity.....	81
Table 10: Design parameters of the $2\pi/3$ -mode traveling-wave (TW) catcher cavity.....	83
Table 11: The design parameters of the full system (2 buncher cavities, 1 catcher cavity and 2 drift spaces).....	83
Table 12: Input and output parameters for the THz klystron.....	84

APPENDIX TABLES

Table A 1: The results of SUPERFISH, COMSOL Multiphysics and CST MWS for two different lengths of the first cell (0.3 and 0.4 of a full-cell length). The peak fields are calculated for 10-MeV output electron beam energy.....	99
--	----

LIST OF FIGURES

Figure 1: The concept for an integrated, compact and high-average power SRF electron source. The overall length is roughly 1.5 m and the diameter is roughly 0.5 m. 11

Figure 2: Schematic of a simple pillbox cavity with length L. The cavity has an electric field along the axis, and magnetic field circulates around the axis through the cavity..... 21

Figure 3: 1.3 GHz SRF (Niobium) pillbox cavity electric field distribution..... 31

Figure 4: An elliptical cavity geometry design parameters. 33

Figure 5: a) Detailed geometry and field mapping of the 9-cell ILC – TESLA cavity b) Electromagnetic field distribution for the given geometry 36

Figure 6: The parameters of an elliptical cavity’s design geometry. The parameter values of the modified (gun) cell are given in Table 1..... 37

Figure 7: Frequency scan results of our 8.4-cell structure’s design with the embedded gun. 38

Figure 8: a) The 8.4-cell structure’s design geometry matched to the 1.3-GHz frequency and its field map in SUPERFISH b) The magnified view of the first 2 cells c) The electromagnetic field distribution of our 8.4-cell structure’s design geometry as computed by SUPERFISH. 40

Figure 9: Schematic view of the cathode assembly indicating 70K shielding and RF choke 42

Figure 10: The gating process using fundamental frequency (1.3 GHz) and second harmonic of the fundamental frequency (2.6 GHz). The blue line indicates the fundamental frequency and red line indicates the second harmonic. (x-axis indicates the time and y-axis indicates the field amplitude) 43

Figure 11: Cathode assembly design using 1.5 cm-length 70K shield wall 45

Figure 12: Cathode assembly design locating the RF choke 1 mm further than the cathode place 46

Figure 13: a) The cathode region’s design geometry at 2.6 GHz with the field generated using SUPERFISH. b) The on-axis electromagnetic field distribution of the cathode region’s design geometry used in Figure 5 as calculated by SUPERFISH. 47

Figure 14: a) The design geometry of the combined cathode and gun regions at 1.3 GHz as calculated using SUPERFISH. b) The magnified view of the cathode and the first cell regions. 48

Figure 15: a) The design geometry of the cathode and gun structures together and the results at 2.6 GHz b) The magnified view of the cathode and first cell regions when integrated as shown in Figure 18 as calculated using SUPERFISH. 49

Figure 16: The solid model of the RF Gun and the cathode region as modeled in CST MWS.... 51

Figure 17: The mesh view of the combined geometry of the cathode assembly and the gun cell in SMASON..... 53

Figure 18: The bunch length vs. relative phase (left) and the bunch rms energy spread vs. phase for the SMASON simulations..... 55

Figure 19: a) The boundary of the combined structure b) The field distribution of the combined structure in SPIFFE..... 56

Figure 20: Kinetic energy of all particles in one bunch through the combined structure (cathode and 8.3-cell geometry) 57

Figure 21: Longitudinal phase space in time for the particles in one bunch without gating process 58

Figure 22 : The snapshots of the bunch travels through the integrated structure without gating process.....	59
Figure 23: Transverse phase space at the end of the integrated structure without gating process	59
Figure 24: The kinetic energy of a bunch through the combined structure	60
Figure 25: The longitudinal phase space in time for the particles in one bunch with gating process	61
Figure 26: The snapshots of the bunch travels through the integrated structure (Red ellipse is added to this figure to indicate the traveling bunches.).....	61
Figure 27: Transverse phase space ellipse at the end of the integrated structure with gating process	62
Figure 28: Schematic of a) resonator FEL b) Self Amplified Spontaneous Emission FEL (SASE FEL) c) High Gain Harmonic Generation (HG) Method d) Echo Enable Harmonic Generation Method (EEHG).....	67
Figure 29: Scheme of the miniature THz klystron. The buncher cavities are resonant to 28.3 GHz and the catcher cavity is resonant at 198.1 GHz.	70
Figure 30: For Stupakov’s EEHG case, we illustrate the bunching factor for $k = 10$ as a function of parameter L_1 for four different values of L_2 : $1-L_2 = 1.18$, $2-L_2 = 1.25$, $3-L_2 = 1.3$, $4-L_2 = 1.35$. (as in Stupakov’s paper).....	73
Figure 31: The longitudinal phase space of an electron bunch during velocity modulation a) The phase space after interaction with the 1 st buncher cavity (28.3 GHz) b) following shearing through the 1 st drift space c) The phase space after interaction with the 2 nd buncher cavity (198.1 GHz) d) following shearing through the 2 nd drift space.....	75
Figure 32: a) The histogram of the particle distribution as shown in Figure 31 (b). b) The FFT of the particle distribution shown in (a).	76
Figure 33: a) The histogram of the particle distribution as shown in Figure 30 (d). b) The FFT of the particle distribution as shown in (a).	77
Figure 34: Shunt impedance versus frequency scaling of SW and TW structures for $\beta = 1$ and $\beta = 0.14$	79
Figure 35: a) The 2-cell geometry of 1 st and 2 nd (identical) buncher cavity designs and b) the field distribution (operating as first buncher cavity in our configuration) operating at 28.3 GHz in the π -mode	80
Figure 36: a) The 3-cell geometry of catcher cavity design b) the field distribution (operating as first buncher cavity in our configuration) operating at 198.1 GHz in the $2\pi/3$ -mode in travelling-wave (TW) structures.....	82
Figure 37: Theoretical small-signal gain for THz klystron	84
Figure 38: AJDISK small-signal gain results	85

APPENDIX FIGURES

Figure A 1: a) The 8.4-cell structure’s design geometry with the frequency matched to 1.3 GHz and its field map as generated in COMSOL Multiphysics. b) The electromagnetic field distribution of the 8.4-cell structure’s design geometry as generated in COMSOL Multiphysics.	96
Figure A 2: a) The 8.4-cell structure’s design geometry with the frequency matched to 1.3 GHz and the contour plot of the fields using CST MWS b) The 8.4-cell structure’s design geometry with the view of the fields in the π mode using CST MWS. c) The electromagnetic field	

distribution of the 8.4-cell accelerating section’s design geometry as determined with CST MWS.	98
Figure B 1: a) The cathode region’s design geometry at 2.6 GHz and field map (in logarithmic scale) using COMSOL Multiphysics. b) The on-axis electromagnetic field distribution of the cathode region’s design geometry.....	101
Figure B 2: a) The cathode region’s design geometry with the frequency matched to 2.6 GHz and the contour plot of the fields as generated in CST MWS. b) The electromagnetic field distribution of the cathode region’s design geometry as shown in Figure 13 as generated in CST MWS....	102
Figure C 1: a) The geometry of the integrated cathode and accelerating structure at a frequency of 1.3 GHz as simulated with COMSOL Multiphysics. b) The magnified view of the cathode and first cell connection c) The field distribution for the design geometry	104
Figure C 2: a) The geometry and frequency (at 2.6 GHz) of the integrated cathode and accelerating structure as simulated with COMSOL Multiphysics. b) The magnified view of the integrated cathode and first cell in order to enhance the field map in the cathode region as calculated with COMSOL Multiphysics. c) The electromagnetic field distribution of the full system geometry	106
Figure D 1: Transferred SUPERFISH Field Distribution into ASTRA as the external field – zoomed on cathode and first 3 cells field as the cathode field is smaller than the cavity field. .	108
Figure D 2: a) The momentum of the reference particle along the z-axis. The final energy is 10 MeV at the end of 9 th cell and b) The average energy of the beam along the z-axis. The final energy is 8.14 MeV at the end of the 9 th cell.	110
Figure D 3: a) The longitudinal phase space of the bunches at z=1.5m. b) The projection of the first bunch’s phase space in Figure D 3 (a).....	111
Figure D 4: The average energy of the beam along the z-axis. The final energy is 9.49 MeV at the end of 9 th cell.....	112
Figure D 5: a) The longitudinal phase space of the bunches, b) projection of the longitudinal momentum of Figure D 5 (a).	113

1. INTRODUCTION

1.1. Overview of Charged Particle Accelerators

There are many thousands of particle accelerators in operation worldwide. The particle beams from these systems are used either directly or indirectly for a variety of applications such as illnesses diagnostics and treatment, ion implantation for industrial applications, X-ray lithography, and archeology etcetera. [1].

Particle accelerators, in general terms, can be described as systems that use the principles of electricity and magnetism to accelerate and guide charged-particle beams. The type of charged-particle beam and characteristics of the beam are defined by the specific applications. Depending on the application, electrons or protons are typically the particle of choice, while others might require something even more exotic such as a gold nucleus, in nuclear physics, for example. Further, the application dictates the method of charged particle acceleration. These methods include electrostatic, magnetic induction, or radio frequency (RF) based resonant acceleration. Electrostatic – or DC - accelerators use static electric fields to accelerate particles. Examples of electrostatic acceleration include the $\sim 10 \text{ keV}^1$ electron guns that used to be found in cathode ray tubes and older style television sets and many of today's high-power RF devices, such as klystrons. These and related electrostatic devices are generally limited to a maximum kinetic energy of a few MeV, where electrical breakdown is the primary, limiting obstacle. Further, once the electrostatic potential is achieved, passing it again through the same electrostatic field cannot further accelerate

¹ 1 eV is the kinetic energy added to a charged particle with a charge equal to that of an electron ($1.6 \times 10^{-19} \text{ C}$) when it has been accelerated across 1 volt of potential.

a particle, thus limiting the maximum achievable kinetic energy obtained from a fixed potential. This is the direct result obtained from Faraday's law of induction.

$$\nabla \times E = -\frac{\partial B}{\partial t} \quad \text{or} \quad \oint_{\partial \Sigma} E \cdot dl = -\frac{d}{dt} \iint_{\Sigma} B \cdot dS$$

If there is no change in time, then the integral of the electric field around any closed path must equal zero. If we want to use a fixed device to repeatedly accelerate a charged particle then there must be variation in the fields. To overcome this limitation, other concepts have been invented. With their varying fields, acceleration by magnetic induction or oscillating RF fields are the principal means to accelerate charged particles to significantly higher energies.

Once the particle beam is accelerated, it is usually used in a couple of distinct ways. The first approach is direct; the beam is guided to a target of choice and used for whatever purpose intended. An example of this approach is the use of protons for cancer treatment. Here, protons are directed into a tumor. The energy they release during the interaction with electrons and collisions with nuclei can break chemical bonds and therefore kill the cancerous material.

The second approach is to use manipulation of the electromagnetic fields of the beam. The power in the beam is converted to electromagnetic energy at some frequency in the electromagnetic spectrum and is then used for some specific purpose. In this case, electrons are principally used. The accelerated high-energy electrons emit electromagnetic (EM) radiation that is referred to as synchrotron radiation. The spectrum of this EM radiation can extend well into the hard x-rays and has been proven to be extremely useful in discovery science among other things.

In this dissertation, we explore two different electron accelerator systems, one that utilizes the electron beam directly in the generation of x-rays and the other where the fields of the beam are used to generate electromagnetic radiation at terahertz frequencies. The common point of these two topics is that the basic concepts in accelerator design are used or re-purposed to create novel systems for a variety of applications.

1.2. Overview of the dissertation

The above briefly described particle accelerators in a basic way with a couple of examples to give a sense of the machines and their use. In this dissertation, however, we are specifically concentrating on the research to enable two types of sources, each of which will be discussed in detail:

- The first area of research is the investigation of a novel and compact means of generating high-average power electron beams at multi megaelectronvolt (MeV) energies.
- The second research area is to use electrons to generate a source of electromagnetic radiation in the Terahertz (THz) frequency regime.

Since both of these devices use electrons, this dissertation will be limited to discussions of electron accelerators. Further, both of these subjects have elements of DC and RF acceleration (or deceleration), or in other words, energy exchange.

In an electron accelerator, the electron source is one of the most basic components. It consists of a cathode emitter and provides initial acceleration to the electrons. Since it both generates the electron beam as well as provides some initial acceleration, the electron source itself can be

described as an accelerator. Usually, however, the electron source is coupled with other accelerating structures, such as resonant cavities driven by RF fields, to achieve even higher electron energies, where the final kinetic energy is chosen depending on the application. Just as accelerators were categorized by their mode of acceleration, electron sources can be described by whether they employ DC or RF acceleration. Also, the mode of acceleration of the electron source - DC or RF - might differ from the rest of the accelerator, assuming the gun is indeed coupled to another device for further acceleration.

In the first part of this dissertation, we study on the electron-beam requirements needed for, as an example, an industrial application of accelerators which require a high-average power electron beam driver [2]. Since one of these requirements is to reach electron-beam energies of ~ 10 MeV, we chose and will employ RF acceleration. Further, since one of the other requirements is to efficiently achieve high-average electron beam powers, we also choose to employ superconducting RF (SRF) acceleration, to be described in more detail below. Another requirement of this device is compactness. This unique combination of challenging requirements has motivated us to develop a novel solution employing new technologies and concepts described herein.

While in our particular case the system goal is the destruction of organic compounds in industrial waste-water effluents, there are many other potential uses for such high-power electron accelerators. Examples include radiation cross-linking of plastics and rubbers; radiation driven chemistry; food preservation; sterilization of medical instruments; sterilization of animal solid or liquid waste.

The second part of this dissertation describes another electron device innovation. Using the architecture commonly associated with long-wavelength (1 mm to 100 μm) electromagnetic radiation emitting device – that of a klystron (to be described in detail later) – we have designed a continuous wave (cw), mid-wavelength – Terahertz (THz) - emitting device. Our klystron-inspired system is promising to enable the usage of the higher-power THz sources for many applications including those in industrial, security and the basic science settings.

1.2.1. Integrated and Compact High Average Power Superconducting Electron Source

To best describe the first part of the research, we can break down a particle accelerator into two distinct parts for the purpose of clarifying the acceleration process – the particle source which provides the particles (in our case electrons) and the initial acceleration, and the subsequent main accelerator.

The electron source (or an electron gun) refer to the region that the electrons are emitted as the cathode. The most commonly used electron guns in electron-driven devices are those with thermionic cathodes followed by electrostatic acceleration. These are maybe most well-known for being used in cathode-ray tubes (CRTs) found in older television sets, computer displays, and oscilloscopes. These were critical parts of the television industry and large television manufacturers, some had an entire division dedicated to electron guns [3]. Today their use in these devices is quite limited, but they continue to be used in devices i.e. microwave linear beam vacuum tubes such as klystrons, inductive output tubes, traveling wave tubes, and gyrotrons, as well as in scientific instruments such as electron microscopes and, in our specific area, particle accelerators.

While thermionic sources have been used primarily with electrostatic accelerators, as will be seen later, they are just as capable of operating in time-varying accelerating fields.

As mentioned in the previous section, electron guns (and accelerators) may be classified by the type of electric field generation (DC or RF) used to provide the initial kinetic energy to the beam. Electron guns, specifically their cathodes, can also be characterized by its emission mechanism (thermionic as mentioned above, photocathode, field emission and plasmas source, etc.). Moreover, the RF accelerators can be classified by their type of RF material properties – either normal-conducting or super-conducting, details of which to be described later in the dissertation.

The first part of this dissertation is about the generation of high-average power electron beams for a specific application. Although normal-conducting RF (NCRF) electron guns and electron accelerating structures have both performed well in pulsed applications with lower repetition rates, achieving high-average powers is a challenge. Due to its intrinsic high-conductivity and ease of fabrication, normal-conducting RF accelerating cavities are typically made of copper. However, even though the conductivity is high, the average ohmic losses become excessive if we attempt to operate them at high repetition rates to generate high-average beam powers. This large amount of RF power dissipation means large amounts of thermal energy translating into a need for a large cooling water system to avoid damage to the cavities. An attractive solution to this problem is to consider making the RF cavities from superconducting materials. Very little RF power is then needed to achieve very high RF fields.

First of all, however, such a system must be held at incredibly low temperature to remain in the superconducting state. This implies significant infrastructure to achieve and maintain these low temperatures and any additional heat must be removed to prevent a sudden loss of the superconducting state (referred to as quenching). Significant power loads on the surface such as an electron beam loss or a heat source can cause a quench of the SRF system. Furthermore, impurities in the materials (typical SRF systems use niobium as the SC material) disrupt the SC state again making the SRF system susceptible to quenching. It is also difficult and costly to procure, machine and polish pure niobium. SRF therefore seems at least as complicated as NCRF system. Some recent improvements in SRF, relevant to enabling our compact, high-average power source concept, however, have made SRF a more attractive and realistic option. Since we are interested in higher-average power electron beams (those at high repetition rates), we have chosen to examine an SRF gun and accelerating structure as opposed to the NCRF system. SRF accelerating devices offer great promise for high-average current operation, but as you will see, the choice of SRF, particularly for the electron gun, is a major challenge.

In the design process of an RF accelerator, a major design choice is RF frequency. Although the choice of RF frequency is really dependent on the application, based on technical limitations, there are also other limits to the choices. Industry, for instance, has developed a limited number of RF sources based on market demands and it is a costly effort to re-develop a source at even a slightly different frequency. Further, the RF sources and peripheral components at large facilities are often recycled to reduce the cost of a new machine. So based on availability of a frequency and financial resources, the choice is often a balance of technical specifications as well as what is sitting on a shelf.

On the other hand, in the case of SRF there is a broad sweet spot in frequency. If the RF frequency increases, the size and weight of an SRF accelerator decreases. However, as the frequency increases, the SRF cryogenic cooling requirements also increase and get larger. This leads to larger cryogenic systems that without additional technological advances outpace the gains in going to higher RF frequencies. Until recently, the approach was to adopt low RF frequencies (~350 MHz) that in turn lead to large physical size and weight for the cavities, cryomodule, and the required radiation shielding because of the beam energies (When the beam energy is higher than 10 MeV, the neutron production occurs). Fortunately, due to several recent breakthroughs, low cryogenic loss elliptical cavities operating at a resonant RF frequency of either 650 MHz or 1.3 GHz are now viable and excellent choices that can be used to create more compact and efficient systems. Our study is to focus on a design at 1.3 GHz as there are available, cost effective RF sources at this frequency.

There are several examples of electron guns where the advantages of superconducting technology are used. The most well-known SRF electron guns were developed at Brookhaven National Laboratory (BNL) in New York, USA [4,5], the Helmholtz-Zentrum Berlin-HZB (Berlin, Germany) [6,7], the Helmholtz-Zentrum Dresden-Rossendorf-HZDR (Rossendorf, Germany) [8,9] and at Beijing University (China) [10]. Even though all these SRF electron guns have elliptical cavity structure, the cell numbers in use for acceleration and their final electron energies are different. There is, however, another common technology has been used in these types of guns. Their emission types are photocathode emission. This means that a separate laser system has been dedicated to emit the particles from the cathode surface. Since the size of the laser system only itself is around ~ 10s of square feet, the full systems are not in compact scale. Another example of

an SRF gun is the quarter wave resonator at Niowave Inc. This structure is an example of an integrated system. However, the emission type is also photocathode emission [11]. There is an additional study that is about to use thermionic emission with an SRF elliptical cavity structure but the cathode assembly is separate from the rest of the accelerator [12].

Unfortunately, these guns have not achieved the average power levels that we demand for our application with a compact footprint. Our engineering goal, as will be seen again later, will be to combine these two components (an integrated gun and main accelerator) to achieve higher power levels and make the subsequent system compact at the same time.

In our novel, envisioned design, the SRF system is inherently complex, but we have gathered a few recent enabling technologies and have included them in our overall system concept. These include the following.

- *A new Niobium processing technique* developed at Fermilab that allows us to achieve unprecedented Q_o (performance) values in superconducting RF cavities translating into very low losses and high efficiencies [13]. This opens up the possibility to operate such a cavity with cryo-coolers as the cooling requirements are only a few Watts. We can then do away with the costly and complex helium inventory and refrigeration system found on typical SRF systems.
- Fermilab has also developed *a new injection-locked magnetron RF source* and has tested this on a single, 2.45-GHz SRF cavity. The results show excellent amplitude and phase stability [14,15]. It has a very high efficiency (80%) and therefore a low cost per watt of operation. This RF source can be utilized to help drive the overall cost of such an

accelerator down to acceptable values. Furthermore, as the system architecture is standalone the cavity frequency is allowed to vary over time. As long as the RF system can track the frequency then the system continues to work. This greatly simplifies operation as microphonic-induced frequency changes do not need to be corrected. Members of our team are adapting this to 1.3 GHz through internal and SBIR funding in order that it is ready for test and integration in the coming years.

- Another innovation produced at Fermilab is the very *low heat leak fundamental power coupler* that would be used to input the primary RF power to the cavity [16]. Such a coupler should be able to sustain 10s of kW average power from the magnetron and waveguide into the SRF accelerator structure/cryomodule while nearly eliminating any heat load on the cooling system.
- Advances in understanding thermionic and field emission cathodes, in particular the potential to gate or limit their emission to acceptable phase values, invites the use of a *robust cathode system* in the SC environment. Indeed, this is one of the most significant challenges and in this dissertation we will show the challenge is solvable.

By combining the above technical advancements into the robust physics and engineering design described herein, a compact system similar to what is seen in Figure 1.1 can be realized [17].

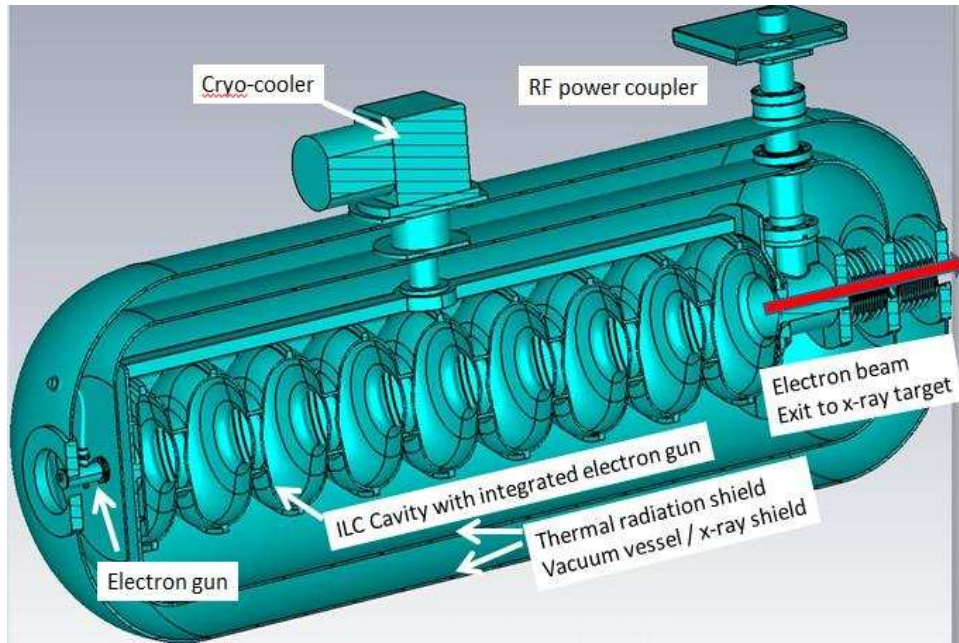


Figure 1: The concept for an integrated, compact and high-average power SRF electron source. The overall length is roughly 1.5 m and the diameter is roughly 0.5 m.

Such a compact system is certainly possible; however, there are many obstacles that still must be overcome to achieve such an integrated and functional design. This is the primary focus of the first part of dissertation – to come up with an integrated system architecture of a compact, high-power electron source and then focus on the difficult issues to find workable solutions.

In this dissertation, our concentration has been on devising the cathode region design based on physics and engineering principles, coupling this design into an RF cavity acceleration structure, and building a parameterized model of this system. We have integrated the cathode, electron gun, and main accelerator into one fully integrated component as well as ensured that proper gating of that cathode limits any beam loss through the system that would have the deleterious effects described above. In this integration step, the design of the cathode assembly and the gun cell (1st

cell of a 9 cell accelerator structure) is not only novel and a key part of the full system, it is critical for achieving stable intensity and high-average power.

In our concept, we chose to use a 9-cell standard accelerating structure that was originally developed for the TeV–Energy Superconducting Linear Accelerator (TESLA), which is a superconducting electron–positron collider of initially 500 GeV total energy, extendable to 800 GeV, and an integrated X–ray laser laboratory at DESY, Germany [18]. This structure is also called ILC/XFEL cavity since it uses for International Linear Collider and European X-Ray Free Electron Laser machines [19,20]. The ILC/XFEL accelerating structure which has separate electron gun system utilizes an elliptical RF cavity profile that is fabricated with high-purity niobium and operates at 2 K. This structure is designed to run at a resonant RF frequency of 1.3 GHz and represented a good starting point for our design.

Our integrated concept was designed in a couple of steps. First, the first of the nine cells needed to be reduced in length. The reason for this is simple. The length of a full cell is chosen assuming the velocity of the electrons are near the speed of light; however, upon emission off the cathode in this integrated concept, the electron’s velocity is very low and it takes some time/distance to reach relativistic velocities. This necessitates a shortened length for the first cell.

We have therefore re-designed the first cell of the 9-cell ILC/XFEL structure, shortening the first cell to 0.4 (or in a later study 0.3) times the length of the standard cell. Typical maximum field gradients generated in the cathode cell (~ 15 MV/m to 20 MV/m) then accelerate the electrons from rest to speed greater than 0.9 times the speed of light over a broad range of starting phases.

The overall structure length is then 8.4 times the length of one regular ILC/XFEL cell and so we refer to this as an 8.4-cell accelerating structure that have the cathode integrated directly into the first (gun) cell that is 0.4 (or 0.3) times the length of a regular cell. For future reference, the length of a regular cell is equal to 11.53 cm which can be easily calculated by using

$$L_{cell} = \frac{c}{2f} \quad (1)$$

where c is the speed of light and f is the resonant frequency of the accelerating structure.

For this present work, a majority of the detailed design work was performed in the cathode region. As mentioned earlier, one of the novel parts of the concept is the design of the cathode assembly and coupled this part into the gun cell. Our desire is to produce a robust system, and to do this we propose to do something that at first looks uncommon. We have chosen to integrate directly into the first cell of the 4 K superconducting RF structure a thermionic cathode operating at temperature > 1000 K. Not only this is a delicate balance on how to shield the heat from the SRF cavity, but the common emission properties of a thermionic cathode are also not directly compatible with the SRF environment. Electrons are freely emitted from a thermionic cathode whenever the field at the cathode is favourable, which if nothing is done is during one half of the RF cycle. If we do not employ a solution to gating the electrons, some electrons will be emitted at unfavourable phases and will potentially strike the cold superconducting surfaces or back bombard the cathode. Those that strike the SC surfaces will create heat loads that could result in a quench of the system, and those that back bombard the cathode could heat the cathode to a level that results in a thermal runaway condition. Even a small loss of electrons to the SC walls of the accelerating structure could easily quench the structure and must be avoided. Clearly attaching a thermionic cathode to a SC accelerator is a very challenging process requiring a careful design.

Our solution to this challenge is to gate the electrons off the cathode over the RF phase range that will allow the electrons to be accelerated and transported out of the end of the accelerating structure without even striking the cold SC structure walls. This will be accomplished by adding an additional resonant cavity right at the cathode. This cavity will be operated at twice the fundamental frequency (in this case 2.6 GHz). The cathode will also be DC biased relative to the zero crossing of the second harmonic field. This combination, a second harmonic field with a DC bias, will allow us to gate the electrons off of the cathode. A small iris between the cathode region and the gun cell will allow the electron to enter the main accelerating region. By proper phasing between the second harmonic and fundamental frequency, the electron can be accelerated without loss. Addition to this design, an RF choke has been added between the 0.4 length cell and the cathode. This prevents the fundamental field from inadvertently influencing the gating process. The iris plate also acts as a 70 K heat shield that will both intercept stray electrons as well as shadow the cathode from the SC surfaces.

In summary, this design allows us to gate electrons out of the cathode region and into the fundamental primary accelerating RF electromagnetic field (1.3 GHz) over a phase range that will allow for full transport of the electrons through the accelerator without losses to the SC walls or undesirable back bombardment to the cathode.

In the first part of dissertation we will detail the above compact and integrated SRF high power electron gun/accelerator system including the electromagnetic design of highly specialized gun cell and cathode region and a novel technique of integrating a thermionic cathode into the superconducting accelerating structure. In addition, we will also present the particle tracking

studies which assess the beam properties through the entire designed system with a design goal of generating an electron beam power of at least 3 kW and up to 10-MeV beam energy. This fully-integrated system is contained within a footprint smaller than classical designs as it eliminates certain infrastructure by capitalizing on new innovations.

1.2.2. Klystron-Inspired Concept for the Generation of Electromagnetic Radiation in the Terahertz (THz) Regime

New advances in different electromagnetic radiation source technologies have made the previously underutilized terahertz (THz) electromagnetic frequency band more accessible than before for a wide range of applications. The so-called ‘terahertz gap’ has a frequency range from 0.3 THz up to 3 THz in the electromagnetic spectrum, or in other words between microwave and far infrared frequencies. As an example of the use of a THz source, consider spectroscopy. In the THz range, spectrographic techniques can be used in, for instance, detecting defects in pharmaceutical tablet coatings, product inspection in industry, chemistry, astronomy, material characterization (physics) and the detection of skin cancer. Despite the long list of applications, this region of the electromagnetic spectrum is still one of the most unexplored and underutilized. One of the main reasons is that even though there are few compact sources of higher power available at THz frequencies, they are not capable in achieving the high powers in broadband range [21].

The second part of this dissertation explores a novel tunable electron-device concept intended to produce significant power in the THz-frequency range. Our focus is on generating and accelerating an electron beam, but this time, rather than trying to produce a high-energy and high-power electron beams for generating x-rays, we instead want to generate an electron beam of fairly low

energy (non-relativistic in fact), manipulate it and generate electromagnetic radiation at THz frequencies. We do this in a device with a configuration similar to a multi-cavity klystron.

A “classical klystron” is in simple terms a device that amplifies an RF signal by extracting power from an energetic electron beam. Russell and Sigurd Varian developed the klystron idea in 1935, and first tested it in 1937 [22]. In the most basic klystron concept, there are two microwave cavities – called the buncher and the catcher, respectively. It is a microwave device, and uses the principle of bunching and phasing of the electron beam relative to an electromagnetic wave. It is a narrow-band power amplifier typically operating in the range of Ultra High Frequency (UHF- hundreds of MHz) up through hundreds of GHz.

Examples of application areas of the usage of klystrons are radar, satellite and television broadcasting, medicine (radiation oncology), particle accelerators, etcetera. Klystrons are popularly used for many different applications since their efficiency is very high (up to 80 % of input wall-plug power can be converted to RF power) and they are highly reliable - typically operating for many years without intervention.

Looking at a klystron in more detail [23], an electron beam is generated in a typical DC thermionic gun with electrostatic focusing described above. An RF cavity is excited to some chosen field level by an input signal. This is the input signal to the amplifier. The DC electron beams interact with RF fields as it passes through this resonant cavity. The electron beam upon passing through the fields of this RF cavity, called the buncher cavity, acquires a sinusoidal energy modulation, which due to the non-relativistic nature of the low-energy beam is equivalent to a sinusoidal velocity

modulation. Following the buncher, the velocity modulated electron beam travels through a drift space. During this time the higher velocity electrons catch up with the low velocity electrons causing a density modulation of the beam at the frequency of the input signal. This bunched beam is then directed through another resonant RF cavity called the catcher cavity that is tuned to the input frequency. In the catcher cavity, the bunched electron beam resonantly drives the fields in the cavity and the electrons give up their large kinetic energy to the RF electromagnetic fields of the catcher cavity. This power is then out-coupled for use elsewhere.

Our study in the second part of this dissertation is about the design of a klystron-inspired device that is efficient, robust and capable in achieving THz frequencies. We have set out to test a concept already explored in the short wavelength electromagnetic radiation production regime (VUV to soft X-rays); however, we have adapted it to the long wavelength regime.

Our original concept to increase the output frequency of the klystron into the Terahertz regime was to adapt the principles of beam manipulation methods used in the electron-beam-based, short-wavelength, and free-electron laser (FEL) light source community which we called Echo-Enabled Harmonic Generation (EEHG) and this is what we will explore.

The echo-enabled harmonic generation method [24] is a laser-assisted electron-beam manipulation scheme designed to produce high-harmonics in the electron beam density distribution for the generation of short-wavelength radiation. This method is used to up-frequency convert the energy density modulation of an electron beam in the free-electron laser (FEL) process. Since it was conceived for the FEL, it implicitly assumes a relativistic electron beam and also generates

subsequent EM radiation in an unguided environment (no waveguide). Using the same concept, but in our case employing velocity modulation of non-relativistic electron beams driving resonant RF cavities much like a klystron, we have designed a device that can generate high amounts of sub – THz frequency radiation power in a compact structure that is a few centimeters in length.

In its simplest concept, we use a klystron configuration with the catcher cavity tuned to a significantly higher harmonic of the buncher. This allows us to use conventional, electromagnetic radiation sources in the microwave regime as the input signal as these are readily obtainable. In a klystron, the bunched electron beam contains signal not only at the frequency of the input signal, but also at harmonics of this signal. This is because the bunching of a sinusoidally velocity modulated beam naturally produces a nonsinusoidal density modulation. The power in these harmonics typically drops in proportion to $1/n^2$, where n is the harmonic number. An alternative to this conventional approach to enhance the harmonic content in terms of power is to utilize the EEHG method. We apply the EEHG method to our device in a uniquely different fashion from how it is used in free-electron lasers. With EEHG, the power in the harmonics scales much more favorably - as $1/n^{1/2}$. In other words, EEHG allows us to obtain significant electromagnetic radiation powers at much higher harmonic numbers than we could ordinarily obtain with a typical klystron which is not incorporated the EEHG beam manipulation. Therefore, we intend to adapt this method into a basic klystron concept to achieve higher power in THz frequency range.

In summary, this dissertation is laid out in the following fashion. In chapter 2, we will present the RF cavity fundamentals and design criteria of an RF cavity. Then, the design steps and results of the fully-integrated high-power SRF gun system that includes a thermionic cathode assembly, 70

K shielding, RF choke and the superconducting main accelerator will be presented in chapter 3. In chapter 4, we will give our initial particle tracking results of the fully-integrated, compact SRF electron gun system. Furthermore, in chapter 5 we will examine the unique concept of a compact THz source. In the last chapter, we will summarize our work and look to the future in terms of next steps to our research in these important areas of electron sources and novel electromagnetic radiation sources. In addition to these chapters, appendices have also been added to the end of this dissertation to give the additional information about the design steps of this work.

2. RADIO FREQUENCY (RF) CAVITY FUNDAMENTALS

As mentioned in the introduction, one goal of this dissertation is to design the electromagnetic properties of a multi-cell, SRF accelerator for several high-average power electron-beam-based applications, including container inspection via the use of high-power X-rays generated from the impact of the high-power electrons on a suitable target. Also mentioned the second goal of this dissertation is to present the design of a novel THz source. Before giving the detailed design steps of a superconducting, multi-cell SRF cavity structure or the design details of the NCRF cavities for the THz source, we will first review, for completeness, the basic details of a single RF cavity and its properties by first using the simple model of the pill-box shaped cavity.

In the second part of this chapter we introduce important quantities that are used for a well-designed accelerating structure such as the accelerating field distribution, the peak electric and magnetic field, the quality factor, and the shunt impedance. These figures of merit are used to design an accelerating structure with the desired properties. In this dissertation we refer to an accelerating structure as one or more accelerating cavities.

2.1. Design Parameters of an RF Cavity

In the field of particle accelerators, RF accelerating structures are used to accelerate the particles to increase or decrease their kinetic energy. Typically we want to increase their kinetic energy, and this will occur if the particles arrive in an RF cavity during the phase of the electromagnetic wave that provides acceleration. However, in the second part of this dissertation, we want to also remind that there are cases when we want to decelerate the particles in an RF cavity. This occurs if the

particles arrive in an RF cavity during the phase of the electromagnetic wave that provides deceleration. The energy lost, properly directed, can then be used for other purposes. For the reasons described in the previous chapter, the use of RF fields to provide acceleration is typically chosen above the other methods such as DC or magnetic induction.

The pillbox cavity is one of the simplest accelerator structures to start with as it can be readily described analytically; nonetheless, it allows us to evaluate the basics before studying more advanced, realistic designs. The pillbox structure is simply an empty cylinder capped at both ends and constructed with a conducting surface as seen in Figure 2.1.

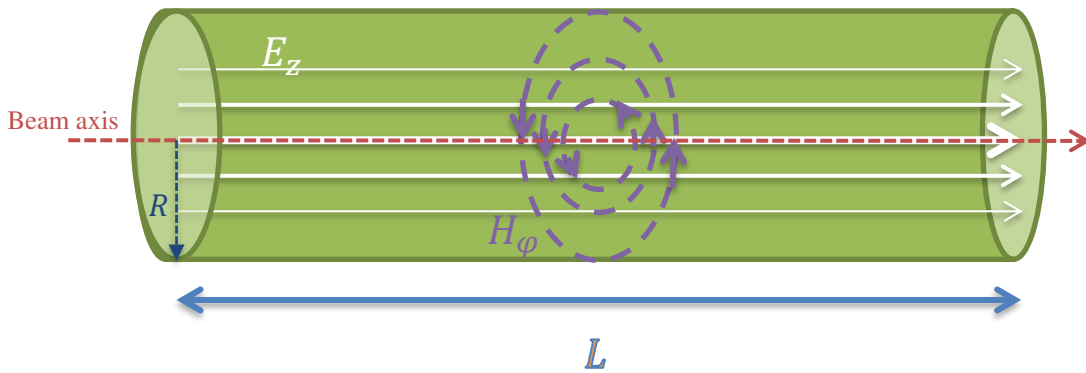


Figure 2: Schematic of a simple pillbox cavity with length L . The cavity has an electric field along the axis, and magnetic field circulates around the axis through the cavity.

To analyze this cylindrical, pillbox cavity structure, we use Maxwell's equations in cylindrical coordinates [25].

$$\nabla \times H = J + \frac{\partial D}{\partial t} \quad (1)$$

$$\nabla \times E = J - \frac{\partial B}{\partial t} \quad (2)$$

$$\nabla \cdot D = q_v \quad (3)$$

$$\nabla \cdot B = 0 \quad (4)$$

Application of the appropriate boundary conditions leads to the characteristic mode solutions. The relevant solution for the particle acceleration is the transverse magnetic (TM) mode where the electric field runs along the axis of the cylinder and the magnetic fields are transverse to the axis. The modes are characterized by three mode numbers, two of them are essential to our discussion, m and n , where m describes how many full-wave patterns exist along the circumference of the waveguide and n tells how many half wave periods there are along the diameter. The third mode number indicates how many zeros exist along the axial direction, however we have used a different method to identify the nature of the mode in this direction and that is by the phase difference between adjacent cells.

2.1.1. Figures of Merit

There are several important parameters we must consider in the design of an RF accelerating structure [26, 27]. These parameters define the design of a cavity and also help to improve the properties of the accelerated beam. The values of these parameters may change depending on the material that is used for design and the fabrication process or the shape of the structure. In the following, we will provide these figures of merit parameters for our SRF compact accelerator.

The mode most commonly used for accelerator structures is TM_{01} mode. Therefore, for concreteness, we focus on the results for the TM_{01} mode of a pillbox cavity in this chapter.

- ***The Frequency of an RF Cavity***

The TM_{01} mode has an azimuthal magnetic field and a longitudinal electric field component given by following equations below.

$$E_r = 0 \quad (5)$$

$$E_z = E_0 J_0(k_r r) \cos(\omega t) \quad (6)$$

$$H_\phi = -\frac{E_0}{Z_0} J_1(k_r r) \sin(\omega t) \quad (7)$$

where E_0 is the peak electric field, J_k is the Bessel function of order k , $k_r = 2.405/r$, $\omega = k_r c$ is the angular frequency, and R is the radius of the cavity.

The first root of the zero order Bessel function is 2.405. Thus when $r = R$ the longitudinal electric field is zero at the walls of the cavity, the TM_{01} accelerating mode. This mode also exhibits the lowest Eigen-frequency for the pillbox cavity [28].

The resonant frequency of this the TM_{01} mode is determined entirely by the radius R and is given by:

$$\omega = 2\pi f = \frac{2.405c}{R} \quad (8)$$

where c is the speed of light. If we would like to build a cavity that works at a frequency 1300 MHz, the radius of the cavity would be 8.83 cm.

- ***Quality Factor of an RF Cavity***

The quality factor of an RF cavity is another important figure of merit, and relates the power dissipation to the stored energy inside the cavity [29]. In short, it demonstrates how effectively a cavity stores and maintains energy. The quality factor Q_0 is simply

$$Q_0 = \omega \frac{U}{P_{diss}} \quad (9)$$

where U is the stored energy and P_{diss} is the dissipation power in the cavity walls.

From the general electromagnetic theory, the stored energy of an electromagnetic field in cavity is

$$U = \frac{1}{2} \mu_0 \oint |H|^2 dV \quad (10)$$

and the dissipation power is

$$P_0 = \frac{1}{2} R_s \oint |H|^2 ds \quad (11)$$

where R_s is the surface resistance of the cavity wall.

The quality factor is related to the number of cycles it would take to dissipate a given amount of stored energy. It is determined by both the cavity geometry and material. Typical unloaded quality factor (Q_0) values are between 10^3 and 10^5 for normal-conducting cavities, and between 10^7 and 10^{11} for superconducting cavities. This major difference is the direct result of the difference in the surface resistance of normal conducting versus superconducting.

The quality factor can also be written as in equation 12.

$$Q_0 = \omega \frac{\mu_0 \oint_V |H|^2 dV}{R_s \oint_S |H|^2 ds} = \frac{G}{R_s} \quad (12)$$

where $G = \frac{\omega \mu_0 \oint_V |H|^2 dV}{R_s \oint_S |H|^2 ds}$ and is called the geometry constant.

As it can be seen in the second part of Equation 12, the ratio of the two integrals is determined by the cavity geometry and the cavity mode. Scaling then allows us to see that the geometry constant is independent of the physical size of the cavity and it is not dependent on the material. In other words, it is frequency and material independent; therefore, this constant is very useful to compare different shapes of cavities.

For a pillbox cavity (both in the normal and superconducting cases), the geometry constant is 257 Ω . For a normal conducting cavity with surface resistance $R_s = 1 \times 10^{-2}$, the quality factor is found to be $Q_0 = 25700$. For the super-conducting case the surface resistance is $R_s = 2 \times 10^{-8}$ using the quality factor $Q_0 = 1.3 \times 10^{10}$.

- ***Shunt Impedance and R_{sh}/Q ratio of an RF Cavity***

Another important quantity used to characterize the losses in a cavity is the shunt impedance (R_{sh}), which is defined as

$$R_{sh} = \frac{V_{acc}^2}{P_{diss}} \quad (13)$$

in units of ohms per cell. This quantity is important as it describes the cavity efficiency, i.e. how well it converts input power into effective net potential.

Ideally we want to maximize the shunt impedance to maximize the accelerating potential for a given dissipated power. This is particularly important for normal-conducting cavities. The power dissipation in the walls is a major issue for copper cavities as they require substantial cooling and high power.

Consider for a moment two identical pillbox cavities, one normal conducting, the other superconducting, and both have identical fields in them. It goes to reason that equal currents are flowing in both in order to generate identical fields. The power losses then are directly proportional to the surface resistance. If, for instance, 100 kW of RF power is supplied to the normal conducting cavity to maintain the desired potential, then the power required for the SC case is roughly 0.1 W.

The shunt impedance of the SC cavity is typically about 10^6 times that of a normal conducting cavity, and this is one of the primary reasons to gravitate toward the SC RF system.

We can also define another ratio, R_{sh}/Q that is independent of the surface resistance (due to the P_{diss} term cancelling out). Using equation 9, equation 13 can be rewritten as in equation 14.

$$\frac{R_{sh}}{Q} = \frac{V_{acc}^2}{\omega_0 U} \quad (14)$$

This quantity allows us to compare different RF geometries. In a normal-conducting cavity, where power dissipation is a major concern, the R_{sh}/Q is maximized by using a smaller beam pipe. In addition to this, this ratio can be increased by choosing a re-entrant cell shape (otherwise called nose cones). In contrast, as surface resistance is low in superconducting cavities, the dissipated power is much smaller; therefore, superconducting cavities can have larger a beam pipe and not suffer significantly on achievable field gradients.

- ***Transit Time Factor and Accelerating Voltage of an RF Cavity***

For an RF cavity design the most commonly quoted figure of merit is the accelerating voltage. The field seen by the particle changes with time when a particle passes through the RF field in the cavity. This effect will impact the overall gain in particle energy. In other words, the field strength seen by the particle can be written in equation 15.

$$E = E_0(z)e^{i(\omega z/c + \phi_0)} \quad (15)$$

where $E_0(z)$ is the amplitude of electric field, ω is the frequency of the RF field and ϕ_0 is the initial phase of the field.

The energy gain of the particle through the cavity can then be written in equation 16.

$$W = q \left| \int_0^L E_0 e^{-i(\omega z/c + \phi_0)} dz \right| = L \frac{qE_0 \sin\left(\frac{\omega L}{2c}\right)}{\frac{\omega L}{2c}} \quad (16)$$

where q is the charge of the particle and L is the acceleration gap of the RF cavity.

Equation 16 can also be used to define the transit time factor for a pillbox cavity in TM_{01} mode.

$$T = \frac{W}{qE_0L} = \frac{\sin\left(\frac{\omega L}{2c}\right)}{\frac{\omega L}{2c}} \quad (17)$$

The transit time factor takes into account the time variation of the field during particle transit through the gap.

Here we assume that the electron passes through the cavity on-axis, the electron is relativistic with a velocity nearly equal to c , and that the electron passes through the center of the cavity when the field has reached its maximum. We then obtain

$$V_{acc} = E_0LT \quad (18)$$

where T is the transit time factor and is the term that accounts for the fact that the field is constantly changing as a function of time, and in the case of a non pillbox cavity also the longitudinal position within the cavity.

Similarly the average accelerating gradient is

$$E_{acc} = \frac{V_{acc}}{L} = E_0T \quad (19)$$

The accelerating gradient or voltage can be limited by the operation modes most notably whether one is operating in continuous wave (CW) or pulsed conditions. The limitations of the gradient in the CW mode for the normal-conducting case using copper is driven by the ohmic heating. As a rule of thumb this limits the gradients to around 2 MV/m. In the superconducting case, however, the critical magnetic field of the superconductor limits the accelerating gradient. In the case of using Niobium, this gradient is around 55 MV/m. However, in practice, thermal instabilities and field emission decrease the limits to about 40 MV/m in a single cell and 23 MV/m in multi-cell SRF structures.

On the other hand, the limits change in the pulsed mode, particularly for the NCRF case. In this mode, the average ohmic losses in the room temperature case are reduced by the duty cycle (the ratio of the pulse width to the RF period). If the duty cycle is small enough in the normal conducting cavities, the cooling does not limit the accelerating gradient and gradients above 100 MV/m are readily achieved with the ultimate limitation coming from field emission resulting in electrical breakdown in the cavity (a spark).

- ***Peak Surface Fields***

A primary limitation to superconductors is surface magnetic fields. If the surface magnetic fields exceed a critical level H_{peak} then the superconductor quenches. Similarly we also have to worry about the peak electric field on the surface E_{peak} . Above a certain level surface imperfections lead to field emission and this can create tremendous problems for the superconductor; however, at the same time it is our goal to achieve high electric fields. Therefore, as a measure of the effectiveness of a superconducting cavity design we strive to reduce the ratio of the peak fields $\frac{H_{peak}}{E_{peak}}$.

To maximize the accelerating gradient, it is also important to minimize the ratio of peak fields to the accelerating field. For a π -mode 1.3 GHz SRF pillbox cavity operating at 1 MV, using the half wavelength 11.5 cm and cavity radius is 8.83 cm from Equation 8 the peak fields ratios can be calculated as:

$$E_{acc} = \frac{V_{acc}}{d} = \frac{1 \text{ MV}}{0.115 \text{ m}} \cong 8.7 \text{ MV/m} \quad (20)$$

$$E_{peak} = E_0 = \frac{\pi}{2} E_{acc} = 13.7 \text{ MV/m} \quad (21)$$

From Equation (7) the magnetic peak field can be written as:

$$H_{peak} = \frac{E_0}{Z_0} J_1(1.84) = \frac{E_0}{647\Omega} \quad (22)$$

where Z_0 is the free-space vacuum impedance. We, therefore, can obtain the ratios of surface fields

$$\frac{E_{peak}}{E_{acc}} = \frac{\pi}{2} \cong 1.6 \text{ and } \frac{H_{peak}}{E_{acc}} \cong 2430 \frac{\text{A/m}}{\text{MV/m}}.$$

Before the optimization of more realistic SRF cavities we compare the analytical calculations and SUPERFISH [30] simulation results for the pillbox cavity dimension given above. The important cavity parameters and field map of the pillbox cavity are presented in Table 1 and Figure 3.

As expected both results agree well with each other. Even though the pillbox cavity structure helps us to analyze the equations, in order to propagate a beam through a cylindrical structure, a beam pipe at the beginning and at the end of the cavity needs to be added. In this configuration, analytical solutions of the fields are not readily solved. However, since these represent perturbations, the primary results from the pillbox cavity are not changed in any major way. In this case, with deviations from an ideal pillbox, we look to well-known simulation codes such as SUPERFISH,

Comsol Multiphysics [31] and CST Microwave Studio [32] to solve the fields and provide us with the detailed properties of the cavity design. In the next chapters of this dissertation, we will present our electromagnetic field design results using SUPERFISH for our SRF and NCRF cavities. (In Appendix 1 and 2, you can also find the electromagnetic results which are obtained using Comsol Multiphysics and CST Microwave Studio.)

Table 1: Analytical and SUPERFISH cavity parameter results for SRF pillbox cavity

Parameters	Units	Analytical Results	SUPERFISH Results
Resonance Frequency, f	[MHz]	1300	1300
Cavity Material	Niobium (Ni)		
Operating Temperature, T	[K]	2	2
Surface Resistance, R_s	[Ω]	2.68×10^{-8}	
Shunt Impedance, R_{sh}	[Ω]	4×10^{13}	4×10^{13}
Quality Factor, Q		9.57×10^9	9.56×10^9
Stored Energy, U	[μJ]	3.3	3.3
Dissipated Power, P_{diss}	[mW]	2.88	2.86
Peak Electric Field to Accelerating Field Ratio, E_{peak}/E_{acc}		13.67	13.77
Peak Magnetic Field to Accelerating Field, H_{peak}/E_{acc} Ratio	$\left[\frac{A/m}{MV/m} \right]$	2527.8	2543.67

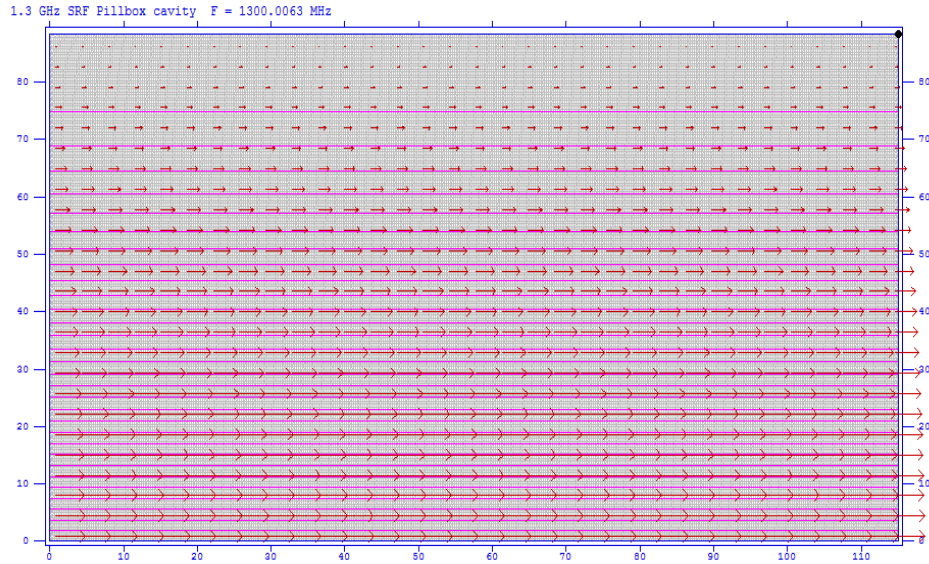


Figure 3: 1.3 GHz SRF (Niobium) pillbox cavity electric field distribution

2.2. Optimization Parameters for Designing an RF Cavity

As we discussed in the previous section, the main method of insuring efficient acceleration is to maximize the shunt impedance. This is true for both the normal-conducting and the superconducting case.

In the normal-conducting case that is operated in a CW manner, most of the cavities have so-called “nose-cone” designs in order to obtain higher shunt impedance and therefore higher net potentials for a given input power. This is because the limitation is really the average power going into ohmic losses and the need to cool the cavity. The nose cone design style allows us to increase the transit time factor (reminder – this is related to the time variation of the field as the particle crosses the accelerating gap of the cavity) and enhancing the peak field strength around the beam’s axis [33].

In the super-conducting CW case, the limitation is not due to ohmic heating. The maximum performance is dominated by the surface fields; therefore, instead of optimizing the shunt impedance, we optimize the surface field ratios. Elliptical cavity profiles have been chosen as they minimize the peak surface field to accelerating field, E_{peak}/E_{acc} , while allow for the necessary control of the resonant frequency (the cell diameter) and the operating mode (the cell length).

There are also several more design parameters that we define for an elliptical cavity as shown in Figure 4, and there are clear reasons for these choices [34, 35].

- The iris ellipse ratio (b/a) uniquely affects the peak surface fields, and these should be kept small in order to achieve maximum gradient.
- The equator ellipse ratio (B/A) has no effect on the electromagnetic performance but affects the mechanical strength of the cavity and is used to adjust the overall effective length.
- The cell iris radius (r) is managed by the beam dynamics considerations as well as by the requirement of the cell-to-cell coupling. Even though a larger iris radius reduces the effect of wake fields (beam-cavity interactions) and High Order Modes (HOMs), it reduces the shunt impedance of the fundamental accelerating mode, and also reduces the maximum achievable accelerating gradient.

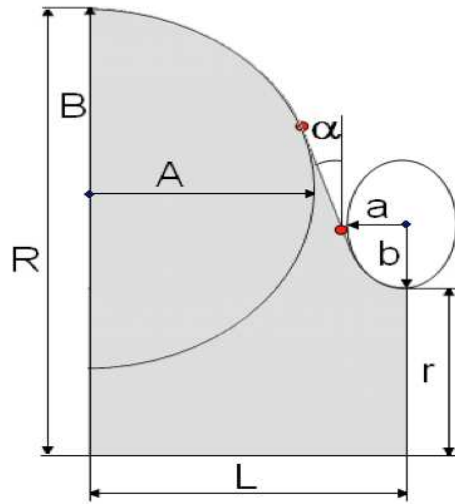


Figure 4: An elliptical cavity geometry design parameters.

- The slope of the side wall (α) determines the electric and magnetic peak fields on the cavity wall and needs to be optimized to maximize the peak surface field ratio.
- The cell length (L) determines the geometrical beta value of the cavity and for a $TM_{01} \pi$ -mode it should be equal to $L = \lambda / 2$.
- The cell radius (R) is used for frequency tuning with almost no effect to any electromagnetic or mechanical cavity parameters.

In this chapter, we discussed the design parameters of an RF cavity. We listed and derived several important figures of merit in cavity design such as resonant frequency, the quality factor, the geometry factor, the R/Q ratio, transit time factor, accelerating voltage and the maximum field ratios. In addition to these parameters, we also discussed the parameter optimization and geometry options specific to the technology of an RF cavity, normal or super conducting. The designed parameters will be presented in detail in the following chapters for both the superconducting RF electron source and normal conducting THz klystron cavities.

3. DESIGN OF A COMPACT INTEGRATED HIGH-POWER SUPERCONDUCTING RADIO FREQUENCY (SRF) ELECTRON BEAM SOURCE

Even though there is significant interest in achieving higher-average power and compact electron sources, there has been limited progress in the field, particularly in the area of electron sources integrated with superconducting, radio-frequency (SRF) systems. By integrated we mean a single device – gun and rest of accelerator - not separate- function, modular components. As we previously discussed in chapter 1, many challenges must be overcome for such integration. However, the combination of a new SRF surface treatment technique, a novel thermionic cathode/electron-gun source integrated with the accelerator, the use of cryo-cooling technology, conduction cooling and a simple but well-controlled, phase-stabilized magnetron RF source may lead to a novel, high-average power SRF electron source that would be cheaper, more compact, and require less infrastructure than other devices.

There are number of challenges to obtain many of the desired beam and system properties in such a fully-integrated, compact SRF-driven electron source. Incorporating the advancements mentioned above, we have designed a compact, integrated SRF electron source that has high beam power and operates up to 10 MeV. Careful consideration of the gating of the thermionic cathode and direct integration of the cathode into the SRF accelerator in a manner that effectively virtually eliminates all beam loss within the accelerator has guided the design results given herein.

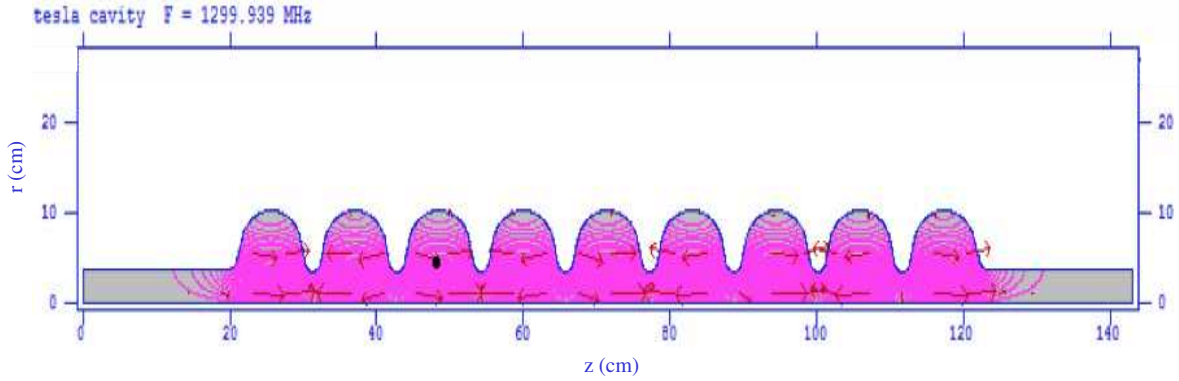
3.1. Electromagnetic Design of the Integrated System

In an electron source, the cathode system is critical for achieving stable intensity and high-average power. The envisioned gun will provide short bunches injected into a specified phase range of the RF cycle. Doing this process correctly limits the current intercepted by the superconducting walls and prevents an unwanted load on the cryo-cooler system. In our design, we re-designed the first cell of the standard, 9-cell, 1.3-GHz ILC/XFEL to form an 8.4-cell electron source. The length of the first cell is primarily chosen to account for the difference between the average velocity of the electron in the cell compared to the phase velocity, c . The gun (first) cell –with a length ratio of 0.4 of a full cell– contains the cathode system and provides the initial acceleration. The latter eight cells are in standard size and for acceleration. This design feature is key to the overall compact fully integrated design. We have used several simulation codes to design and validate this unique system.

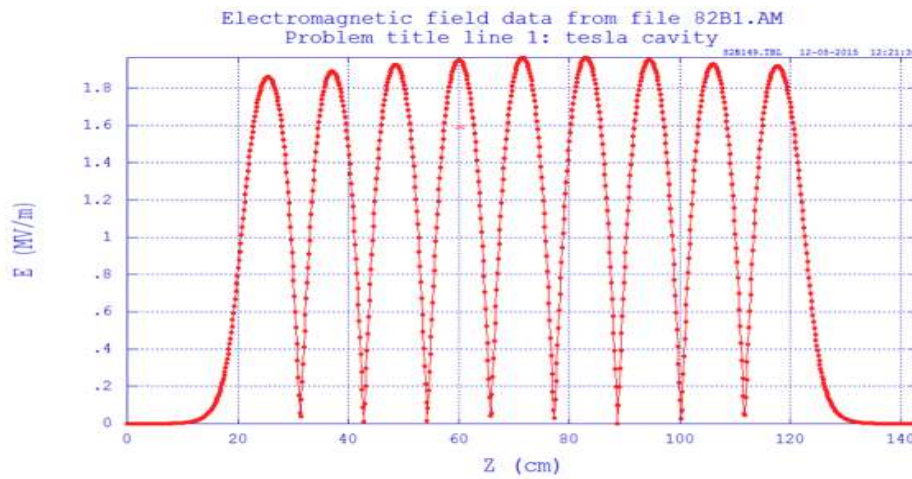
3.1.1. Design of the Gun and Overall Accelerating Structure

In our accelerator design, the 8 cells of the standard ILC/XFEL cavity parameters are used and the first cell of this structure is redesigned to match the desired parameters of an integrated electron gun [36].

To begin, a 9-cell ILC/XFEL superconducting elliptical cavity geometry file was created as a SUPERFISH geometry file using an internal code [37] and transferred to SUPERFISH to ensure SUPERFISH would work correctly for future optimization and design studies. The output of this simulation is given in Figure 5.



(a)



(b)

Figure 5: a) Detailed geometry and field mapping of the 9-cell ILC – TESLA cavity b) Electromagnetic field distribution for the given geometry

Our next step was to modify the first cell of the 9-cell, ILC/XFEL accelerating structure so that it would be suitable for the initial cell containing the cathode region.

Using these results as a reference, the design of the gun cell for the desired configuration was started with the goal of obtaining the desired field distribution in the π -mode (adjacent cells operating 180 degrees out of phase with one another) and at the chosen 1.3-GHz frequency. To meet these requirements, we have optimized the design parameters that are presented in detail in

chapter 2 and the results of which are given in Table 2. The initial design parameters were calculated for the geometry of an elliptical cavity as shown in Figure 6. Tolerances are assumed to be $\pm 100 \mu\text{m}$ during this RF design optimization based on the fabrication process. These values will be recalculated for the fabrication process, taking into account the dimensions of a cooled cavity and the chemical treatment of cavity surfaces.

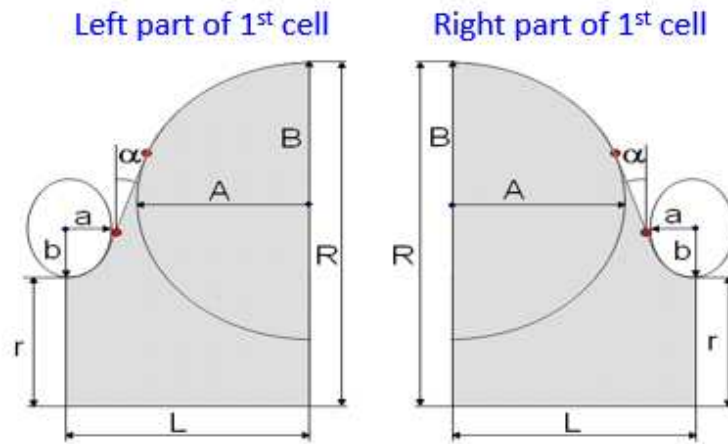


Figure 6: The parameters of an elliptical cavity's design geometry. The parameter values of the modified (gun) cell are given in Table 1.

Table 2. The design parameters of the modified (gun) cell

Design Parameters	Left part [mm]	Right part [mm]
Iris Radius, r	3.5	35
Cavity Radius, R	99.05	99.05
Length, L	12.93	34.59
External Radius, A	11.53	24
External Radius B	11.53	24
Horizontal Half Axis, a	1.4	9.2
Vertical Half Axis, b	1.4	12
Wall Slope, α	0°	2.6°

Figure 7 shows a frequency scan of the 8.4-cell structure performed with the code SUPERFISH. As seen, there are two frequencies near the desired 1.3-GHz operating point; however, only one frequency, that of 1300.92 MHz, gives the desired TM_{01} mode. This is the pi-mode frequency of the standard ILC/XFEL geometry design.

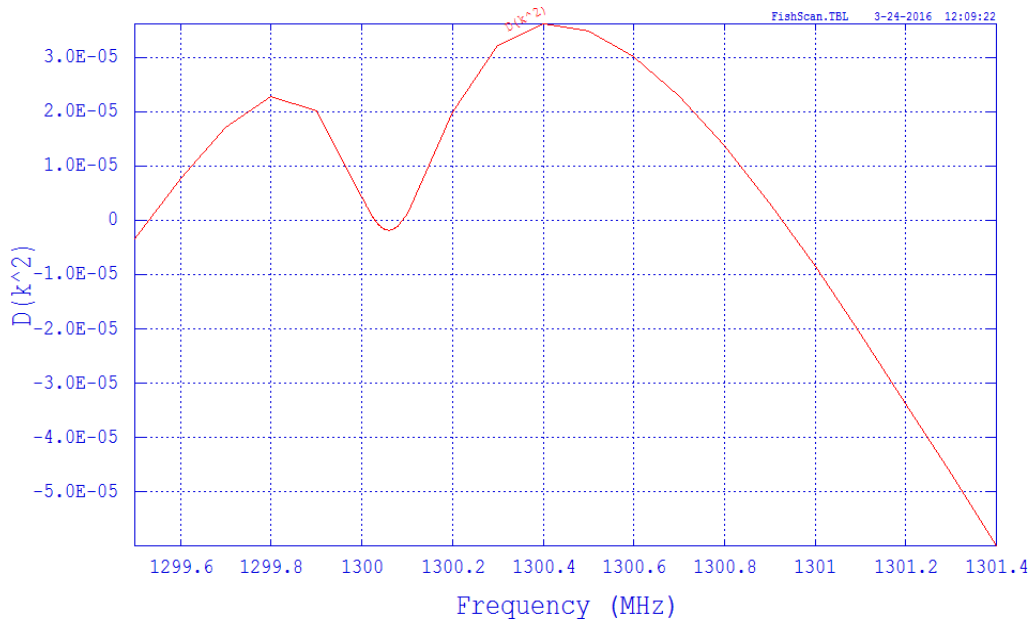
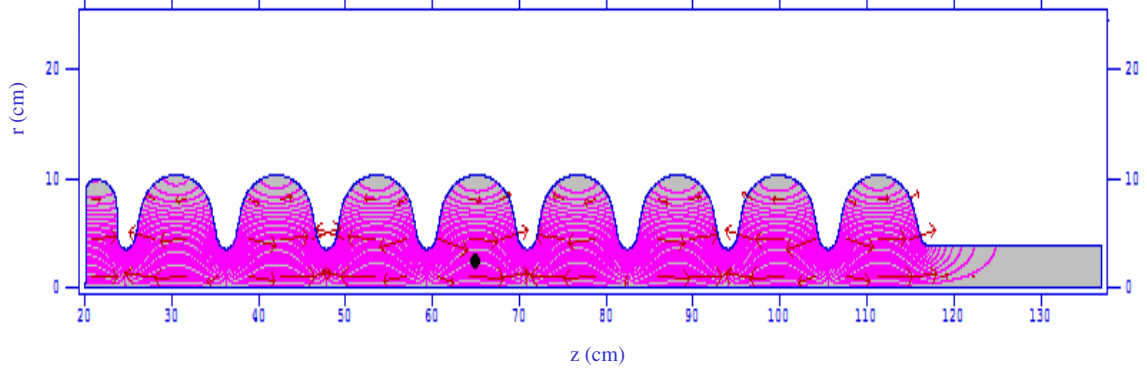


Figure 7: Frequency scan results of our 8.4-cell structure’s design with the embedded gun.

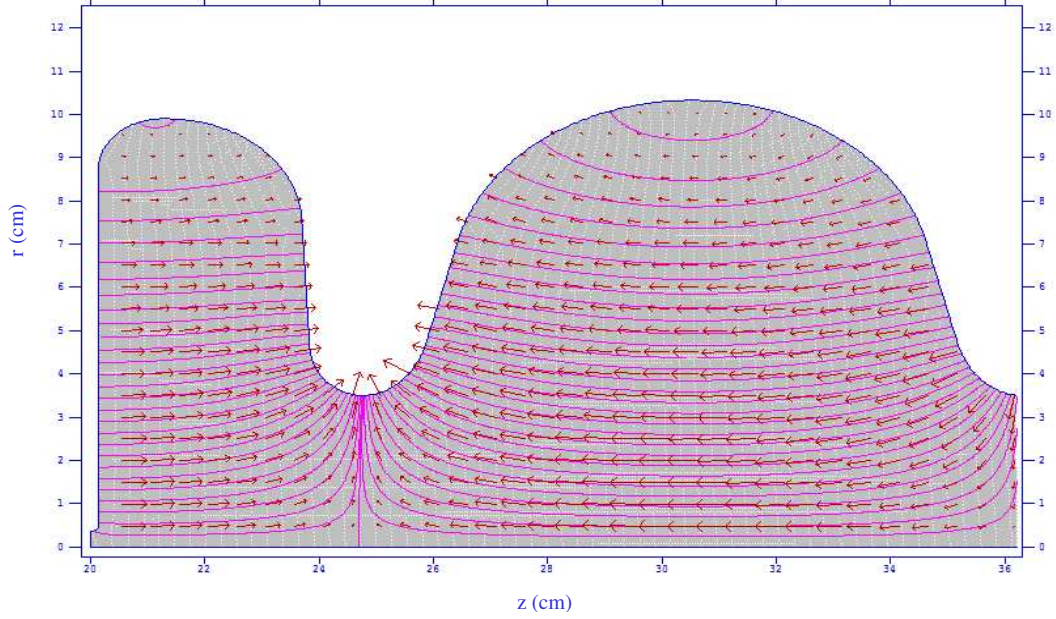
Figure 8 (a) shows the 8.4-cell structure and field map with arrows and contours. Figure 8 (b) is the magnified view of (a) for the first 2 cells to illustrate the field map of the 8.4-cell cavity’s geometry. Figure 8 (c) shows the on-axis field distribution of the 8.4-cell accelerating cavity. The field in the gun cell has been optimized based on the design conditions to achieve maximum gradient.

1.3 GHz SRF-gun Modified 9 cells geometry-N.Sipahi CSU/FNAL F = 1300.9256 MHz

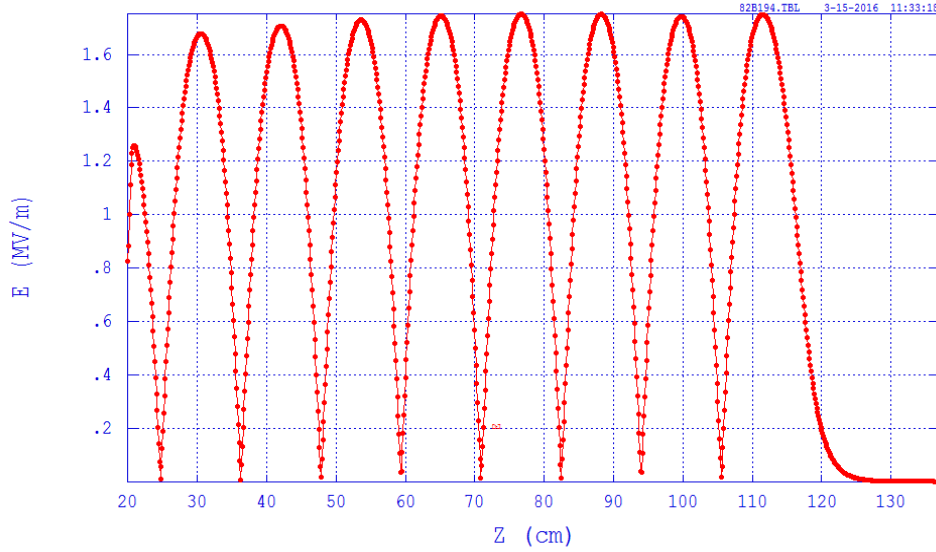


(a)

1.3 GHz SRF-gun Modified 9 cells geometry-N.Sipahi CSU/FNAL F = 1300.9256 MHz



(b)



(c)

Figure 8: a) The 8.4-cell structure’s design geometry matched to the 1.3-GHz frequency and its field map in SUPERFISH b) The magnified view of the first 2 cells c) The electromagnetic field distribution of our 8.4-cell structure’s design geometry as computed by SUPERFISH.

Two additional simulations tools were used as a check on the results: the 2-D code COMSOL Multiphysics and the full 3-D code CST MWS and the results are given in Appendix A. Strong agreement was found in all three cases. As such, the essential results of the additional simulations are contained in the appendix. For consistency we will present in the primary text only the SUPERFISH results since these results have been used as the input for the beam dynamics simulation part.

The design steps were then repeated for the case of a shorter first cell – a length of 0.3 of a full cell. This allowed us to perform some design optimization of the gun cell length based on the metrics of the beam’s performance will be mentioned later. As it can be seen in Table 3, the output parameters are quite similar to those found with a first cell length of 0.4 of a full cell.

Table 3: The results of SUPERFISH for two different lengths of the first cell (0.3 and 0.4 of a full-cell length)

Parameters	SUPERFISH Results	
Gun Cell Ratio	0.4	0.3
Frequency [MHz]	1300.9	1300.9
E_{peak} , [MV/m]	21.7	22.6
B_{peak} , [mT]	45.1	45.4
$\frac{B_{\text{peak}}}{E_{\text{peak}}}$ [mT/(MV/m)]	2.07	2.0
R/Q [Ω]	931	908
Quality Factor, Q	9.8×10^9	9.9×10^9

3.1.2. Design of the Cathode Region

We have chosen a thermionic cathode for our design. Since a thermionic cathode is by its very nature operated at high temperature, this could present an issue within a superconducting environment; however, it is not as problematical as it might be imagined when a proper design is used for cathode assembly.

The cathode will be operated in vacuum and we will assume that a very low thermal conductivity holder holds it in place. Power (heat) radiated from the cathode into the RF cavity structure region is then dominated by black-body radiation. The Stefan-Boltzmann equation (Equation 23) can then be used to calculate the black-body heat emitted from the cathode.

$$P = A \epsilon T^4 \quad (23)$$

where A is the surface area of the cathode, ϵ is the emissivity, σ is the Stefan – Boltzmann constant, and T is the temperature in Kelvin.

Assuming a cathode with a 3 mm radius, a cathode temperature of 1200 K, and a worse case emissivity as 1, the power (heat) emitted is roughly 3.3 W. Operation at even slightly lower temperatures will drop this number dramatically and increase the cathode lifetime, but at the expense of a lower current density.

The cathode region is designed with a 70 K shield just downstream of the cathode. The aperture of this shield is such that it intercepts any heat that would otherwise directly impact the superconducting surfaces. Since the RF cavity apertures are very large, they are effectively in the shadow of this shield plate and so they do not directly see the cathode. Therefore, the impact of the heat from the cathode on the superconducting surfaces is limited. Moreover, we also add an RF choke into this cathode region. This help us to prevent the main accelerator region from influencing the gating process [38]. The schematic of the cathode region is shown in Figure 9.

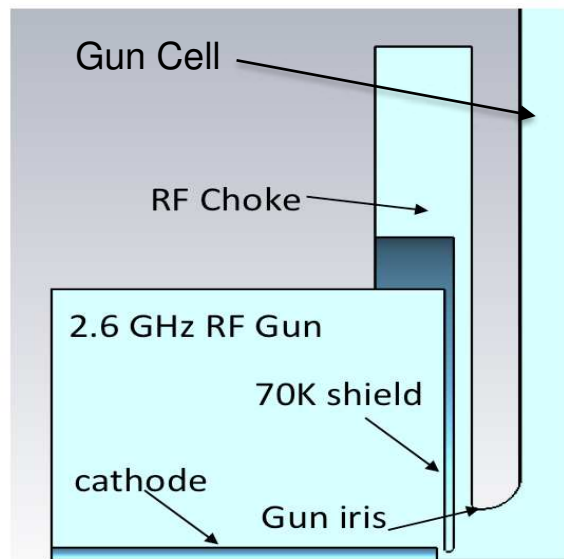


Figure 9: Schematic view of the cathode assembly indicating 70K shielding and RF choke

We also make the tacit assumption that a suitable thermionic cathode material can be found that does, in itself, not contaminate the superconducting environment. Our first choice is the M-type dispenser cathode as these have proven quite robust and have sufficient emission at relatively low temperature. We are also considering other cathodes for future design steps, including field emitters, should the thermionic cathode design prove intractable.

One significant issue with a thermionic cathode system is that it emits electrons if the RF field at the cathode is the correct sign. If the cathode is subjected to only the fundamental 1.3-GHz field then it emits electrons over a full 180 degrees. Unfortunately, not all these electrons will make it out of the accelerator. Many will either strike the superconducting surfaces and present a significant heat source or back bombard the cathode. Therefore, we must gate the electron emission to limit phase range of emission that will ensure acceleration of the electrons without them striking the superconducting surfaces or back bombarding the cathode. The gating process is illustrated in Figure 10.

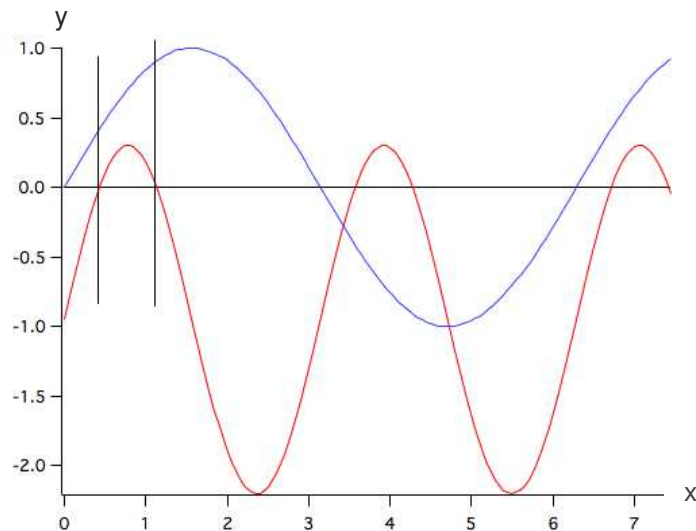


Figure 10: The gating process using fundamental frequency (1.3 GHz) and second harmonic of the fundamental frequency (2.6 GHz). The blue line indicates the fundamental frequency and red line indicates the second harmonic. (x-axis indicates the time and y-axis indicates the field amplitude)

To implement the gating of charge from the cathode surface, we have incorporated an additional resonant cavity behind the cathode plane of the half-cell that is designed to be resonant at the second harmonic of the main frequency, i.e. at 2.6 GHz; this region will also be held at a DC bias as can be seen in Figure 10. We present the detailed design results of this region both separately and coupled to the 8.4-cell accelerating structure in between Figure 11 and Figure 13. By judicious choice of the fundamental and second harmonic field amplitudes, the relative phases between the two RF fields, the DC bias field and the carefully chosen longitudinal location of the cathode, we are able to effectively and simply gate the electrons over the desired range of RF phases.

The detailed design of this region has been done in several steps [39]. First, the cathode region which resonates at 2.6 GHz was separately designed. We again used SUPERFISH to examine the geometry and the fields. The results from COMSOL and CST MWS are also presented in Appendix B. During the design process, the two important parameters are the length of the 70K shielding and the location of the RF choke in order to resonate the cathode assembly at 2.6 GHz. Figures 11 and 12 show the design steps while optimizing the cathode assembly geometry.

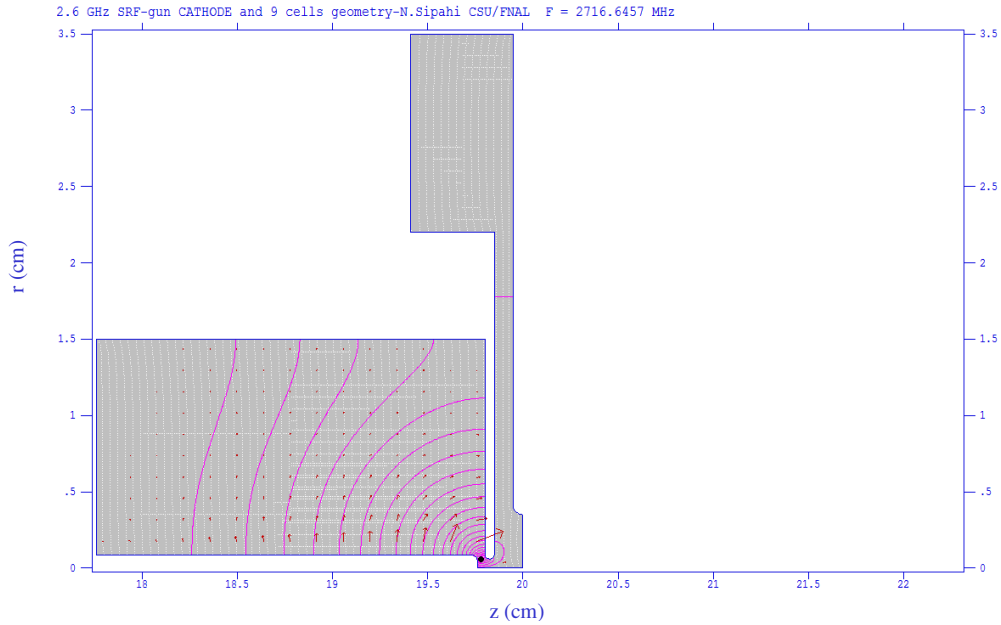


Figure 11: Cathode assembly design using 1.5 cm-length 70K shield wall

In Figure 11, 70 K shielding is 1.5 cm length. Even though there is not any field propagation through the main accelerating structure, the cathode assembly resonates around 2.71 GHz. Therefore, further optimizations have been done to optimize the frequency and this result is shown in Figure 12.

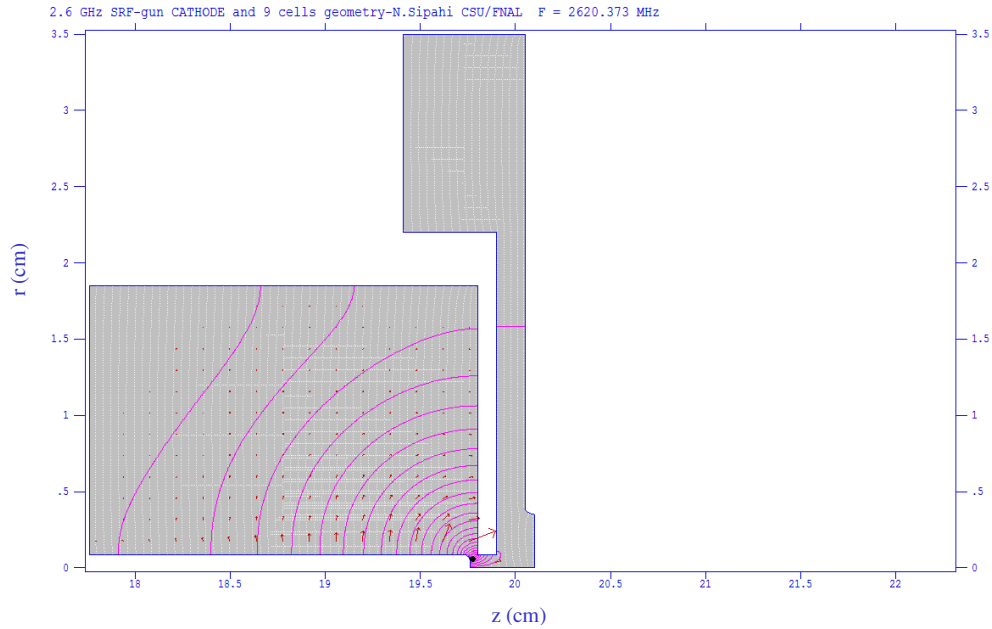
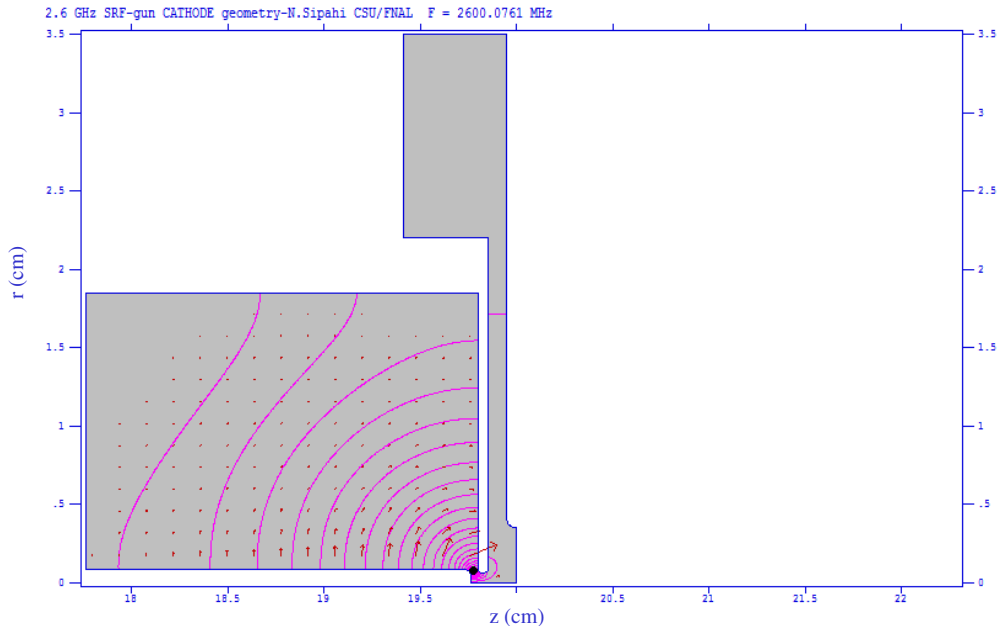
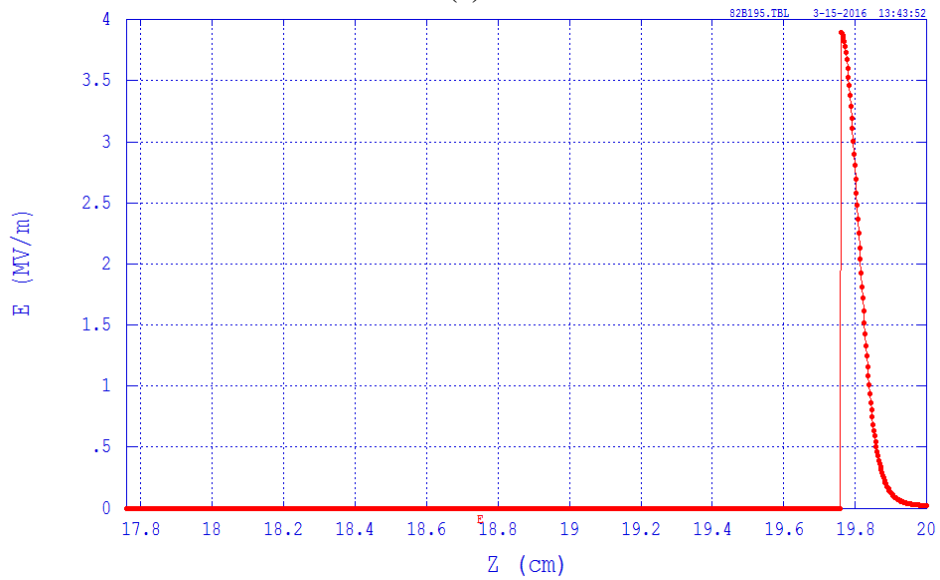


Figure 12: Cathode assembly design locating the RF choke 1 mm further than the cathode place

In this step, the RF choke is located 1 mm further from the cathode place. This optimization allows us to get closer to the second harmonic frequency. However, the structure still operates at 20 MHz higher frequency than the second harmonic of the fundamental frequency. Therefore, further iterations have been performed to optimize the resonant frequency of the cathode assembly at 2.6 GHz, and the optimized cathode geometry which is operating at 2.6 GHz frequency and includes optimized RF choke and 70 K shielding wall is given in Figure 13.



(a)



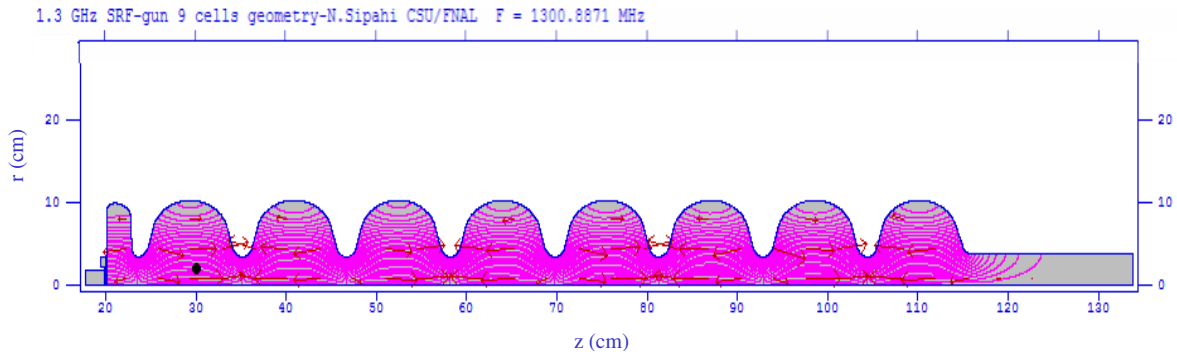
(b)

Figure 13: a) The cathode region's design geometry at 2.6 GHz with the field generated using SUPERFISH. b) The on-axis electromagnetic field distribution of the cathode region's design geometry used in Figure 5 as calculated by SUPERFISH.

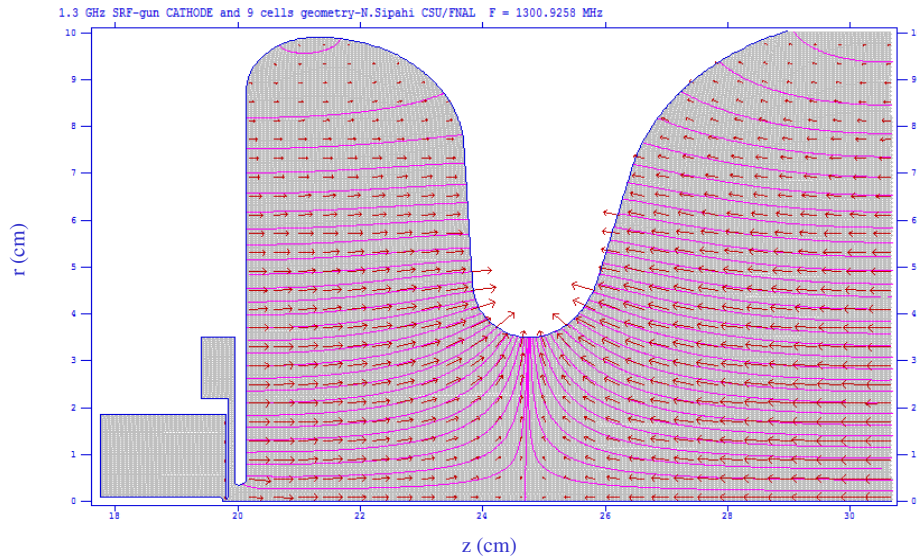
3.1.3. Design Combination of the Cathode and the Gun into a Single Structure

Until here, we described how we separately designed the cathode and accelerator regions of the entire structure. We now will show the results of the combined system.

Using SUPERFISH, we first checked the impact on the resonant conditions when we combined the two structures into one. As can be seen in Figure 14, the field from the 8.4-cell structure when excited solely at the fundamental frequency of 1.3 GHz does not propagate through the iris to the cathode region.



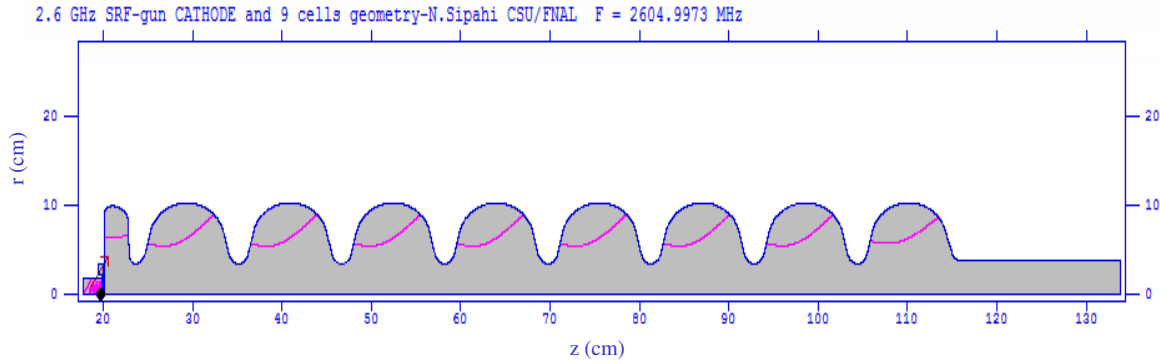
(a)



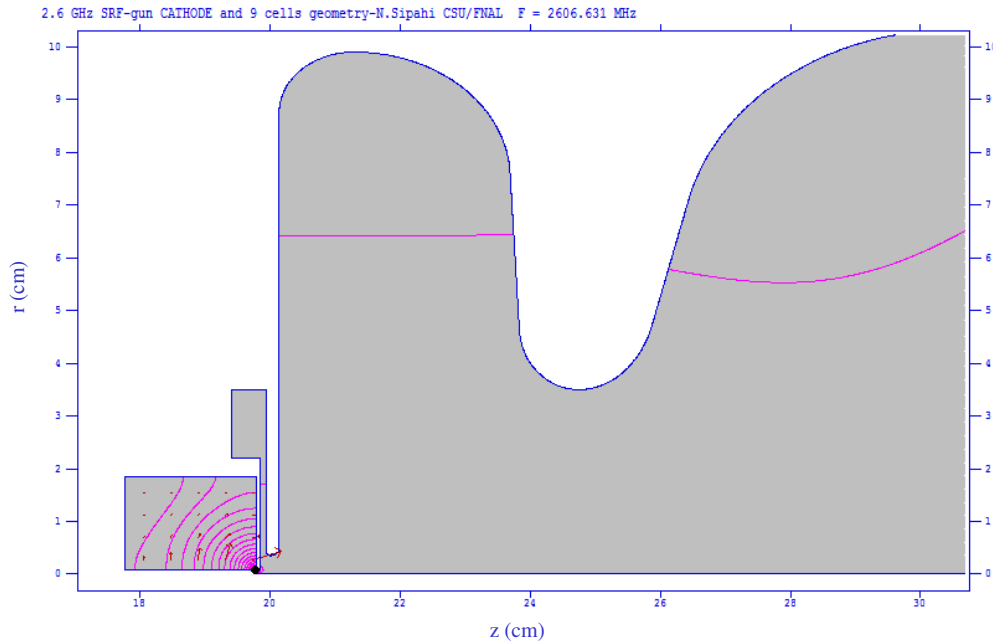
(b)

Figure 14: a) The design geometry of the combined cathode and gun regions at 1.3 GHz as calculated using SUPERFISH. b) The magnified view of the cathode and the first cell regions

Similarly, if we excite only the cathode region at 2.6 GHz, then we can see that there is very little coupling of field into the main accelerating region (Fig. 15) and will be completely inconsequential compared to the dominant 1.3-GHz frequency component. These show us that the two regions are independent.



(a)



(b)

Figure 15: a) The design geometry of the cathode and gun structures together and the results at 2.6 GHz b) The magnified view of the cathode and first cell regions when integrated as shown in Figure 18 as calculated using SUPERFISH.

As a summary of this chapter, we have performed detailed electromagnetic simulations to design an accelerating structure with an integrated cathode part based on a 9-cell ILC/TESLA SCRF structure. We designed the cathode region for the integrated gun concept where the accelerating region resonates at 1.3 GHz and the cathode region is resonant at 2.6 GHz. This design, together with a DC bias field will allow us to gate the electrons into the main structure over a range of RF phases favorable to acceleration without loss of beam on the SC surfaces or through back-bombardment. During these simulation steps, we have used the 2D SUPERFISH electromagnetic design code (also COMSOL Multiphysics codes and the 3D CST MWS). In next chapter, we will give the detailed beam dynamics studies of this integrated system.

4. BEAM DYNAMICS SIMULATIONS FOR THE INTEGRATED SRF ELECTRON SOURCE

In the previous sections, we examined if a plausible RF electromagnetic design of the gun and cathode region could be achieved. Further, we examined if this gun region could be integrated fully, in terms of the electromagnetic RF design, with the rest of the accelerator, keeping in mind the overall goal of compactness and reduction of duplicative infrastructure commonly associated with separated function electron guns and structures. Since we convinced ourselves thus far that the RF electromagnetic design of our concept is feasible, we now can begin to examine the cathode region and analyze the gating process of the thermionic cathode as losses would most likely be attributed to releasing electrons into the accelerating structure during an unfavorable phase window [40].

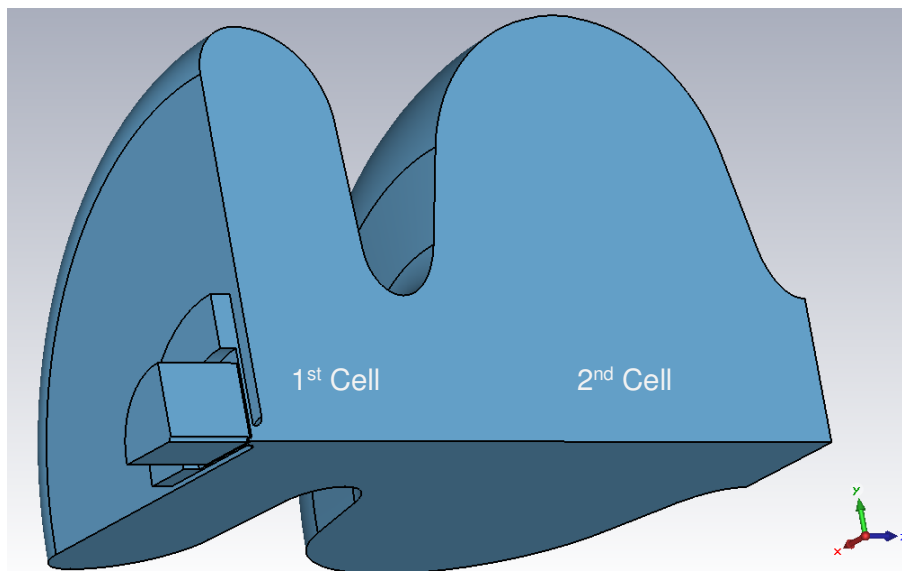


Figure 16: The solid model of the RF Gun and the cathode region as modeled in CST MWS.

The solid model of the cathode region which resonates at 2.6 GHz and the first two cells which resonate at 1.3-GHz is shown in Figure 16. Also shown is a cutaway of the cathode region to illustrate the detail. The RF choke blocks RF leakage of the 1.3 GHz into the adjacent region cathode region and the 70 K shield prevents thermal leakage into the 4K area.

For the particle tracking, as in case of the RF electromagnetic design, we used several particle tracking codes which are SMASON [41] and SPIFFE [42] (also ASTRA [43] results are given in appendix D) to examine the integrated design in detail.

4.1. Simulation Results using SMASON

SMASON is capable of simultaneously simulating multiple RF frequencies and their nearly arbitrary field distributions as well as DC fields. In addition, it is capable of tracking particles through these fields. It includes space charge effects making it ideal for simulating the complexity near the cathode of our design. It uses the Finite Element Method for the field calculation in the electron guns and the Particle-in-Cell Method for the numerical simulation of the electron emission and space charge within the applied RF and DC voltages. It is a spatially 2D program with the macro-particles described by the infinitely thin rings with uniform charge distribution [ibid, 41].

We used SMASON for more realistic initial particle tracking simulations of the combined (cathode assembly and gun) structure. We transferred the cathode and gun cell geometry into SMASON as can be seen in Figure 17.

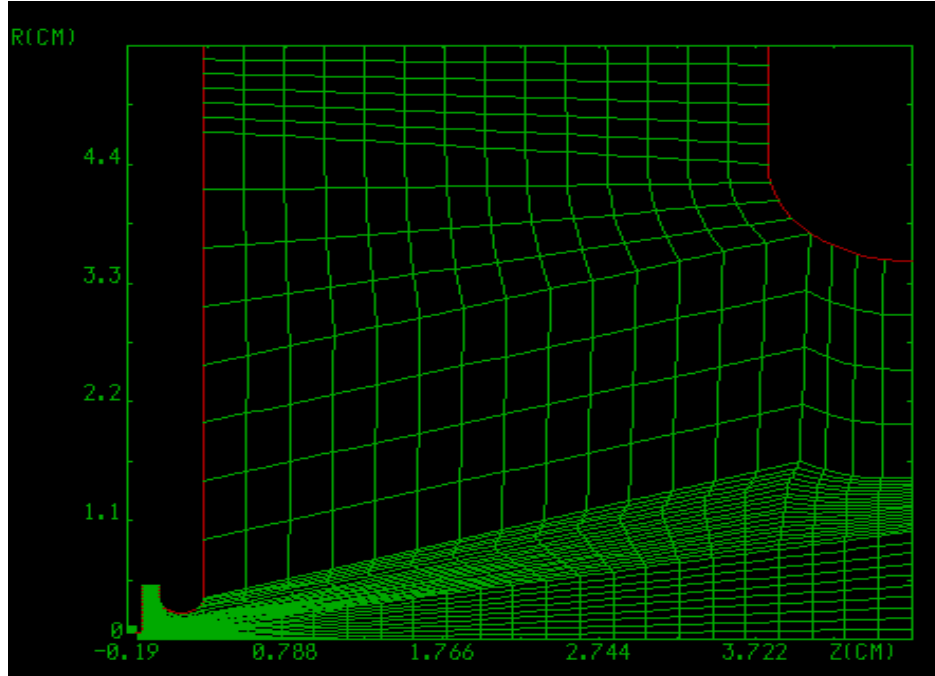


Figure 17: The mesh view of the combined geometry of the cathode assembly and the gun cell in SMASON.

SMASON is used to track the electrons from the cathode up to the plane of the iris between the first and second cells. The voltage from the cathode into the first cell has time and spatial dependence as shown in Equation 24 and 25.

$$U_1(s, t) = U_{a_1}(s)\cos(\omega t + \varphi) \quad (24)$$

$$U_2(s, t) = U_d(s) + U_{a_2}(s)\cos(2\omega t) \quad (25)$$

where $U_d(s)$ is the constant bias voltage, $U_{a_1}(s)$ is the amplitude of the RF voltage operating at the fundamental, $U_{a_2}(s)$ is the amplitude of the RF voltage operating on the second harmonic, and φ is the phase difference between the fundamental and the second harmonic RF fields.

Our optimization goal was to limit the beam losses to the cavity walls to less than ~ 0.5 W (of a total of 5 W, so therefore 10%) while delivering a 10-MeV, 2-mA beam of electrons. A cathode area of 0.78 mm^2 was assumed. The longitudinal profiles of the DC, the fundamental RF, and the second harmonic RF (phase differences included) were summed together linearly with their amplitudes set by the optimization routine. The optimization process also varied the relative phase between the fundamental and second harmonic.

SMASON simulations were performed to find the conditions of optimal performance, as defined by minimizing the beam loss through the system. These parameters are presented in Table 4.

Table 4: The optimized beam parameters at the end of first cell as simulated by SMASON.

Beam Parameters	Values
Bias Voltage	2 kV
RF Voltage	2.72 kV
Average Gradient of Fundamental Frequency (1.3 GHz)	~ 8 MV/m
Average Gradient of Second Harmonic Frequency (2.6 GHz)	~ 5.4 MV/m
Phase	-15°
Energy (end of the 1 st cell)	0.335 MeV
Energy Spread	5.9 %
Average Current	2 mA
rms Phase Size (rms Bunch Length)	$\sim 7.3^\circ$ (15.6 ps at 1.3 GHz)

In Figures 18, the outputs of SMASON are shown for the bunch length and energy spread at the end of the gun cell as a function of the relative phase between the fundamental and second harmonic. According to these results to achieve the smallest bunch length and energy spread at the same it needs to be operated at a phase difference of -15 degrees.

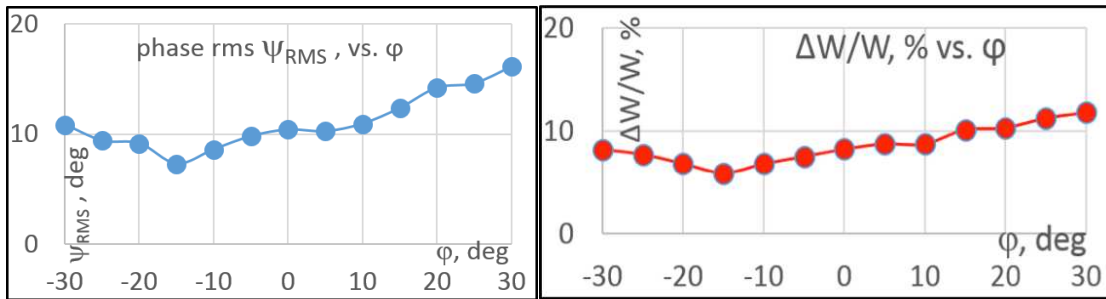


Figure 18: The bunch length vs. relative phase (left) and the bunch rms energy spread vs. phase for the SMASON simulations.

The results from SMASON represent a start; however, more sophisticated, capable codes are required to explore some of the fine details.

4.2. Beam Dynamics Simulations using SPIFFE

In addition to the initial SMASON results, we continue to study more detailed beam dynamics simulations of the fully integrated (cathode assembly and the 9-cell structure) system with another particle in cell code called SPIFFE [ibid, 42]. SPIFFE is short for **S**Pace Charge and **I**ntegration of **F**orces **F**or **E**lectrons. It is also a well-known simulation code especially for analyzing the space charge effects and the beam behaviors close to the electron gun area and it has been previously bench-marked in several studies [44, 45, 46].

In order to perform particle tracking with SPIFFE, we must define the simulation region and the cavity geometry. The grid sizes and the boundary conditions must also be defined before running the input file. There are two ways to track the particles through the defined structure. One is to define antennas according to the geometry in order to excite the cavities to obtain the field distribution. The other way is to import the external field distribution from another electromagnetic field design codes. This way is also much faster way computationally than the first way. Therefore, we chose the second way and imported the field map of the full design from SUPERFISH as we presented in the previous chapter. After importing the field distributions, we were able to generate Figure 19 that shows the boundaries of the geometry and the field distribution.

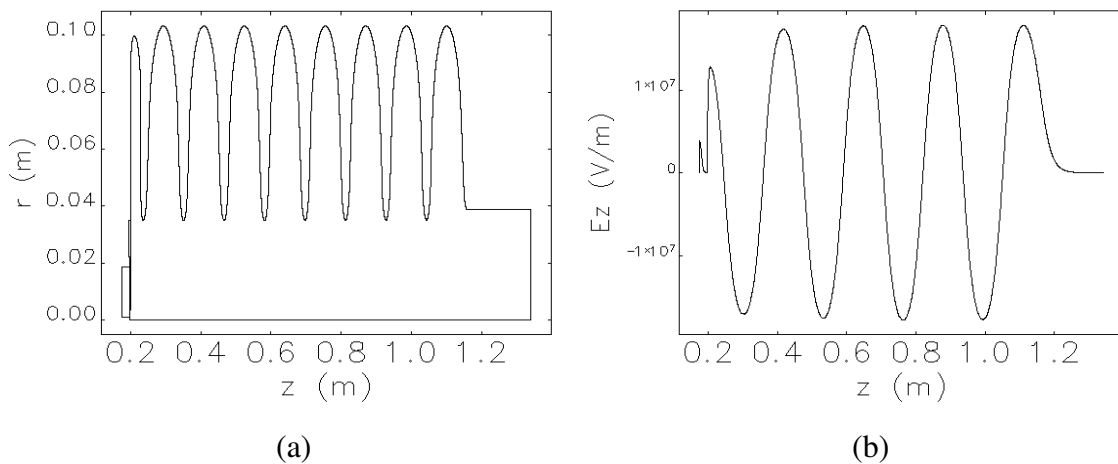


Figure 19: a) The boundary of the combined structure b) The field distribution of the combined structure in SPIFFE

After transferring the field map into SPIFFE, the next step was loading particles. There are two different ways to generate particles for tracking. One is to directly load a particle distribution and the other is to define a cathode for particle generation. Since we have the design of the cathode system and would like to analyze the results of a realistic cathode geometry coupled to the rest of the accelerating structure, we defined a thermionic cathode with the current density, 100 kA/m²

with a cathode area of 0.78 mm^2 . We then looked at two cases: one with no gating and one when the gating is functional.

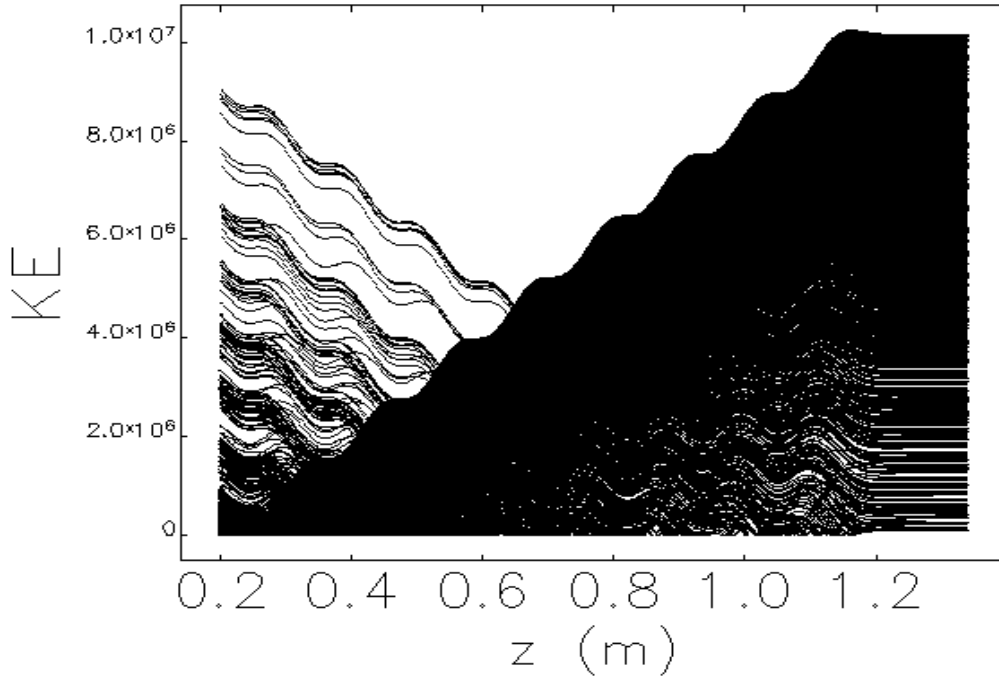


Figure 20: Kinetic energy of all particles in one bunch through the combined structure (cathode and 8.3-cell geometry)

Figure 20 shows the kinetic energy plot of all particles in a bunch that are emitted from the cathode without gating. Even though some proportion of the particles in the bunch travel through the end of the cavity, their final energies are different and most of them have less than 10 MeV. Moreover, there are also many undesired particles some of which oscillate in the fields and eventually propagate backward and are lost. Here, we have intentionally not gated the electrons that entered the structure to illustrate this undesirable effect. This is highly undesirable since the particles can strike the surfaces of the SRF cavities and cause detrimental issues such as quenching as well as back bombardment and thermal runaway of the cathode [ibid, 43].

Figure 21 shows the time evolution of the number of sequential particles in one bunch emitted off the cathode. The odd behavior is due to many particles emitted from the cathode at too late a phase to get fully accelerated. Even though some particles are not at the optimum phase, they can be accelerated through the structure but then they get lost into the cavity. The others are trapped in subsequent RF cycles leading to the peculiar and unwanted phase space distribution.

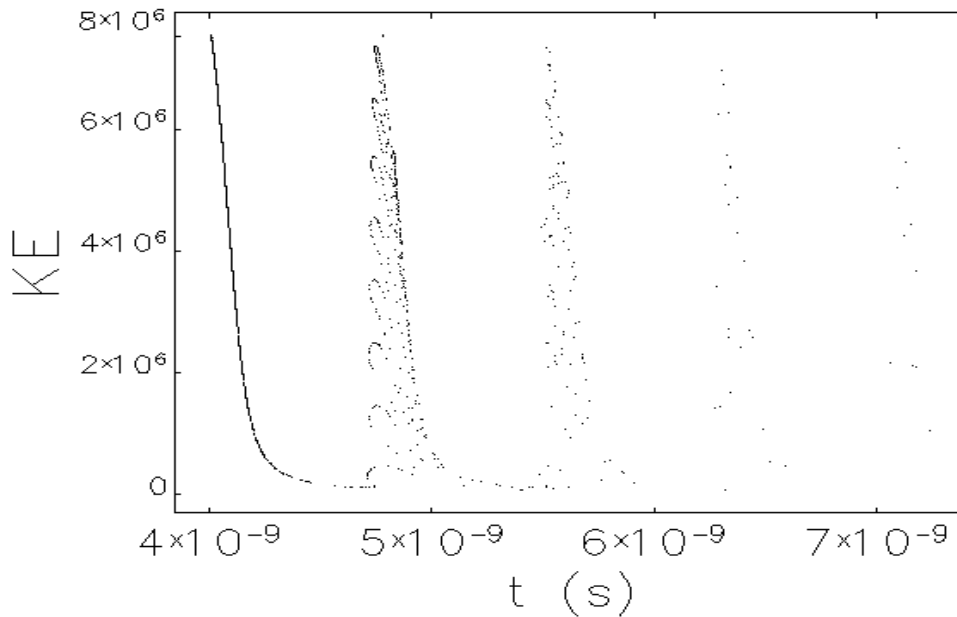


Figure 21: Longitudinal phase space in time for the particles in one bunch without gating process

In Figure 22, it can be seen that while the bunch travels through the integrated structure, many particles strike the SC surface and many others travel backward through the cathode. As a result of this behavior, the beam emittance increases. The final transverse phase space is given in Figure 23.

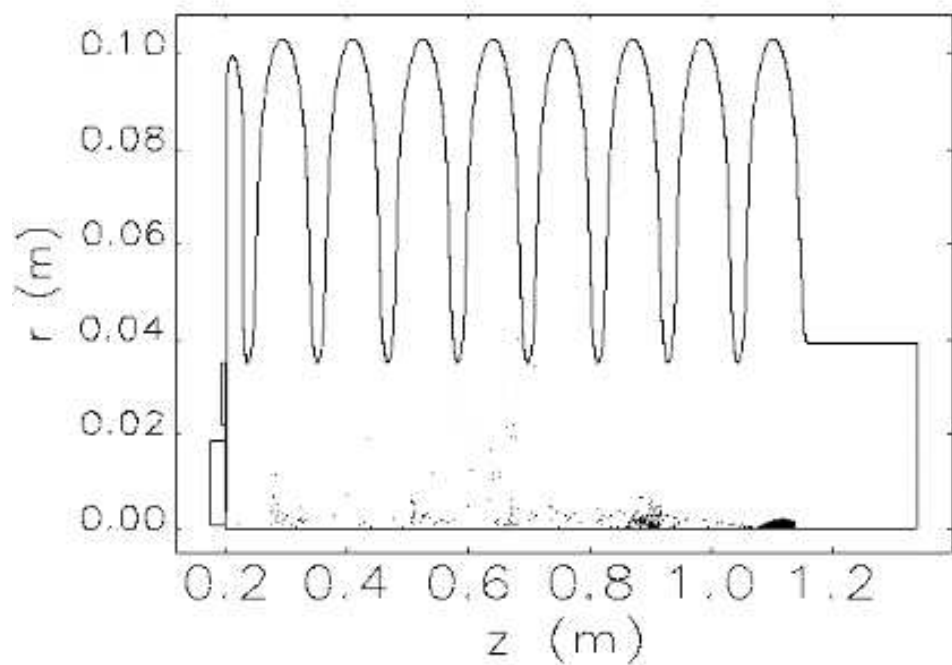


Figure 22 : The snapshots of the bunch travels through the integrated structure without gating process

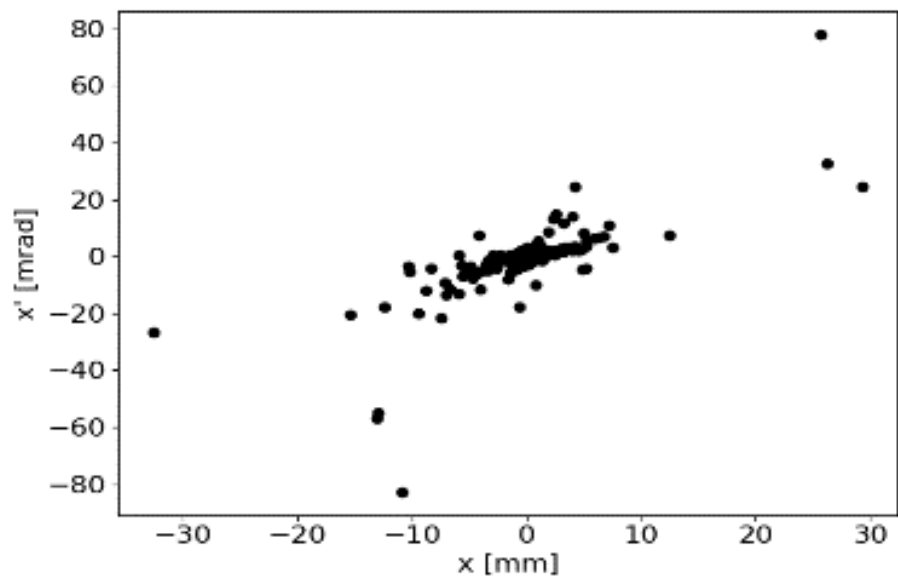


Figure 23: Transverse phase space at the end of the integrated structure without gating process

Next, we simulated the gating that we intend to implement in our system. In this step, we simulate the gating by emitting the particles from the cathode by assuming that the emission will occur. Figures 24 and 25 show the kinetic energy through the full structure and longitudinal phase space in time with gating, respectively. In Figure 24, snap shots of the bunch are spaced by 50 ps. This time, the average kinetic energy of the particles is 9.4 MeV at the end of structure. This means that by gating we avoid the large energy spread and capture all particles without loss.

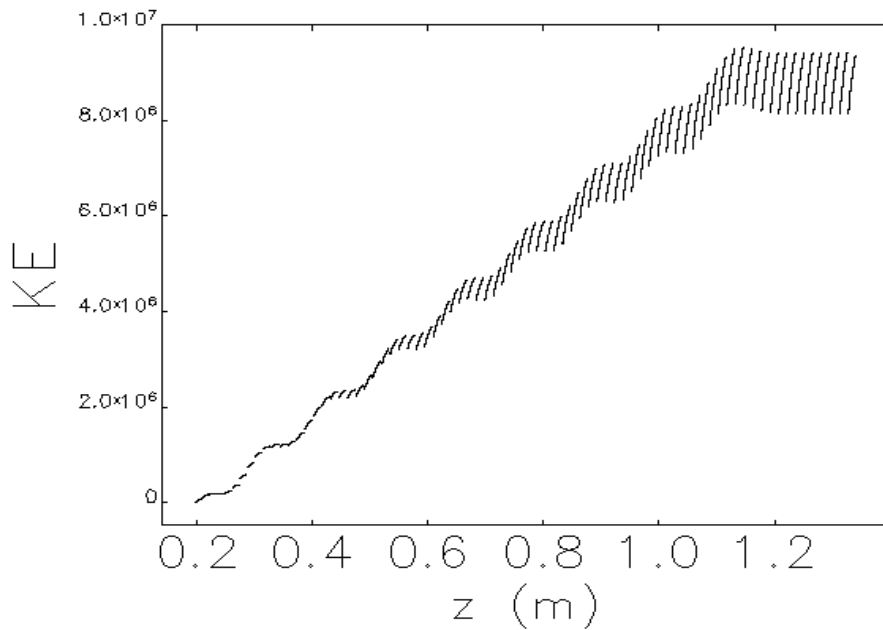


Figure 24: The kinetic energy of a bunch through the combined structure

In Figure 26, it can be seen that the bunch travels through the integrated structure without any losses in the SC surface. This allows an emission that will ensure acceleration of the electrons without them striking the superconducting surfaces. This process allows us to get much smaller emittance values. The transverse phase space at the end of the structure is given in Figure 27.

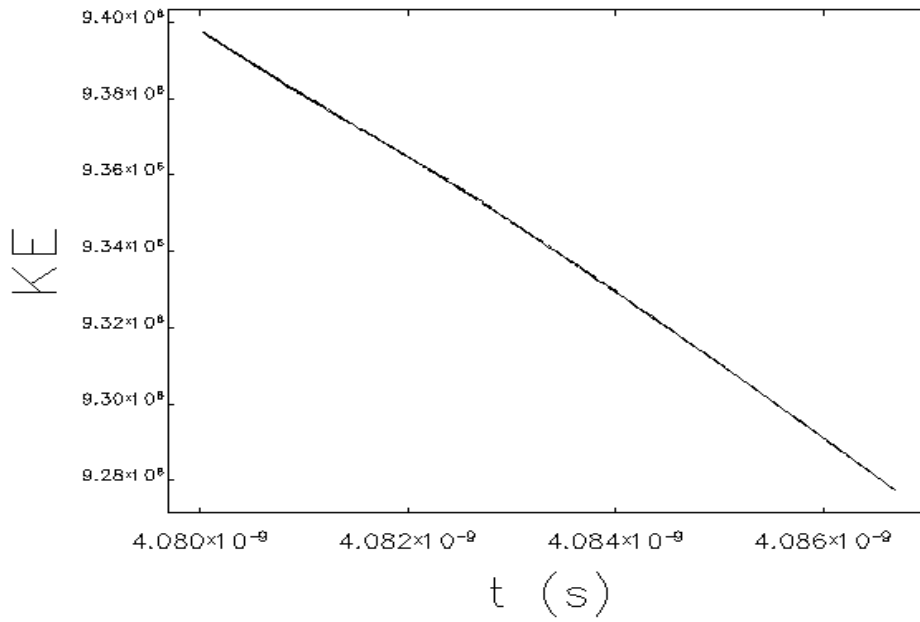


Figure 25: The longitudinal phase space in time for the particles in one bunch with gating process

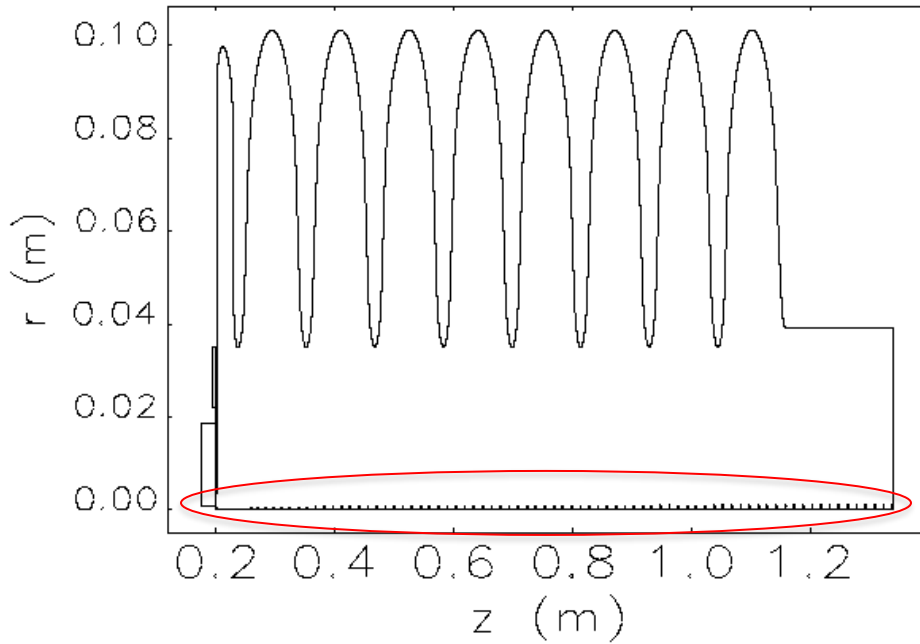


Figure 26: The snapshots of the bunch travels through the integrated structure (Red ellipse is added to this figure to indicate the traveling bunches.)

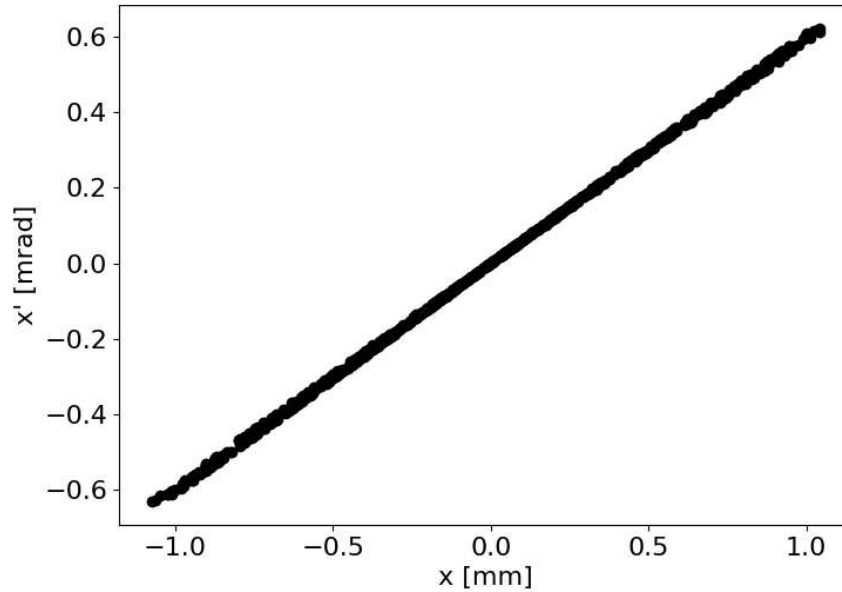


Figure 27: Transverse phase space ellipse at the end of the integrated structure with gating process

As a summary, we performed the charged-particle tracking simulations using SMASON and SPIFFE codes (and ASTRA results are given in appendix) to analyze the beam behaviors through the full structure. We are confident from the results that our design has merit and shows potential for operation. The initial gating method shows promise and space charge effects appear to be minor and controllable.

Now, we will move to the second topic of this dissertation – the generation of a unique source of long-wavelength radiation. As it can be seen, many of the same considerations of cavities tuned to a specific electromagnetic frequency, harmonics of electromagnetic radiation, power in electron beams (that can be increased by increasing the beam energy or beam current), etc. are also used in the second part of the dissertation.

5. DESIGN OF A COMPACT, CW KLYSTRON-INSPIRED TERAHERTZ (THZ) ELECTROMAGNETIC RADIATION SOURCE

In this second part of the dissertation, we are exploring if a unique, klystron-inspired configuration could be designed and realized to generate a high power source in THz frequency range. Our initial design of this klystron-inspired source, radiating at 0.2 THz, shows great promise of achieving these and other higher sub-THz and a pathway to THz frequencies in a compact system. This system was conceptualized by mapping our knowledge of higher harmonic generation in free-electron lasers into this new source.

5.1. The Principles of a Klystron

In an effort to generate electromagnetic radiation for applications such as communications and radar, Russell and Segurd Varian (Varian brothers) developed and patented the klystron idea in 1935 and first tested it in 1937. Its concept is simple – it is an amplifier of electromagnetic radiation extracting additional power from a powerful electron beam at the same frequency as an input signal [47].

Addition to the description of the klystron in Chapter 1, we will discuss it in detail now. A klystron is an electron tube used to amplify electromagnetic radiation in the microwave frequency regime. It uses two major principles – that of electron beam bunching and that of extracting electromagnetic radiation power at a specific frequency from this bunched electron beam. In the klystron concept, there are two cavities, each, in the case of today's klystrons, are resonate at one

single microwave RF frequency. One is called the “buncher” and the other the “catcher.” A buncher cavity, via an input RF signal, implements a velocity modulation on the incoming electron beam. This velocity modulation develops into a density modulation (current modulation) in the drift between the buncher and catcher cavities. The catcher cavity then turns the power in the current modulated beam into electromagnetic energy that can be subsequently used for other purposes.

So we asked ourselves that if there is a way to use the principle of the klystron to achieve THz frequencies and to produce more powerful harmonic wavelengths – those whose power does not drop significantly. Based on concepts used in the short wavelength electromagnetic radiation production regime, we can find an answer to this question.

5.2. The Principle of the Echo-Enabled Harmonic Generation (EEHG) Method

In the 1950s, a self-excited, drift-tube klystron frequency multiplier was investigated [48]. There are a few research efforts that use the same method in order to multiply the frequency from X-band (8 – 12 GHz) to the Ka-band (26.5 – 40 GHz) range [49]. Despite these related studies, there are no existing operational, or even designs of, klystrons that employ the frequency multiplier method to achieve THz frequencies. Because of this, we set out to explore how one can achieve THz wavelengths with a klystron-inspired idea.

Our original concept is to increase the output frequency of the klystron into the Terahertz regime by adapting the principles of beam manipulation methods used in the electron-beam-based, short-wavelength, and free-electron laser (FEL) light source community[50]. One of these advanced

methods is called Echo-Enabled Harmonic Generation (EEHG) and this is what we will explore. In the meantime recall that all genres of FEL electron beams are in the relativistic regime, i.e. all electrons are travelling near the speed of light; however, the electron beam velocities in klystrons are in the nonrelativistic regime.

As a prelude, we examine the basic operation of a free-electron laser (FEL) [51, 52] to show the piece wise steps of operation as well as the relation to the fundamental principles of klystrons. Figure 28 shows the comparison between an oscillator FEL, a Self-Amplified Spontaneous Emission FEL (SASE FEL), the High-Gain, Harmonic-Generation (HG) Method, and the Echo-Enabled, Harmonic-Generation Method (EEHG).

In an oscillator FEL (Fig. 28 (a)), EM radiation is produced when the electrons travel through the field of the undulator. Significant radiation is produced at wavelengths

$$\lambda_n = \frac{\lambda_{und}}{2n^2} \left(1 + \frac{K^2}{2} \right) \quad (26)$$

where λ_n is the output wavelength of the n^{th} harmonic, λ_{und} is the period of the undulator field, γ is the normalized beam energy, and K is the normalized magnetic field strength of the undulator. Some of this light is trapped between the mirrors of the oscillator. If the spacing between the mirrors is set correctly then the trapped pulse of light overlaps the next bunch passing through the undulator field. If the light is sufficiently intense then there can be an interaction between the electrons and the electromagnetic field. Specifically the electron's transverse motion can couple to the electric field of the EM pulse and gain or lose energy depending on the phase relationship

between the EM field and the electron's motion. This periodic energy variation eventually turns into a density modulation of the electron bunch at the resonant wavelength given by the above equation. As such, these electrons will begin to emit coherently. The result is a favorable instability to exponentially drive further bunching of following electron bunches. This process continues until saturation is reached. The resultant light is then considerably brighter than what would occur in the incoherent emission. It is also fully coherent both transversely and longitudinally.

A Self-Amplified Spontaneous Emission FEL (Fig 28 (b)) works in a similar manner to the oscillator described above; however, there are no mirrors and the process occurs in a single pass. For this to work we need a very long undulator for the process to reach saturation. In addition only obtains partial longitudinal coherence, as there is no potential for feedback across the entire length of the bunch. To improve the longitudinal coherence we could conceivably propagate an external EM seed pulse tuned to the resonant wavelength; however, this is not possible at very short wavelengths, and other methods need to be used.

A high-gain harmonic-generation FEL (Fig. 28 (c)) works in a similar way to a SASE FEL; however, this time an external seed pulse (e.g. from a laser) is co-propagated with an electron bunch in an undulator. The interaction creates a periodic energy modulation along the length of the bunch. The bunch is then passed through a dispersive region where the energy modulation is converted into a density modulation that contains signal at the fundamental and higher harmonics. This micro-bunched beam is then passed through a subsequent undulator tuned to a chosen harmonic where it radiates coherently at the wavelength of the harmonic. This allows us to get past the limitation of finding a sufficiently powerful seed source at the desired wavelength; however,

we are still limited by an achievable high harmonic, and this limitation is driven primarily by the energy spread in the electron beam.

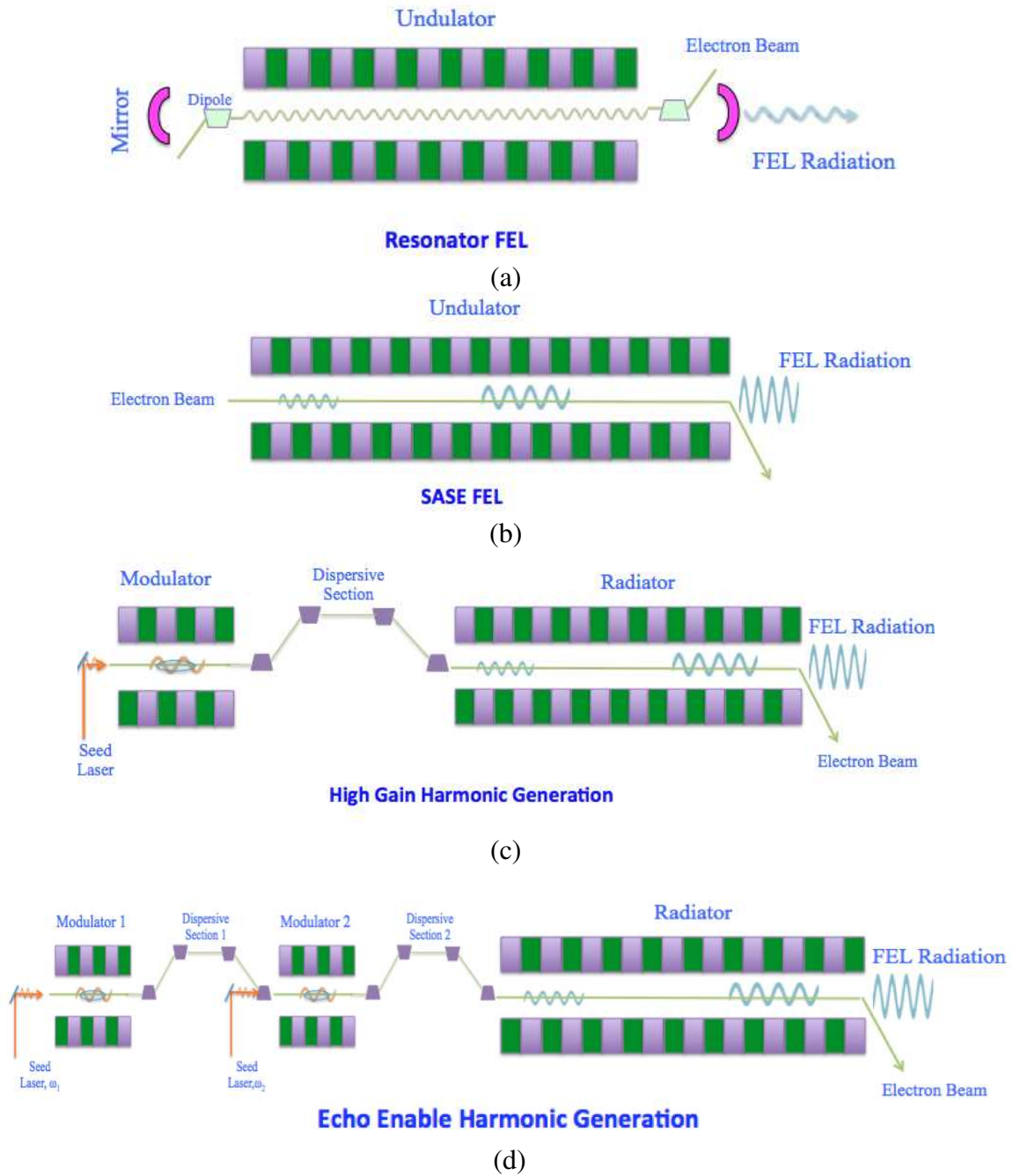


Figure 28: Schematic of a) resonator FEL b) Self Amplified Spontaneous Emission FEL (SASE FEL) c) High Gain Harmonic Generation (HGHG) Method d) Echo Enable Harmonic Generation Method (EEHG)

The echo-enabled harmonic-generation (EEHG) process (Fig. 28 (d)) is similar to the HGHG method which constructs the basis of our new proposed concept. Here we use a series of modulation and dispersion sections to induce on the beam a density modulation at very high harmonics of the input signals. This micro-bunched beam is then forced to radiate significant power at the chosen higher harmonic.

In a slightly more detailed description of the EEHG process a laser pulse is used to modulate the beam energy in the first undulator. This energy-modulated beam then passes through a dispersive region where the energy modulation shears the bunch into many narrow energy bands. A second laser pulse and undulator system then modulates the energy of this sheared beam. The beam is then passed through a second, dispersive region where this energy modulation is also converted into a density modulation at a chosen wavelength dependent on the frequencies of the lasers and effects of the dispersive regions. Then final undulator, much like in the HGHG case, is tuned to the desired harmonic.

The major difference is that in the EEHG FEL, is that it can successfully generate much higher harmonic than with the other processes. This can be attributed to the initial shearing of the bunch into many narrow energy bands. The energy spread in the beam is what limits the harmonic number, but the shearing process used in EEHG effectively narrows the effective energy spread in the beam and allows us to achieve much higher harmonics.

We recall however that FELs, whether oscillators, SASE, HGHG or EEHG all utilize relativistic electrons. Now we adapt EEHG to the nonrelativistic regime of klystrons.

5.3. Design of a Klystron-inspired THz Source

The theory of EEHG was conceived with the assumption that highly relativistic electron beams were being used. In fact, for all practical purposes the electrons used in a typical EEHG system, for generating short-wavelength, X-ray radiation, can be assumed to be moving at near the speed of light. For these electrons, energy modulations do not translate into any significant velocity modulation and so dispersion in a strong magnetic chicane system is used to shift their relative positions as a function of their modulated energy. Klystrons literally operate at the other end of the spectrum. The electrons are non-relativistic and energy modulations are indeed equivalent to velocity modulations. As such, drift regions can replace dispersive sections.

Similarly, introducing an energy modulation onto the beam in a klystron which adds power at an appropriate frequency can be done by a buncher cavity without a permanent magnetic device such as an undulator as in the various FEL methods.

By adding an additional buncher cavity and drift to the klystron we can then adapt the EEHG concept to a klystron-inspired architecture. Then a much higher harmonic content can be imprinted on to the bunch. Figure 29 shows the general layout of our concept which is unique for our desired frequency range.

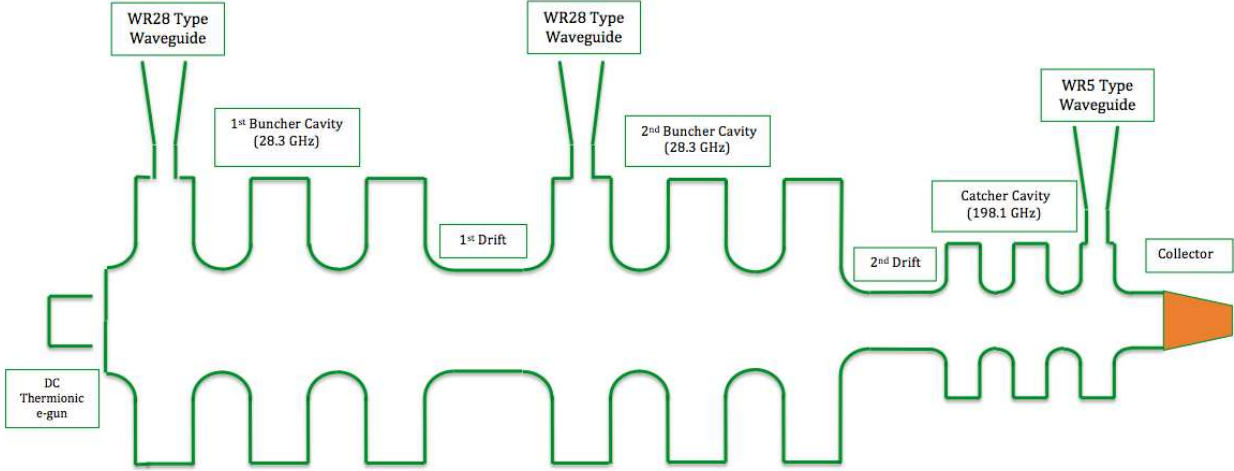


Figure 29: Scheme of the miniature THz klystron. The buncher cavities are resonant to 28.3 GHz and the catcher cavity is resonant at 198.1 GHz.

5.3.1. Adaptation of the Theory of EEHG Method into the Compact Klystron-inspired THz System

We first focus on the theory of our concept. As a starting point, we looked toward the EEHG method's theory in G. Stupakov's paper [ibid, 24]. Then, we have adapted the equations for energy modulation in the relativistic EEHG method into velocity modulation for the nonrelativistic THz "klystron" concept. Below are the theoretical steps to this adaptation.

We assume an initially DC beam (no density modulation) that has a small random velocity distribution with a variance σ_ϑ and we use the dimensionless velocity deviation as $q = (\vartheta - \vartheta_0)/\sigma_\vartheta$. The initial distribution function is $f(q) = N/(2\pi)^{-1/2}\exp(-q^2/2)$ where N is the number of particles per unit length. The RF fields of the first buncher cavity periodically modulate the beam energy (velocity). The final dimensionless velocity deviation q' is related to the initial q

by the equation $q' = q + M \sin(\omega_{RF}t)$ where $M = \Delta\vartheta/\sigma_\vartheta$. The distribution function then becomes

$$f(t, q) = N/(2\pi)^{-1/2} \exp(- (q - M \sin(\omega_{RF}t))^2 / 2) \quad (27)$$

After the beam goes through the “first drift” with length D , time becomes $t' = t + q (\sigma_\vartheta/\vartheta_0) (D/\vartheta_0)$, and the distribution function as becomes

$$f(\chi, q) = N/(2\pi)^{-1/2} \exp(- (q - M_1 \sin(\chi - qL))^2 / 2) \quad (28)$$

where $\chi = \omega_{RF}t$ and $L = \omega_{RF} (\sigma_\vartheta/\vartheta_0) (D/\vartheta_0)$.

This, effectively, is the equation that we derive for a typical klystron. We then choose the values of M and D , to maximize the power in the fundamental, or if desired a harmonic. If we expand the exponential term along the time axis it also can be seen the origin of the harmonics. Such an expansion would give Bessel functions of various orders for the various harmonics.

We then repeat the process with a second buncher cavity operating at an amplitude M_2 with a phase relative to the first cavity of ϕ , followed by a drift of length D_2 . Then, the final, rather complicated, distribution function becomes

$$f_2(\chi, q) = \frac{N}{\sqrt{2\pi}} \exp \left[-\frac{1}{2} \left(q - M_2 \sin(\omega\chi - \omega L_2 q + \phi) - M_1 \sin(\chi - (L_1 + L_2)q + M_2 L_1 \sin(\omega\chi - \omega L_2 q + \phi)) \right)^2 \right] \quad (29)$$

where $\omega = \omega_{RF} t$, $L_1 = \omega_{RF} (\sigma_{\vartheta}/\vartheta_0) (D_1/\vartheta_0)$, $L_2 = \omega_{RF} (\sigma_{\vartheta}/\vartheta_0) (D_2/\vartheta_0)$. Note, we have assumed that the frequencies of both buncher cavities are the same; however, this is not a requirement and arbitrary frequencies can be chosen if desired.

Because of the complexity of the distribution function there are no simple and clear relationships between the four major parameters. We can, however, make reasonable choices that will lead us to an approximate solution that in turn can be used in an optimization routine to find the desired set points required to achieve a desired harmonic. For instance we wish that the length of the overall device be relatively short. This implies a relatively large value of M_I when compared to the beam centroid energy. M_I values that would give a modulation of roughly 15% of the beam centroid energy are plausible starting points. Next we need to decide what harmonic to aim for.

In our example we wish to maximize the 7th harmonic. Shearing via the velocity modulation should therefore result in roughly 7 energy bands in the distribution. This, together with the beam centroid energy and modulation depth then gives us an initial value for the first drift length D_I . Similarly the modulation depth imparted by the second buncher should be sufficient so that the following drift is not terribly long. A number of roughly 5% of the beam centroid energy will provide plenty of modulation depth. The following drift length can then be approximated. This is done by determining the length it takes a maximally modulated electron to drift $\frac{1}{4}$ of the RF wavelength relative to a particle with the centroid energy. With these initial values in hand we are ready to optimize the solution.

A script was developed, written to operate in Igor Pro [53] is used to help calculate and define the drift lengths according to the determined values for modulation and offset. As a validation of our code we first compared the output of the algorithm to those calculated in the literature for the classical EEHG system. Figure 30 is the result of this scan, and is identical to that of the work presented by G. Stupakov.

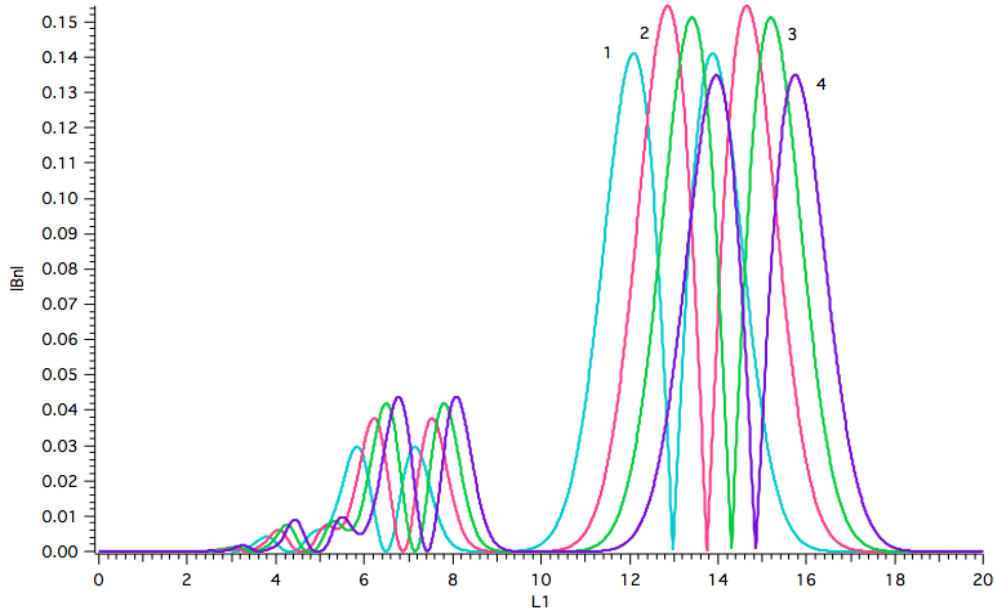


Figure 30: For Stupakov’s EEHG case, we illustrate the bunching factor for $k = 10$ as a function of parameter L_1 for four different values of L_2 : 1- $L_2 = 1.18$, 2- $L_2 = 1.25$, 3- $L_2 = 1.3$, 4- $L_2 = 1.35$. (as in Stupakov’s paper)

After the validation of our code for the known EEHG case, we then chose appropriate dimensionless amplitudes M_1 and M_2 that would allow us, by variation of the drift lengths, to readily explore the parameter space that spans the 5th through 12th harmonics. The scans showed that for our chosen amplitudes for M_1 and M_2 the 7th harmonic gave us the best performance. Therefore, we chose the 7th harmonic of the main resonance frequency for our output frequency. In our input file we chose initial modulations of 15% modulation for the first buncher and 5% modulation for the second buncher.

We chose for our seed frequency applied to the bunches to be 28.3 GHz as such sources are readily available at the power levels we desire. The basic cavity and seed parameters are given in Table 5.

Table 5: Basic parameters of the System (Details to be described later.)

Parameter	Value
Frequency of the Input Electromagnetic Radiation to seed the System	28.3 GHz
Frequency of the 1 st Buncher Cavity	28.3 GHz
Frequency of the 2 nd Buncher Cavity	28.3 GHz
Average Power of the Input Microwave Seed Signal for the first buncher cavity	1W
Frequency of the output electromagnetic radiation	198.1 GHz

Next, we chose, the output electromagnetic radiation frequency to be 198.1 GHz, the 7th harmonic of the 28.3-GHz seed. We assumed that we generated a 5-kV electron beam (particle velocity is $0.14c$) from a standard DC, thermionic gun.

The electron beam is modulated to a depth of 15% across the first buncher cavity and then allowed to drift 1.21 cm which we can calculate easily as the following.

For the fundamental frequency which is 28.3 GHz, the period is 35 ps. In our case, since $\beta = 0.14$ then the drift length in one period becomes 1.48 mm. When we multiple this value with the first effective length constant which is 8.2, it gives the required length of the first drift length and equals to 1.21 cm. Similarly the second drift becomes 1.05 cm when the effective length constant is 7.1.

The following figures illustrate, over one buncher RF period, the evolution of the phase space of the beam as it travels through the system for parameters discussed above. The phase space evolves as expected, described in detail below.

The longitudinal phase space at various locations in the process is shown in Figure 31. Figure 31 (a) shows the phase space immediately after passing the first buncher cavity of the THz klystron. It shows the modulation effect on the electron beam. The phase space following the first drift is shown in Figure 31 (b). As we expected, there is significant shearing of the phase space and one is left with roughly 7 effective energy bands. Figure 31 (c) shows the phase space. Finally, Figure 31 (d) shows the beam phase space following the 2nd drift. There is clear density modulation only the length of the beam. This will allow us to use higher harmonics (7th harmonic in our case).

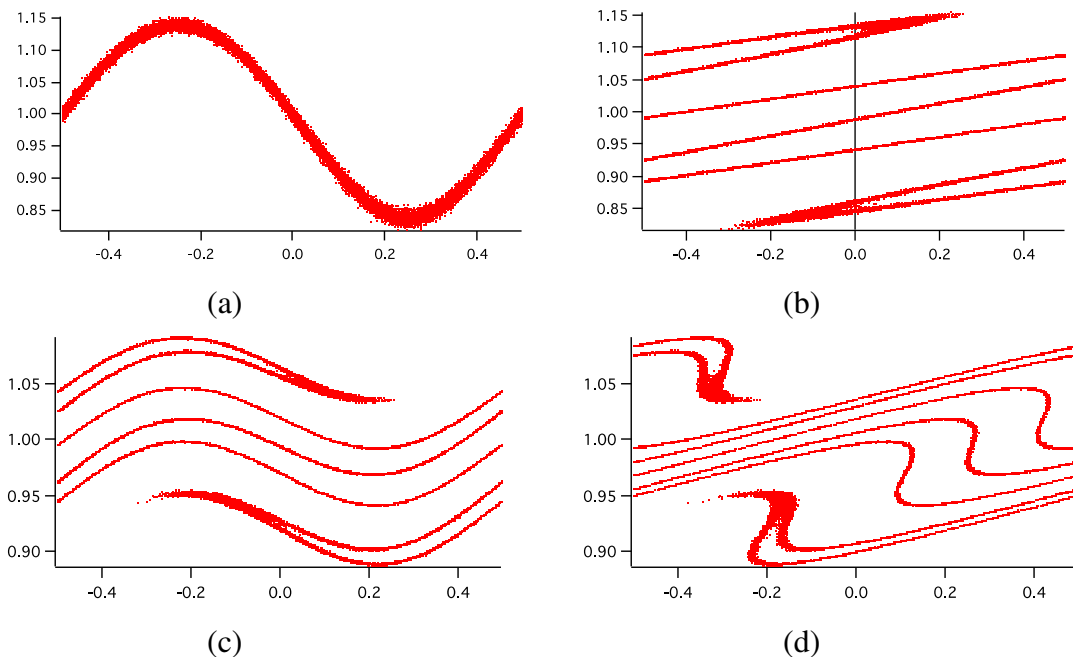


Figure 31: The longitudinal phase space of an electron bunch during velocity modulation a) The phase space after interaction with the 1st buncher cavity (28.3 GHz) b) following shearing through the 1st drift space c) The phase space after interaction with the 2nd buncher cavity (198.1 GHz) d) following shearing through the 2nd drift space

Furthermore, the particle distribution has been analyzed and is shown in Figure 32. Figure 32 (a) shows the histogram of the particle distribution presented in Figure 31 (b). The Fast Fourier Transformation of the particle density histogram (to convert the signal from the time domain into the frequency domain) is shown and computed in Figure 32 (b). Figure 33 shows similar graphs but this time for the Figure 31 (d).

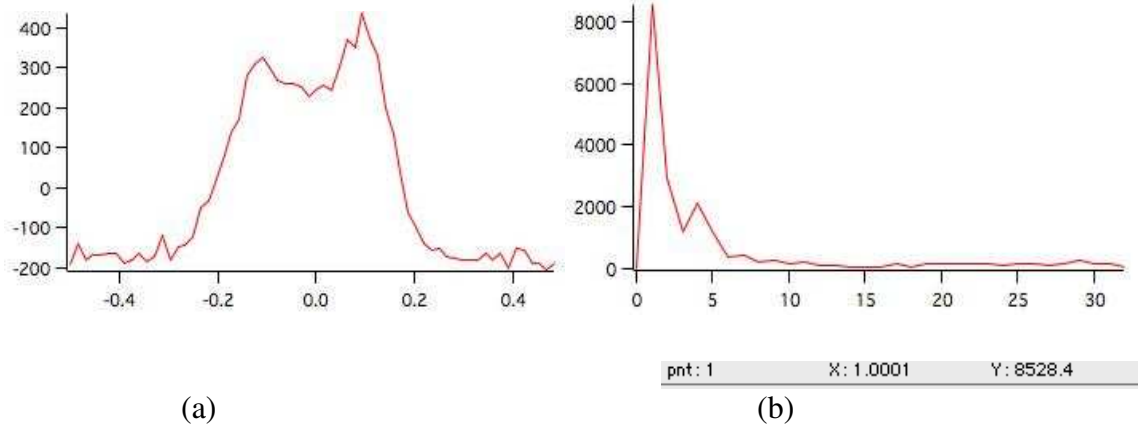


Figure 32: a) The histogram of the particle distribution as shown in Figure 31 (b). b) The FFT of the particle distribution shown in (a).

Figure 32 (b) indicated the presence of the fundamental frequency after the first buncher, which is expected, but very low signals at the higher harmonics. The results are very different in Figure 33 (b). Here see that the maximum peak value is, as desired, at the 7th harmonic (198.1 GHz) of the fundamental frequency. This shows us that the maximum gain is in the 7th harmonics as we designed.

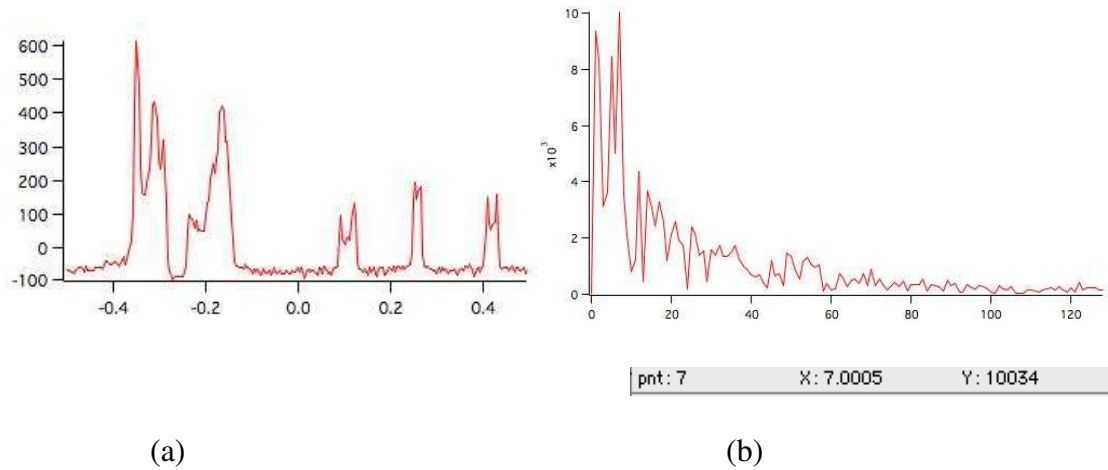


Figure 33: a) The histogram of the particle distribution as shown in Figure 30 (d). b) The FFT of the particle distribution as shown in (a).

5.3.2. RF Design of the THz Klystron

Having shown that in theory the design is plausible we next turn our attention to more practical details, in particular, the design of the buncher and catcher cavities. The code SUPERFISH was once again used to develop the basic designs for both the 28.3-GHz buncher cavities and the 198.1-GHz catcher cavity.

A high shunt impedance is desirable in both buncher and catcher cavities. In the buncher cavity it reduces the power and length required to generate the requisite fields, and in the catcher it reduced the overall length and therefore the number of cells that must be constructed. Therefore, we made our designs in order to get the higher shunt impedance ($\sim 90 \text{ M}\Omega/\text{m}$) for Ka-band frequency range (26.5 – 40 GHz) and also ($\sim 300 \text{ M}\Omega/\text{m}$) for G-band frequency (110 – 300 GHz).

Our challenge here is that the velocities are low and the frequencies high, this implies short cavity lengths and therefore more cells to achieve the overall required shunt impedance for a given input

power and modulation depth. We looked at two different cases, a standing wave structure with a longitudinal phase advance per cell of π , and a travelling wave structure with longitudinal phase advance per cell of $2\pi/3$. We also study the impact of the transit time factor as the cavities would be much shorter than cavities designed for relativistic beams. The impact of the transit time factor T is sizable for the slow electrons by [ibid, 26]

$$r_{sh} = \frac{(V_0 T)^2 L}{p} \quad (30)$$

As expected the effective shunt impedance increases with the square root of the frequency. We do, however, take a significant variation in the effective impedance for the low β cavity (0.14c for a 5 keV kinetic energy electron). The results for each case are given in Tables 6 and 7 and also represented in Figure 34.

Table 6: SW and TW cavity parameters for maximum relative velocity ($\beta = 1$)

Parameters	Values					
Cavity Structure Type	Standing Wave (SW)			Travelling Wave (TW)		
Phase advance per cell [Radians]	π			$2\pi/3$		
Relative Velocity	1					
Resonance Frequency Range	X-band	Ka-band	G-band	X-band	Ka-band	G-band
Resonance Frequency [GHz]	11.7	28.3	198.1	11.7	28.3	198.1
Iris Radius to Wavelength Ratio	0.1					
Shunt Impedance [$M\Omega/m$]	107	167	441	110	173	465
Quality Factor	8510	5486	2065	6456	4681	1788

Table 7: SW and TW cavity parameters for maximum relative velocity ($\beta = 0.14$)

Parameters	Values					
	Standing Wave (SW)			Travelling Wave (TW)		
Cavity Structure Type	Standing Wave (SW)			Travelling Wave (TW)		
Phase advance per cell [Radians]	π			$2\pi/3$		
Relative Velocity	0.14					
Resonance Frequency Range	X-band	Ka-band	G-band	X-band	Ka-band	G-band
Resonance Frequency [GHz]	11.7	28.3	198.1	11.7	28.3	198.1
Iris radius to wavelength ratio	0.1					
Shunt Impedance [$M\Omega/m$]	60.1	93.7	248.3	75.9	118.3	313.6
Quality Factor	2146	1410	504	1371	723	336

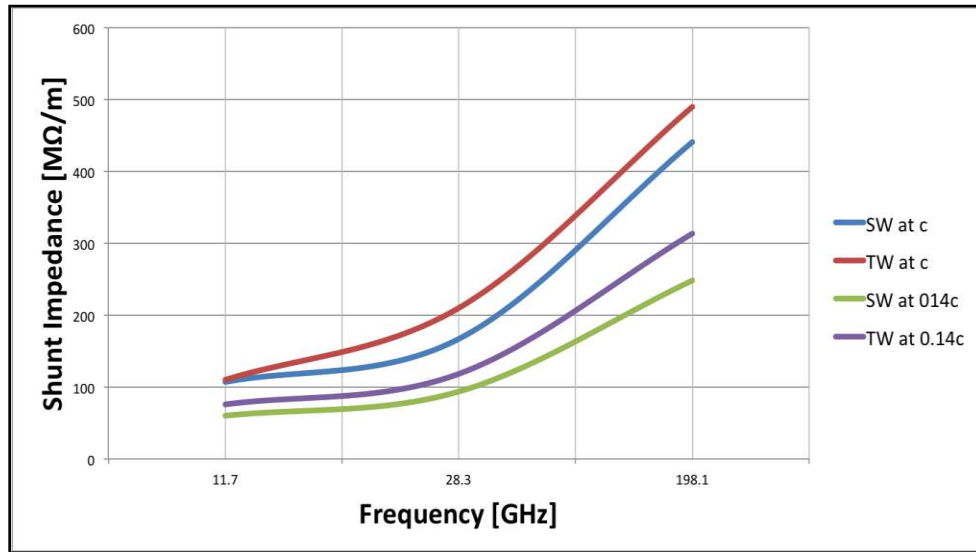
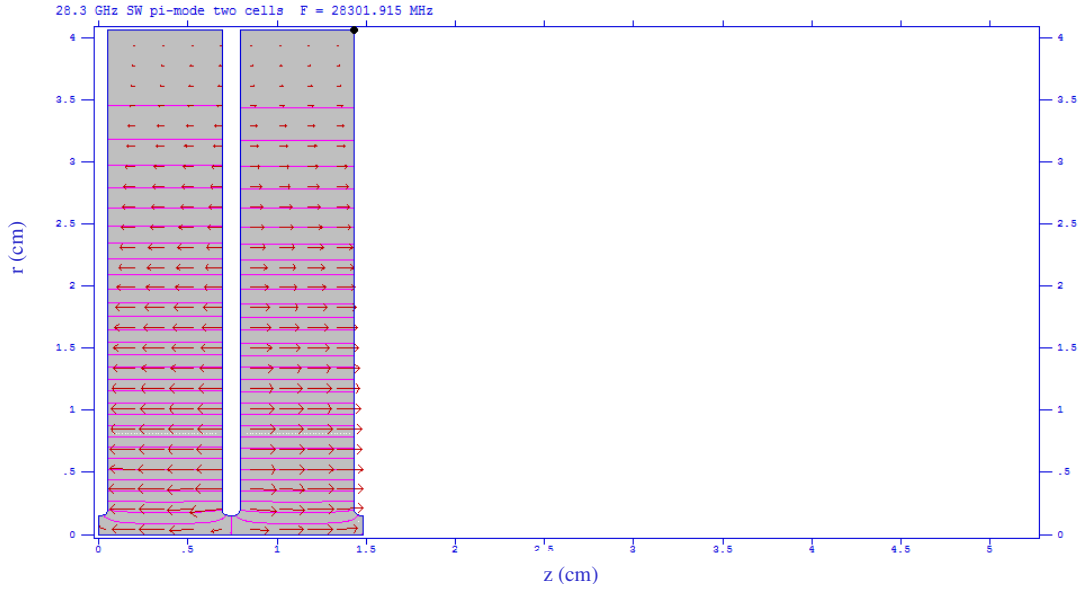


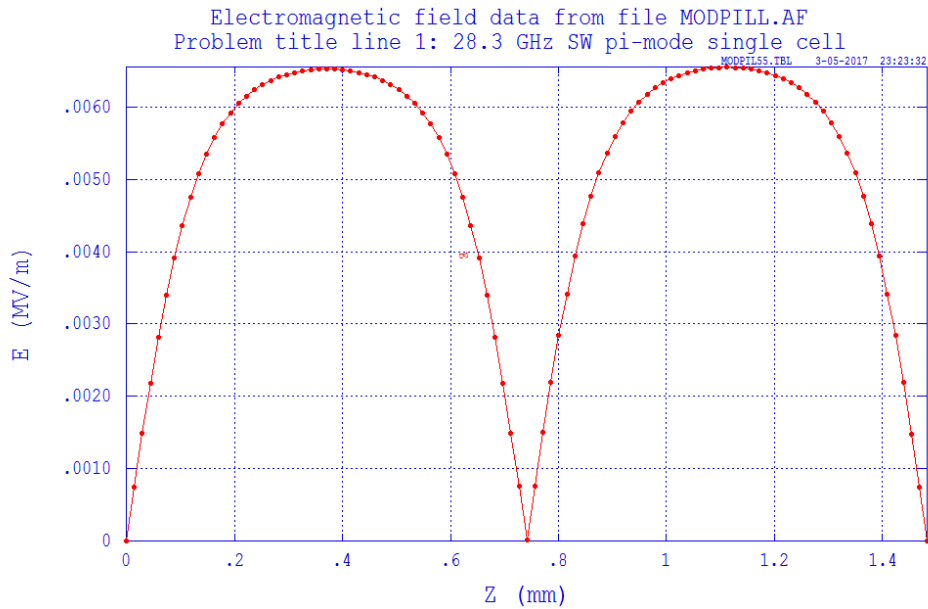
Figure 34: Shunt impedance versus frequency scaling of SW and TW structures for $\beta = 1$ and $\beta = 0.14$

In our design we chose to use two step buncher section design to further increase our modulation before our catcher cavity. These buncher cavities are both operating at the fundamental frequency – 28.3 GHz in the π -mode. The beam has 15 % modulation in the 1st buncher and 5% in the 2nd

buncher. Figure 35 shows the geometry for these identical cavities simulated using SUPERFISH. The electric field distribution at 28.3 GHz for the π -mode standing-wave cavity and the design parameters are also given in Table 8.



(a)



(b)

Figure 35: a) The 2-cell geometry of 1st and 2nd (identical) buncher cavity designs and b) the field distribution (operating as first buncher cavity in our configuration) operating at 28.3 GHz in the π -mode

Table 8: Design parameters of the π -mode standing-wave (SW) buncher cavity

Design Parameters	Values
Iris Radius, r [mm]	0.15
Cavity Radius, R [mm]	4.05
Single Cell Length, L [mm]	0.74
Disc Thickness, a [mm]	0.05

Table 9 shows the design parameters of the π -mode standing-wave (SW) catcher cavity using SUPERFISH.

Table 9: Design parameters of the π -mode standing-wave (SW) catcher cavity

Design Parameters	Values
Iris Radius, r [mm]	0.02
Cavity Radius, R [mm]	0.59
Single Cell Length, L [mm]	0.10
Disc-thickness, a [mm]	0.01

In order to increase our extracted power efficiency we chose a higher shunt impedance a $2\pi/3$ -mode travelling-wave (TW) as our catcher cavity at the end of the structure. For practical considerations in the TW case we kept the ratio of disc-thickness and inner radius same as π -mode SW case. Figure 36 shows the design geometry and field distribution of the buncher cavity which operating at 198.1 GHz and well fits in TW structures at $2\pi/3$ -mode. The design parameters are given in Table 10.

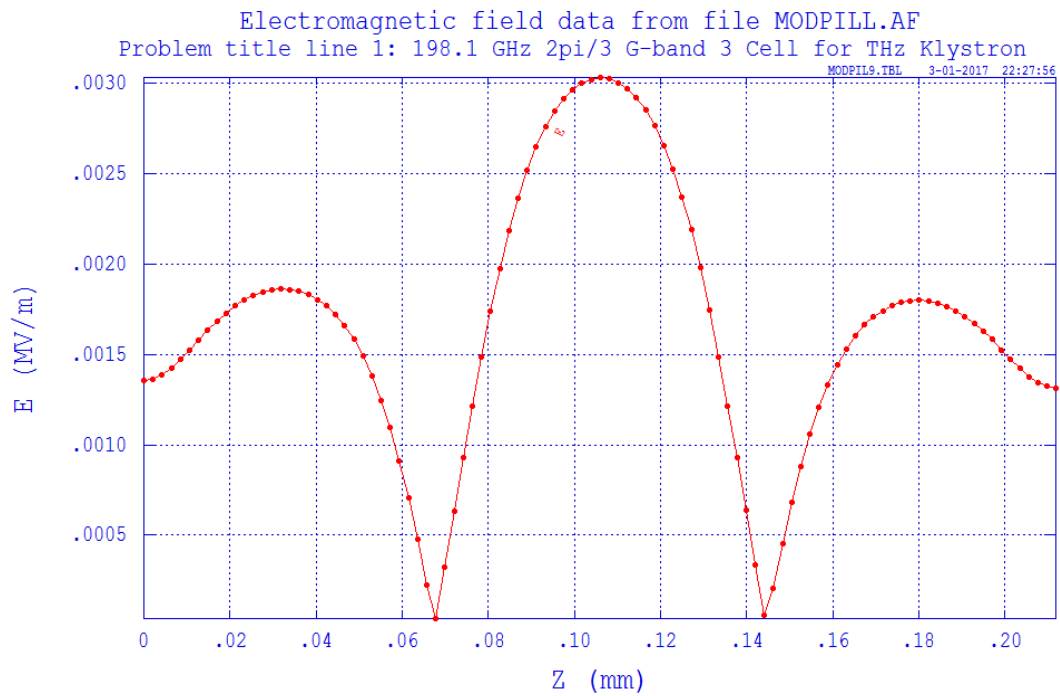
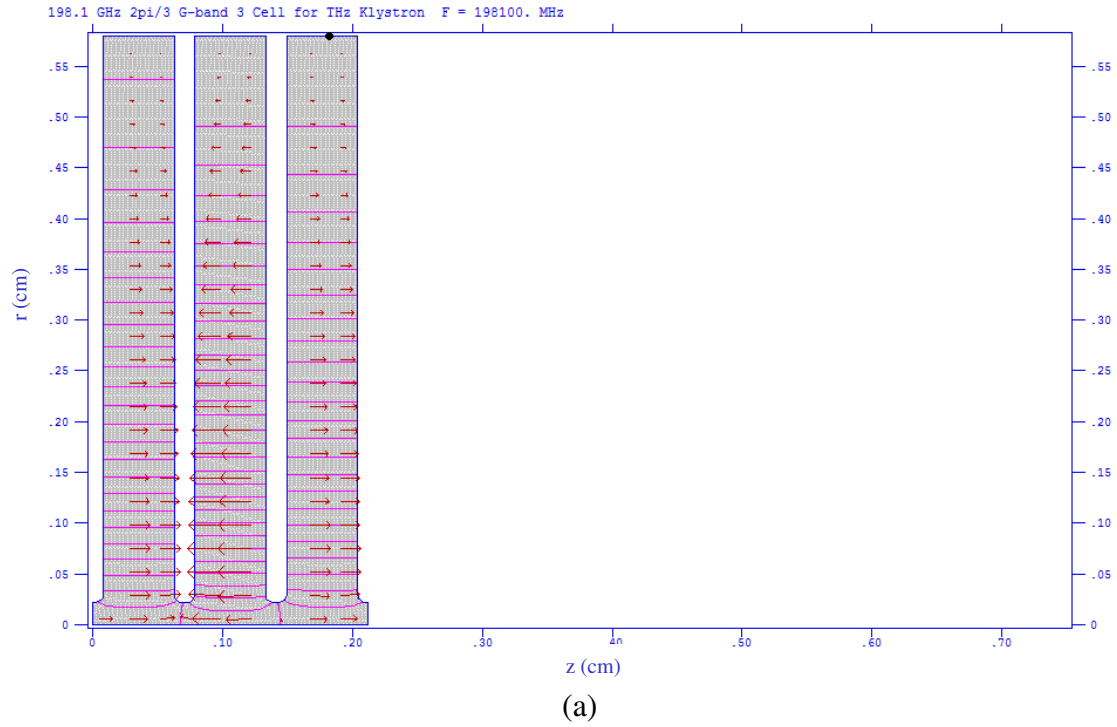


Figure 36: a) The 3-cell geometry of catcher cavity design b) the field distribution (operating as first buncher cavity in our configuration) operating at 198.1 GHz in the $2\pi/3$ -mode in travelling-wave (TW) structures.

Table 10: Design parameters of the $2\pi/3$ -mode traveling-wave (TW) catcher cavity

Design Parameters	Values
Iris Radius, r [mm]	0.02
Cavity Radius, R [mm]	0.58
Single Cell Length, L [mm]	0.07
Disc-thickness, a [mm]	0.01

As seen in the figures that are generated by using SUPERFISH, all of our design results are for uncoupled structures. In Table 11, we presented the design parameters of the final structure.

Table 11: The design parameters of the full system (2 buncher cavities, 1 catcher cavity and 2 drift spaces)

Parameters	Values
1 st Buncher cavity cell number	1
2 nd Buncher cavity cell number	2
Catcher cavity cell number	3
1 st drift space length [m]	0.012
2 nd drift space length [m]	0.001

We also calculated the available output power for a given electron gun parameters by considering the related modulation values for each buncher cavities. The parameters that are used for the power calculation of the full structure are given in Table 12. We achieved 4 W output power at the end of the catcher cavity as can be seen in Figure 37.

Table 12: Input and output parameters for the THz klystron

Parameters	Values
Electron gun input voltage [kV]	5
Electron velocity [c]	0.14
RF input power [W]	1
Shunt impedance of the buncher cavity [MΩ/m]	93.7
Shunt impedance of the catcher cavity [MΩ/m]	313.6
Beam Current [A]	0.2

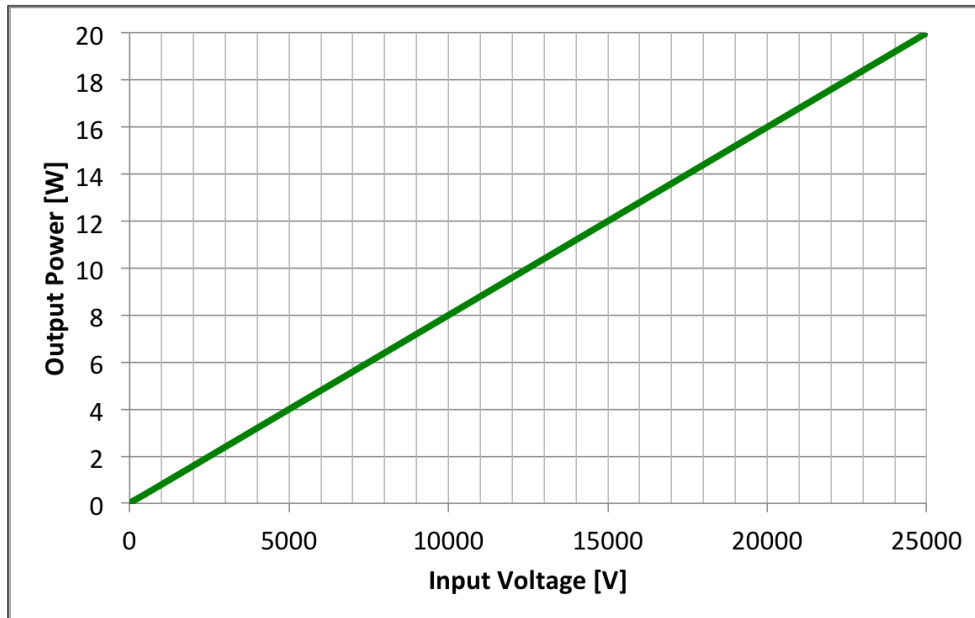


Figure 37: Theoretical small-signal gain for THz klystron

Furthermore, in order to validate our theoretical results with the simulation method we used a klystron design code which is called AJDISK [54]. AJDISK is a Stanford Linear Accelerator Laboratory (SLAC) small-signal gain simulation code to analyze a klystron design. In our simulation steps, we used our cavity design parameters as previously given as an input of the

simulation. We also used the electron gun and cavity parameters as given in Table 12. As can be seen in Figure 38, we can achieve 4 W power at the end of this structure. This shows us that our theoretical and simulation results are very consistent and promising to build the Klystron-inspired THz source.

In addition, using another electron source which has higher input voltage can increase our available power from this compact structure (Fig.37). Moreover, more advanced structures as buncher and catcher cavities allow us to improve our output parameters and achieve higher power levels at higher frequencies.

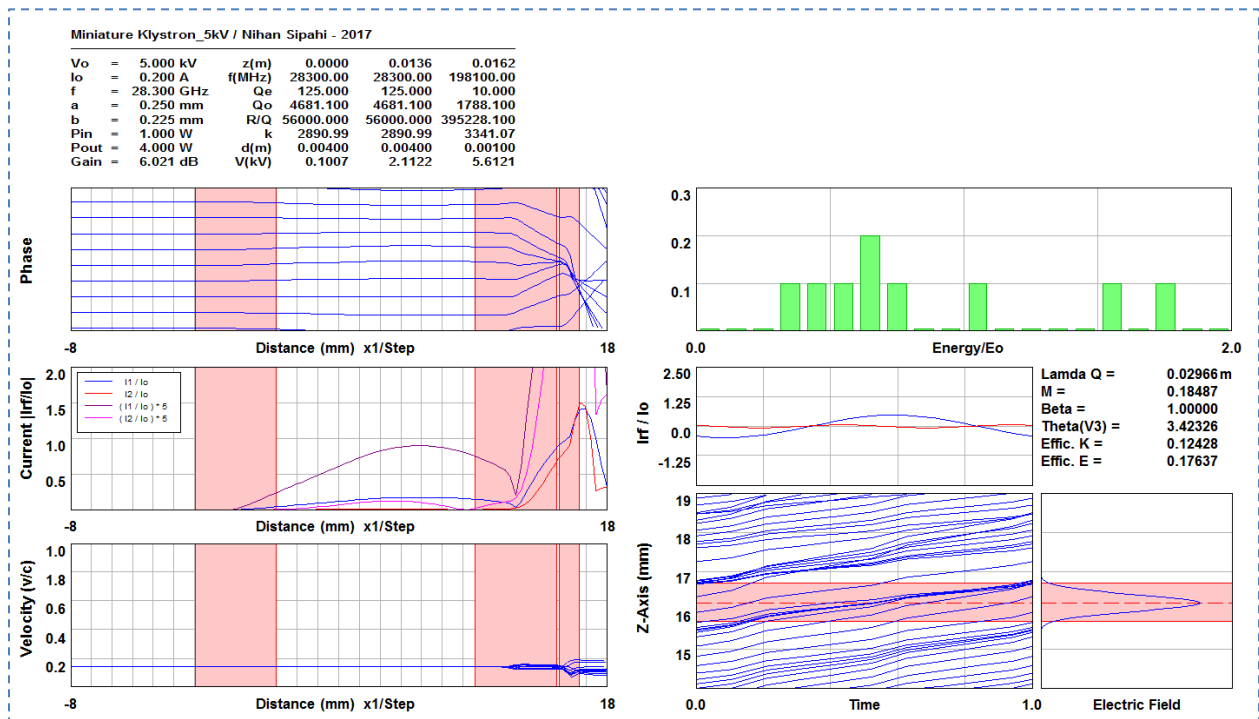


Figure 38: AJDISK small-signal gain results

6. CONCLUSIONS

In this dissertation, we studied

- increasing the intensity and efficiency, yet also decreasing the size and complexity, of a powerful electron source while maintaining a high-quality beam
- devising a new, compact device to generate high powers of narrow-band, electromagnetic radiation lying in a band between the infrared and microwave regimes as an example for generating other such frequencies in this band.

The intent was to show that the generation of high-energy electrons and novel electromagnetic radiation sources are not necessarily independent of one another. An electromagnetic wave and an electron beam both can be characterized by their peak and average power. This power and the characteristics from each genre of source can contribute to the advancement of other sources – namely electron beams and novel electromagnetic radiation sources.

In this study, we conceptualized and designed the high-power electron-beam sources that could ultimately be used either directly or be used for the generation of x-rays.

The first part of the dissertation was about developing the electromagnetic design and performing the initial beam dynamics simulations to provide a proof-of-principle of our challenging concept for the integrated electron gun to generate high-power electron beams. In the design step of the integrated concept, we redesigned the regular ILC/XFEL cell to use as a gun cell in the main accelerator structure. Then, we also designed a cathode assembly part that includes an RF choke

to eliminate the field between cold and hot environment and a 70K shield to protect the cathode and integrate it with the main accelerating structure. After having promising results from the detailed electromagnetic design of the integrated system, we then studied the initial beam dynamics of the system. These results showed that our integrated design is capable of achieving higher energies with high average power in a compact manner. As a next step, the intensive beam dynamics that focuses on the cathode and the electron gun needs to be studied to analyze the emission process and back-bombardment effects in details before starting the fabrication process.

The second part of the dissertation was about the extraction of electromagnetic radiation from a non-relativistic electron beam. This proof-of-principle relied on a klystron-like architecture and the adaptation of a frequency up-conversion technique originally conceived for relativistic electron beams and soft-to hard-x-ray frequencies, to the non-relativistic electron-beam case and THz frequencies.

In this part of the dissertation, we first analyzed the EEHG method to adapt it for our concept. After adapting this method for the non-relativistic case, we then studied the design of the RF structures for the klystron-inspired THz source. In order to calculate the available power in this compact design, we used both analytical and computational techniques. Our results show that klystron-inspired, compact concept is capable of achieving high powers at THz frequency range. As a next step, the RF design needs to be performed in 3D codes to better analyze the secondary effects.

In conclusion, this dissertation has detailed the electromagnetic design of compact high power electron sources for both superconducting and normal conducting technologies. Additionally, the beam dynamics simulations have been performed for both superconducting and normal conducting electron sources. These results, which have been obtained using several different electromagnetic design and particle in cell codes, can be useful for the development of both superconducting and normal conducting compact electron sources that have capabilities not available before - and significantly contributes to the field of accelerator physics.

REFERENCES

- [1] Accelerators and Beams: Tools of Discovery and Innovation, 4th Edition, American Physical Society <https://www.aps.org/units/dpb/news/edition4th.cfm>

- [2] Hamm, Robert Wray, and Marianne Elizabeth Hamm, eds. *Industrial accelerators and their applications*. World Scientific, 2012.

- [3] Gewartowski, James W., and Hugh A. Watson. *Principles of electron tubes: including grid-controlled tubes, microwave tubes, and gas tubes*. van Nostrand, 1965.

- [4] Brookhaven National Laboratory website : <https://www.bnl.gov/world/>

- [5] Xu, Wencan, et al. "First beam commissioning at BNL ERL SRF gun." (2015)

- [6] Helmholtz-Zentrum Berlin-HZB Laboratory website : https://www.helmholtz-berlin.de/index_en.html

- [7] Abo-Bakr, M., et al. "Status of the HZB ERL Project bERLinPro." *IPAC 14* (2014): 340.

- [8] Helmholtz-Zentrum Dresden-Rossendorf-HZDR Laboratory website : <https://www.hzdr.de>

- [9] Teichert, Jochen, H. Buetting, and P. Evtushenko. "A Superconducting Photo-Injector with 31/2-Cell Cavity for the ELBE Linac." Proc. of EPAC. 2004.

- [10] Xiang, Rong, et al. "Experimental investigations of DC-SC photoinjector at Peking University." *Nuclear Instruments and Methods in Physics Research Section A: Accelerators, Spectrometers, Detectors and Associated Equipment* 528.1 (2004): 321-325.
- [11] Boulware, Chase, et al. "4 K Superconducting Linac for Commercial Applications." North American Particle Accelerator Conf. (NAPAC'16), Chicago, IL, USA, October 9-14, 2016. JACOW, Geneva, Switzerland, 2017.
- [12] Niowave, Inc. website <http://www.niowaveinc.com>
- [13] A. Grassellino, A. Romanenko, D. Sergatskov, O. Melnychuk, Y. Trenikhina, A. Crawford, A. Rowe, M. Wong, T. Khabiboulline and F. Barkov, "Nitrogen and argon doping of niobium for superconducting radio frequency cavities: a path way to highly efficient accelerating structures", *Supercond. Sci. Technol.* 26, 102001 (2013).
- [14] Kazakevich, Grigory, and Rolland Johnson. "High-power magnetron RF source for superconducting Linacs of ADS and intensity-frontier projects." *Presented at 11th International Topical meeting on Nuclear Applications of Accelerators*. No. FERMILAB-CONF-13-314-AD-TD. 2013.
- [15] B. Chase, R. Pasquinelli, E. Cullerton, P. Varghese, "Precision Vector Control of a Superconducting RF Cavity driven by an Injection Locked Magnetron", Patent pending.
- [16] S. Kazakov, "How to Eliminate a Copper Coating and to Increase an Average Power of Main Coupler", TUPO009, Proceedings of SRF 2011, Chicago IL.

- [17] Kephart, Robert, Brian Chase, Swapan Chattopadhyay, Ivan Gonin, Anna Grassellino, Sergey Kazakov, Nihan Sipahi et al. "SRF, Compact Accelerators for Industry & Society." In *17th International Conference on RF Superconductivity (SRF2015), Whistler, BC, Canada*. 2015.
- [18] Richard, F., et al. "TESLA Technical Design Report Part I: Executive Summary." *arXiv preprint hep-ph/0106314* (2001).
- [19] Phinney, Nan, Nobukasu Toge, and Nicholas Walker. "ILC reference design report." *arXiv preprint arXiv:0712.2361* (2007).
- [20] Altarelli, Massimo, et al. "The technical design report of the European XFEL." *Chapter 4* (2006): 2006-097.
- [21] Steer, Brian, et al. "Extended-Interaction Klystron Technology at Millimeter and Submillimeter Wavelengths." (2009).
- [22] Varian, Russell H., and Sigurd F. Varian. "A high frequency oscillator and amplifier." *Journal of Applied Physics* 10.5 (1939): 321-327.
- [23] Tsimring, Shulim E. *Electron beams and microwave vacuum electronics*. Vol. 191. John Wiley & Sons, 2006.
- [24] Xiang, Dao, and Gennady Stupakov. "Echo-enabled harmonic generation free electron laser." *Physical Review Special Topics-Accelerators and Beams* 12.3 (2009): 030702.
- [25] Jackson, J. David. *Electrodynamics*. Wiley-VCH Verlag GmbH & Co. KGaA, 1975.

- [26] Wangler, Thomas P. RF Linear accelerators. John Wiley & Sons, 2008.
- [27] Padamsee, Hasan. RF Superconductivity: Volume II: Science, Technology and Applications. John Wiley & Sons, 2009.
- [28] T. Sipahi, M.Sc. Thesis "Resonance Frequency Calculation of a Narrow Gap Reentrant Klystron Cavity" Ankara University, 2013.
- [29] N.Sipahi, M.Sc. Thesis "Equivalent Circuit Properties and Quality Factor of a Narrow Gap Reentrant Klystron Cavity, Ankara University, 2013.
- [30] K. Halbach and R.F. Holsinger, SUPERFISH - A Computer Program for Evaluation of RF Cavities with Cylindrical Symmetry, Part. Accel., 7 (1976) 213 - 222.
- [31] COMSOL Multiphysics Manual 5.1, see <https://www.comsol.com/comsol-multiphysics>
- [32] CST Microwave Studio: <https://www.cst.com/products/CSTMWS>
- [33] Gerigk, Frank. "Cavity types." arXiv preprint arXiv:1111.4897 (2011)
- [34] Pagani, C., et al. "Design criteria for elliptical cavities." 10th Workshop on RF Superconductivity, Tsukuba, Japan. Vol. 69. 2001.
- [35] Jana, Arup Ratan, Vinit Kumar, and Rahul Gaur. "Electromagnetic design optimization studies for $\beta g = 0.61$, 650 MHz elliptic superconducting radio frequency cavity." Proceedings of the Indian particle accelerator conference 2013.

- [36] Sipahi, Nihan, et al. "RF Design of a High Average Beam-Power SRF Electron Source." *7th International Particle Accelerator Conference (IPAC'16), Busan, Korea, May 8-13, 2016*. JACOW, Geneva, Switzerland, 2016.
- [37] Private Communication, Alexander Sukhanov, Fermilab, 2015
- [38] Sipahi, Nihan, et al. "RF Design of a 1.3-GHz High Average Beam Power SRF Electron Source." North American Particle Accelerator Conf. (NAPAC'16), Chicago, IL, USA, October 9-14, 2016. JACOW, Geneva, Switzerland, 2017.
- [39] Sipahi, Nihan, "Part 1: Detailed Electromagnetic Design of an Integrated and Compact 1.3 GHz Superconducting Radio Frequency (SRF) Electron Source, Technical Publications, Fermi National Laboratory (Fermilab), Batavia, IL, USA (under review)
- [40] Sipahi, Nihan, "Part 2: Initial Beam Dynamics Results of an Integrated and Compact 1.3 GHz Superconducting Radio Frequency (SRF) Electron Source, Technical Publications, Fermi National Laboratory (Fermilab), Batavia, IL, USA (under review)
- [41] Grudiev, A. V., et al. "Numerical Simulation of a Gridded Inductive Output Amplifier." *Proceedings of the 1996 European Particle Accelerator Conference (EPAC'96), Barcelona*. 1996.
- [42] M. Borland, SPIFFE (Space Charge and Integration of Forces For Electrons), version 4.5, Argonne National Laboratory, September 2, 2015
- [43] K. Flottmann, ASTRA: A Space Charge Tracking Algorithm, <http://www.desy.de/~mpyflo>

- [44] Edelen, Jonathan Paul. *Theory and mitigation of electron back-bombardment in thermionic cathode radio frequency guns*. Diss. Colorado State University, 2015.
- [45] Edelen, J. P., and J. R. Harris. "Current transmission and nonlinear effects in un-gated thermionic cathode RF guns." *arXiv preprint arXiv:1705.01386* (2017).
- [46] Borland, Michael, and Xiaowei Dong. "Simulation of Cathode Back-bombardment in a 100 MHz Thermionic RF Gun." *Proc. of LINAC*. 2010.
- [47] Gilmour, A. S. Klystrons, traveling wave tubes, magnetrons, crossed-field amplifiers, and gyrotrons. Artech House, 2011.
- [48] Cornetet, W. H. "A self-excited drift-tube klystron frequency multiplier for use in generating millimeter waves." *IRE Transactions on Electron Devices* 6.2 (1959): 236-241.
- [49] Fan, Junjie, and Yong Wang. "A 14 kW High-Power X-Band to Ka-Band Klystron Frequency Multiplier." *IEEE Transactions on Electron Devices* 61.6 (2014): 1854-1858.
- [50] Yu, Li Hua. "Generation of intense UV radiation by subharmonically seeded single-pass free-electron lasers." *Physical Review A* 44.8 (1991): 5178.
- [51] Dattoli, Giuseppe, et al. "Introduction to the physics of free electron laser and comparison with conventional laser sources." *arXiv preprint arXiv:1010.1647* (2010).
- [52] Saldin, Evgeny L., E. V. Schneidmiller, and Mikhail V. Yurkov. *The physics of free electron lasers*. Springer Science & Business Media, 2013.
- [53] Pro, Igor. "WaveMetrics." *Inc.: Lake Oswego, OR* (1996).

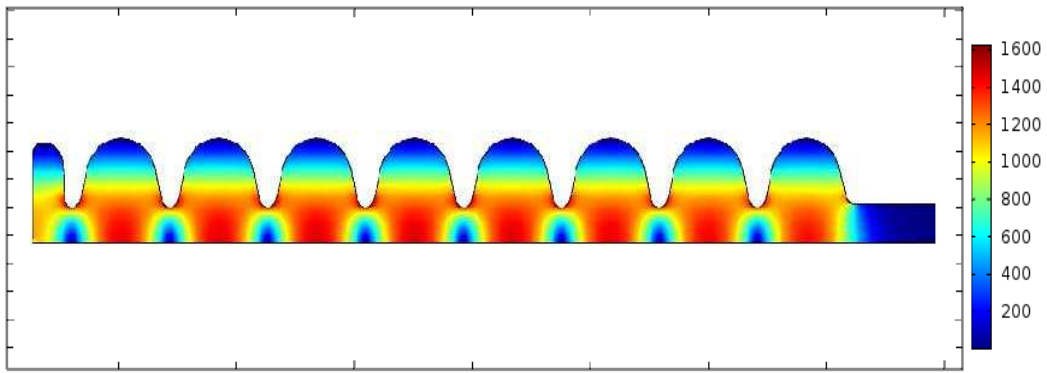
[54] Jensen, Aaron, Michael Fazio, Jeffrey Neilson, and Glenn Scheitrum. "Developing sheet beam klystron simulation capability in AJDISK." *IEEE Transactions on Electron Devices* 61, no. 6 (2014): 1666-1671.

[55] Emma, P., et al. "Transverse-to-longitudinal emittance exchange to improve performance of high-gain free-electron lasers." *Physical Review Special Topics-Accelerators and Beams* 9.10 (2006): 100702.

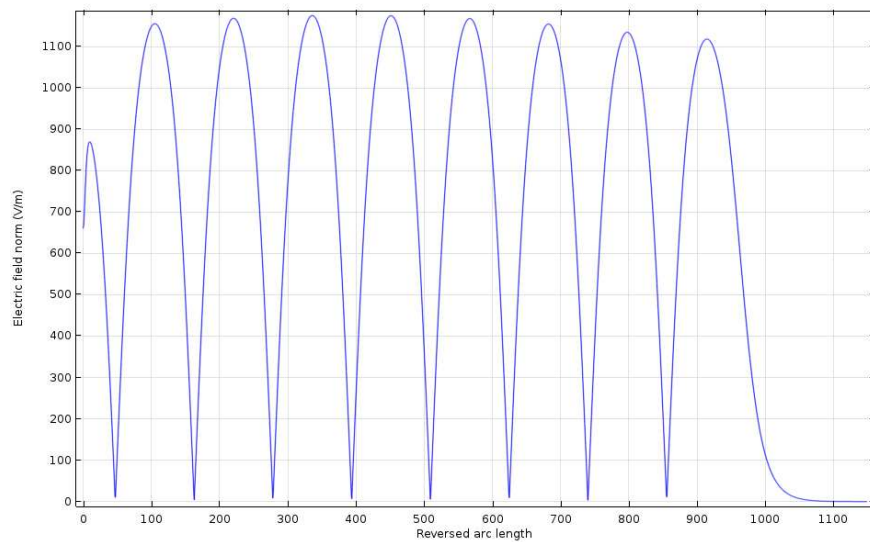
[56] Flottmann, K., Ph Piot, M. Ferrario, and B. Grigoryan. "The TESLA X-FEL injector." In *Particle Accelerator Conference, 2001. PAC 2001. Proceedings of the 2001*, vol. 3, pp. 2236-2238. IEEE, 2001.

APPENDIX A. ADDITIONAL DESIGN RESULTS FOR THE GUN-CELL AND OVERALL ACCELERATING STRUCTURE FOR THE COMPACT SRF ELECTRON SOURCE

In this part, the detailed simulation results in Comsol Multiphysics and CST Microwave Studio have been presented. Figures A.1 shows the simulation results of the 8.4-cell cavity design via COMSOL Multiphysics. As we expected, the results match with the SUPERFISH results.



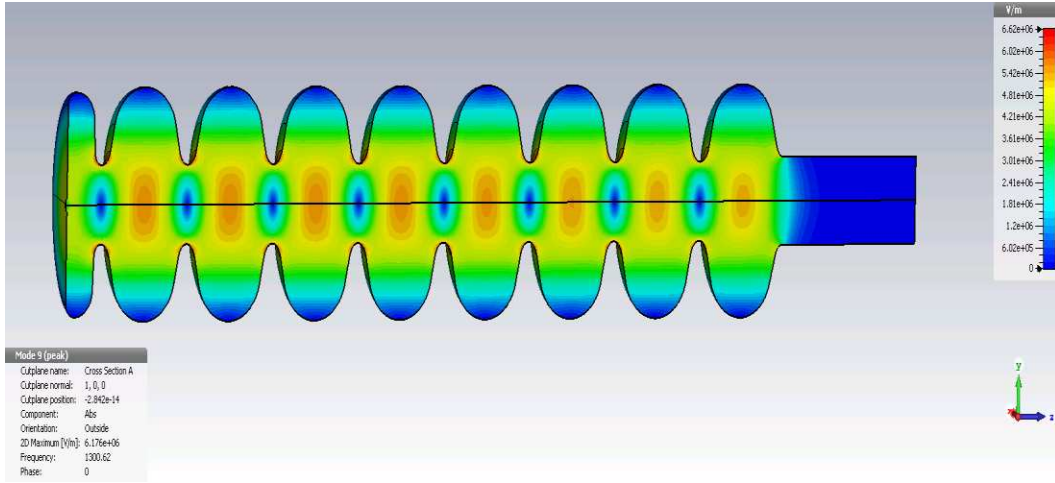
(a)



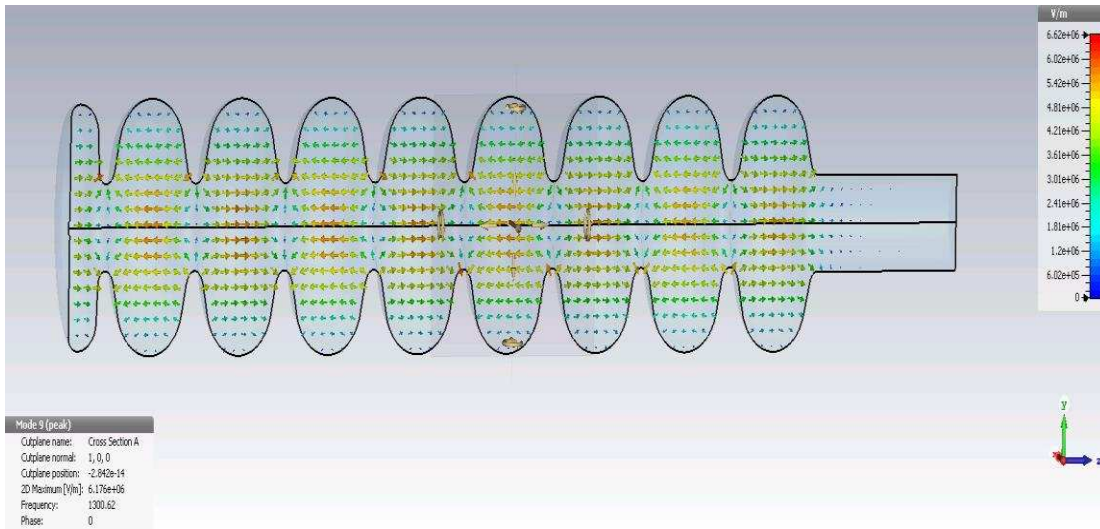
(b)

Figure A 1: a) The 8.4-cell structure's design geometry with the frequency matched to 1.3 GHz and its field map as generated in COMSOL Multiphysics. b) The electromagnetic field distribution of the 8.4-cell structure's design geometry as generated in COMSOL Multiphysics.

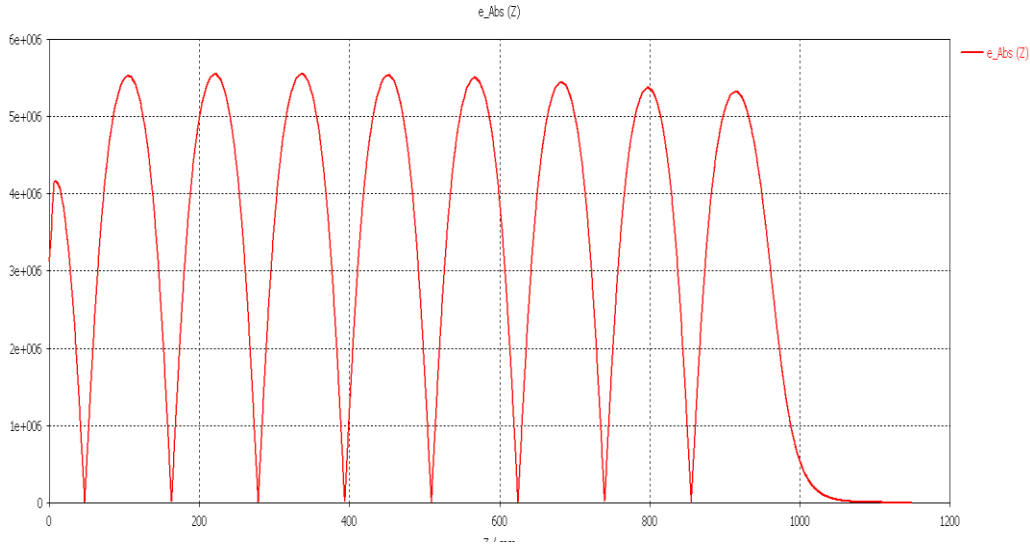
Moreover, Figures A 2 shows the CST MWS simulation results for 8.4-cell structure and they are also in good agreement with the results of the 2-D simulations obtained from both the SUPERFISH and COMSOL Multiphysics codes.



(a)



(b)



(c)

Figure A 2: a) The 8.4-cell structure's design geometry with the frequency matched to 1.3 GHz and the contour plot of the fields using CST MWS b) The 8.4-cell structure's design geometry with the view of the fields in the pi mode using CST MWS. c) The electromagnetic field distribution of the 8.4-cell accelerating section's design geometry as determined with CST MWS.

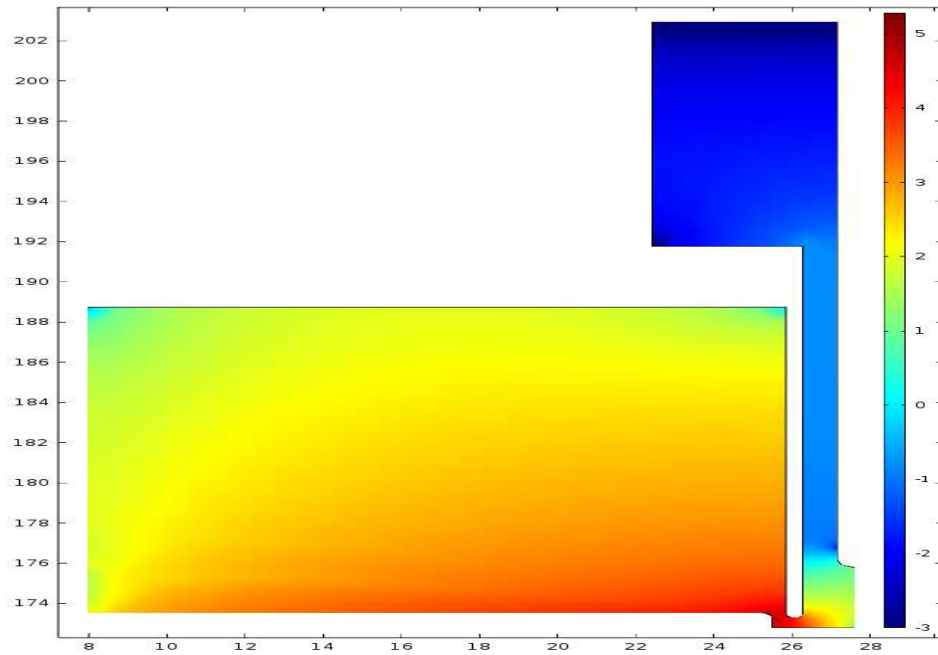
In Table A.1, we summarize and compare the results obtained from the three different simulation codes for these two different first cell lengths. While the normalization between the various codes is different, the resonant frequencies of the TM_{010} modes are quite similar as generated by SUPERFISH, COMSOL and CST. Differences can be attributed to the different meshing techniques used in the various codes; however, the values obtained are suitable for these particular RF design optimizations. Finally, as seen in Table A.1, the values of the field profiles are lower in the 0.3 cell case than in the 0.4 length cell case. Initial beam dynamics simulations show better overall performance in the 0.3 cell case, particularly in the area of beam loss; therefore, we have chosen to pursue this case in more detail.

Table A 1: The results of SUPERFISH, COMSOL Multiphysics and CST MWS for two different lengths of the first cell (0.3 and 0.4 of a full-cell length). The peak fields are calculated for 10-MeV output electron beam energy.

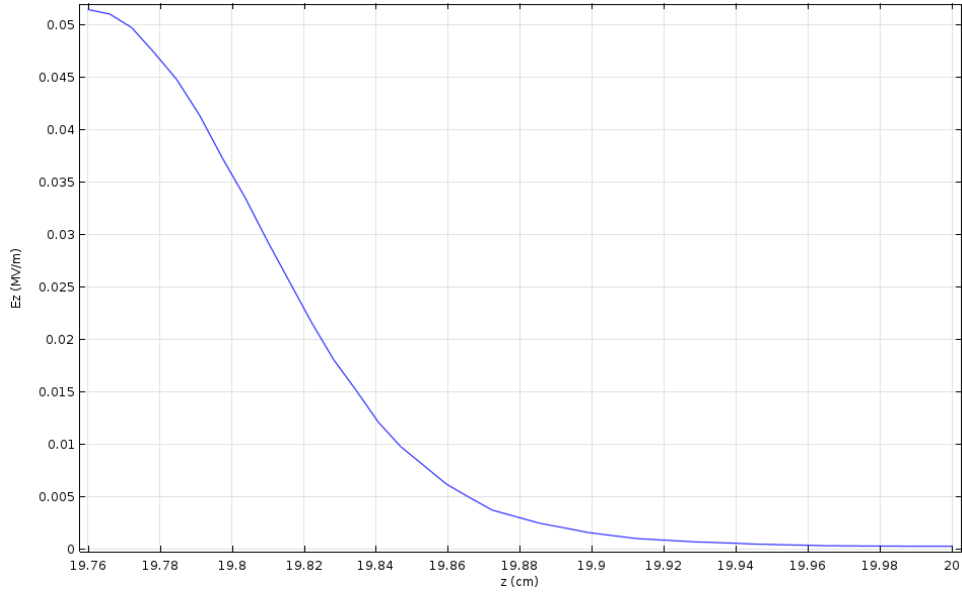
Parameters	SUPERFISH		COMSOL Multiphysics		CST MWS	
Gun Cell Ratio	0.4	0.3	0.4	0.3	0.4	0.3
Frequency [MHz]	1300.9	1300.9	1299.9	1300.7	1300.6	1300.6
E_{peak} , [MV/m]	21.7	22.6	22.5	24.3	22.5	23.8
B_{peak} , [mT]	45.1	45.4	44.4	45.5	44.6	44.7
$B_{\text{peak}}/E_{\text{peak}}$ [mT/(MV/m)]	2.07	2.0	1.97	1.87	1.98	1.88
R/Q [Ω]	931	908	942	910	936	908

APPENDIX B. ADDITIONAL DESIGN RESULTS FOR THE CATHODE ASSEMBLY FOR THE COMPACT SRF ELECTRON SOURCE

This part represents the COMSOL Multiphysics design results and shows the validation with our SUPERFISH results. The results using COMSOL Multiphysics are given in Figures B.1, illustrating the cathode geometry and the electromagnetic field distribution, respectively. As was seen in the design process of the 8.4-cell accelerating structure, the design results using the 2-D codes, SUPERFISH and COMSOL provide again comparable results also for the cathode region.



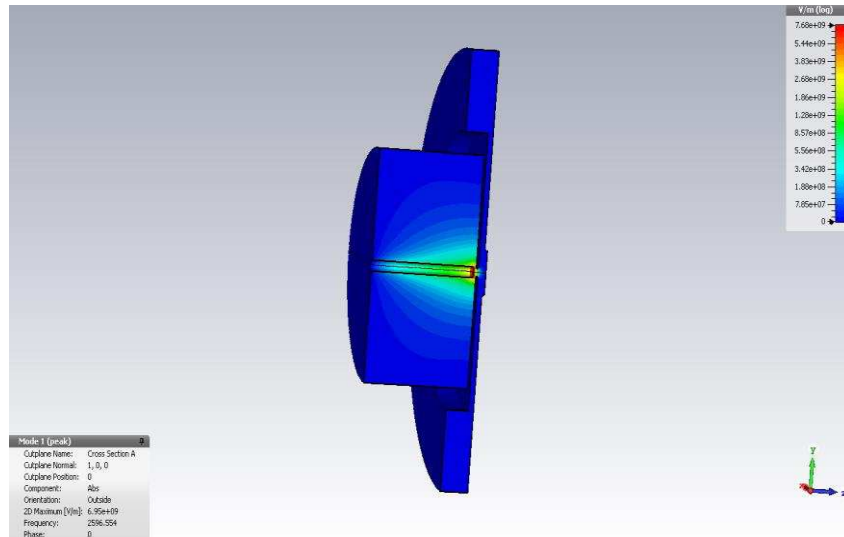
(a)



(b)

Figure B 1: a) The cathode region’s design geometry at 2.6 GHz and field map (in logarithmic scale) using COMSOL Multiphysics. b) The on-axis electromagnetic field distribution of the cathode region’s design geometry

We further validated the 2-D results using CST MWS. These results are shown in Figures B 2, and illustrate that CST provides analogous results as compared to SUPERFISH and COMSOL.



(a)

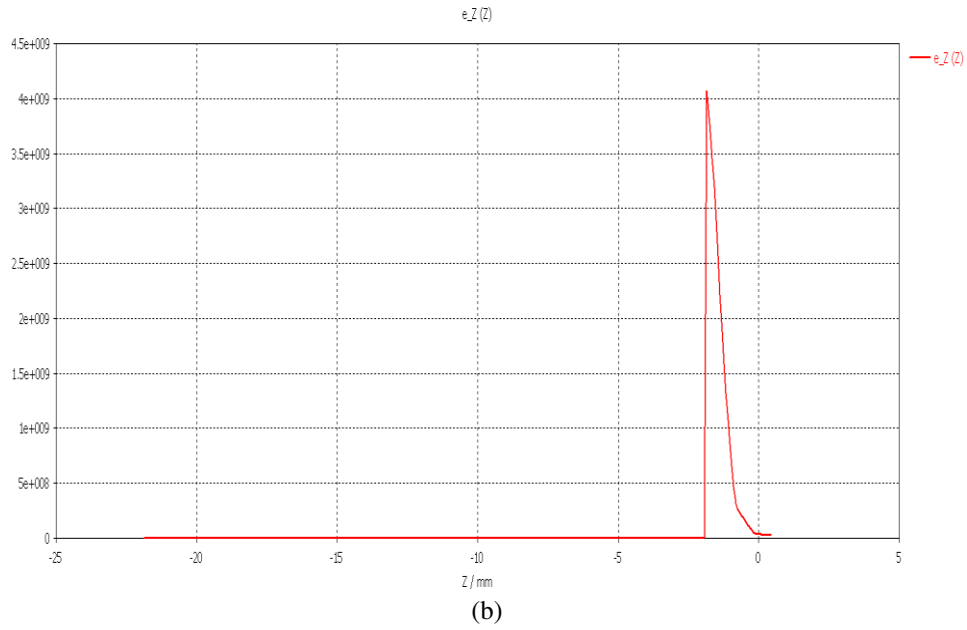
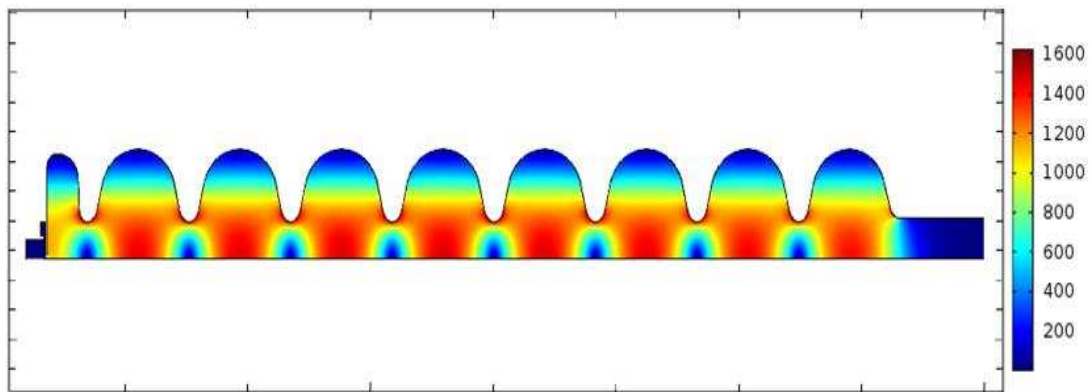


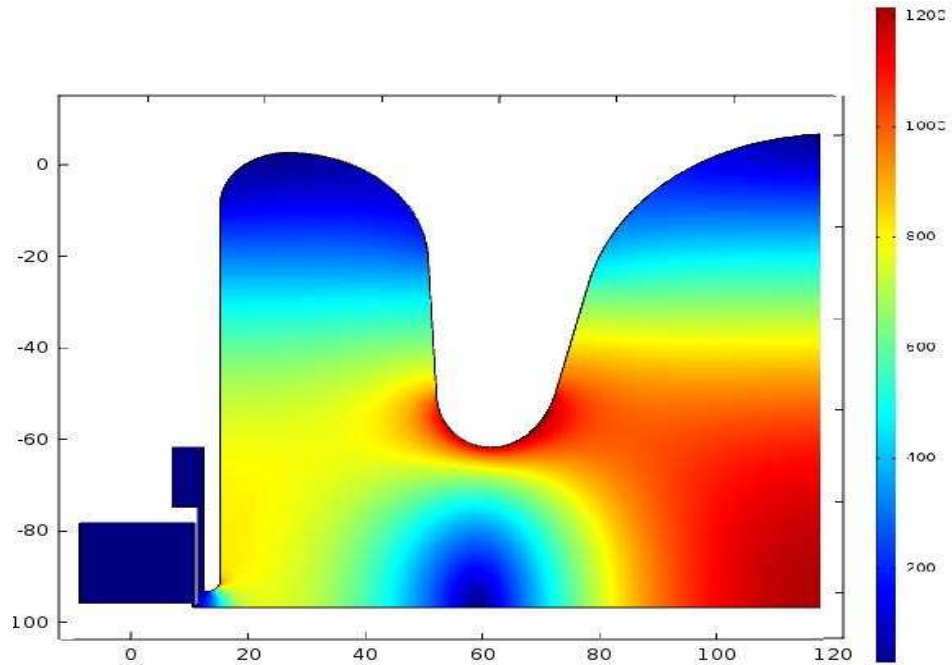
Figure B 2: a) The cathode region's design geometry with the frequency matched to 2.6 GHz and the contour plot of the fields as generated in CST MWS. b) The electromagnetic field distribution of the cathode region's design geometry as shown in Figure 13 as generated in CST MWS.

APPENDIX C. ADDITIONAL DESIGN RESULTS FOR THE INTEGRATED STRUCTURE OF FOR THE COMPACT SRF ELECTRON SOURCE

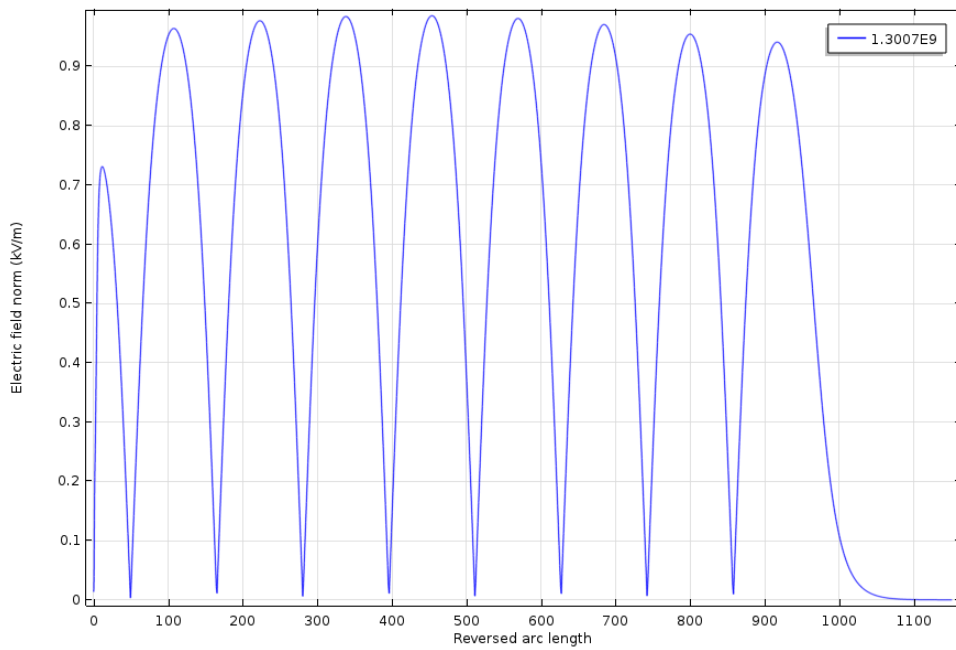
Next, using COMSOL Multiphysics, we find similar results to those found as in SUPERFISH, and shown in Figures 18 – 21). COMSOL also shows that the dominant frequency is 1.3 GHz in Figures C.1. For the simulations of the 2.6-GHz frequency component through the combined structure, there is only negligible propagation to and through the first cell, as can be seen in Figures C.2. The detailed comparison shows good agreement using our previous methods of design validation.



(a)

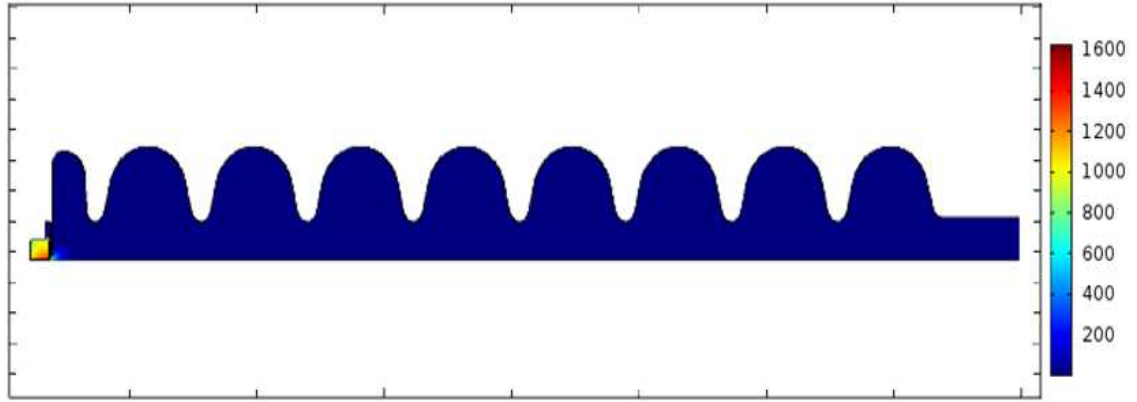


(b)

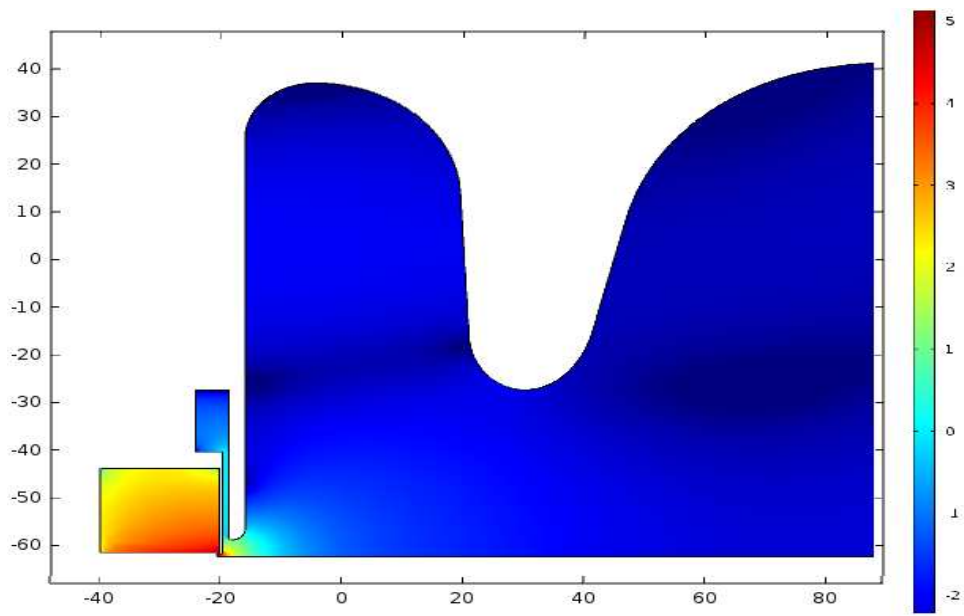


(c)

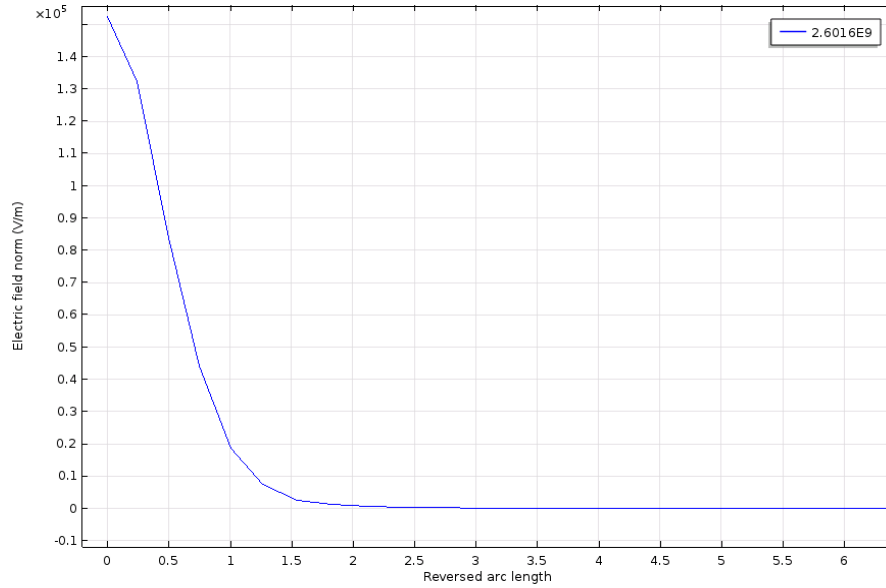
Figure C 1: a) The geometry of the integrated cathode and accelerating structure at a frequency of 1.3 GHz as simulated with COMSOL Multiphysics. b) The magnified view of the cathode and first cell connection c) The field distribution for the design geometry



(a)



(b)



(c)

Figure C 2: a) The geometry and frequency (at 2.6 GHz) of the integrated cathode and accelerating structure as simulated with COMSOL Multiphysics. b) The magnified view of the integrated cathode and first cell in order to enhance the field map in the cathode region as calculated with COMSOL Multiphysics. c) The electromagnetic field distribution of the full system geometry

APPENDIX D. BEAM DYNAMICS SIMULATIONS USING ASTRA FOR THE COMPACT SRF ELECTRON SOURCE

The freely available particle tracking simulation code known as ASTRA (A Space Charge Tracking Algorithm) [ibid, 43] allow us to more fully simulate a thermionic cathode and RF acceleration system of particles. ASTRA allows us to analyze the electron beam properties in detail. This code has been used in many design studies and also validated against their actual performance [55, 56].

ASTRA generates an initial particle distribution using a ‘generator’ file. In this file, possible input parameters can be defined such as particle number, type of distribution and longitudinal extension etcetera. We defined a long bunch length ($769\text{ps} = 1/1.3\text{ GHz}$) in order to see how an ungated thermionic cathode might perform in our design.

This code also uses external field distributions in order to track particles. Therefore, the SUPERFISH field maps for both the cathode assembly region and the 8.3-cell structure was generated and imported into ASTRA. Figure D.1 shows a snapshot in time of the field distribution of the combined geometry (cathode assembly and 8.3-cell accelerator structure) in ASTRA. The DC bias was turned off for this part of the study.

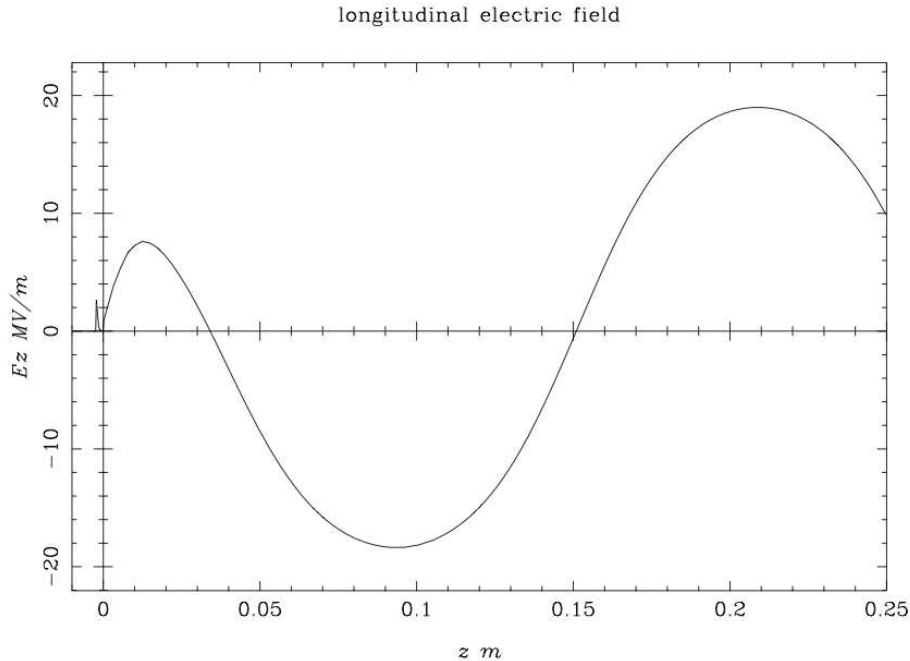
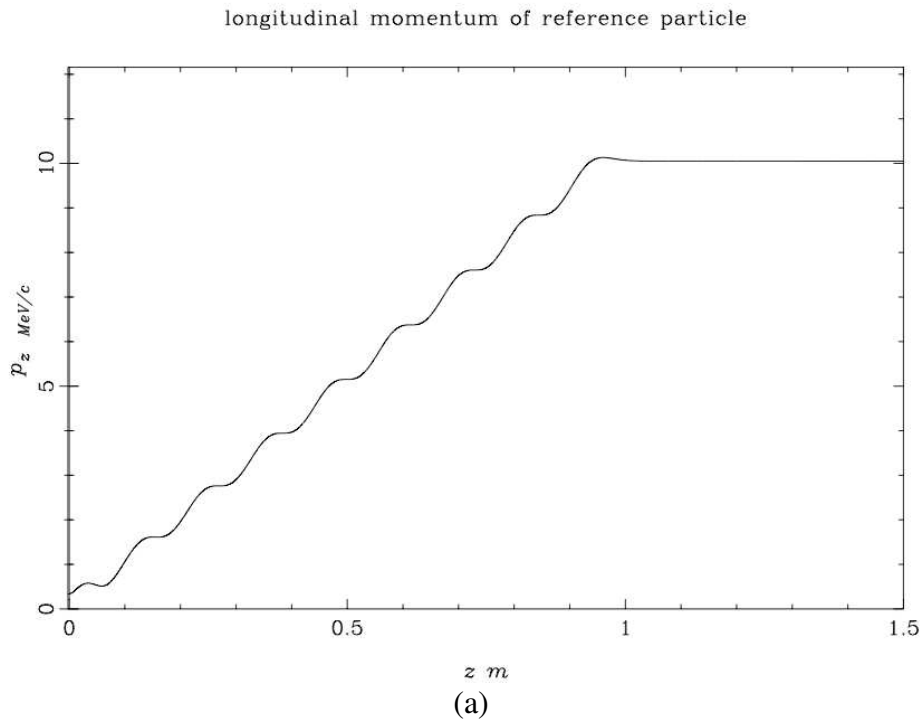


Figure D 1: Transferred SUPERFISH Field Distribution into ASTRA as the external field – zoomed on cathode and first 3 cells field as the cathode field is smaller than the cavity field.

After importing the field distribution, we defined the cathode emission details and start to track the particles generated from the cathode. In the first run we selected an auto-phasing process feature to determine the optimum phases for both the fundamental and the second harmonic frequency structures. The optimum phases of the RF fields were found to be 268 degrees and 221 degrees, respectively. Although these numbers look rather odd at first they are readily understood in terms of how ASTRA handles zero phase. ASTRA starts with a sine-like time profile and so at zero phase the field is zero. It reaches a maximum positive gradient at 90 degrees and a maximum negative field at 270 degree. Negative fields accelerate electrons and since we want as much energy as possible it make sense that the optimal fundamental phase is near 270 degrees. During this process, the reference particle is first tracked through the beam line to check the settings and then it is tracked again starting with a small radial offset. Figure D.2 (a) shows the reference particle's

longitudinal momentum through the full structure. Particle emission was then setup to allow emission at any phase. Figure D.2 (b) shows the average energy of the particles that are generated from the cathode and manage to get accelerated through to the end of the 8.3-cell accelerating structure. Even though the reference particle reaches roughly 10 MeV energy at the end of 9th cell, the average particle energy at the end of the accelerating structure is only 8.14 MeV. The reason for this is that we did not at this time gate the electrons as in the SMASON simulations. The electrons were emitted from the cathode and propagated, if possible and not lost, through the accelerating structure. There is a significant amount of particle loss in the system and a very large energy spread.



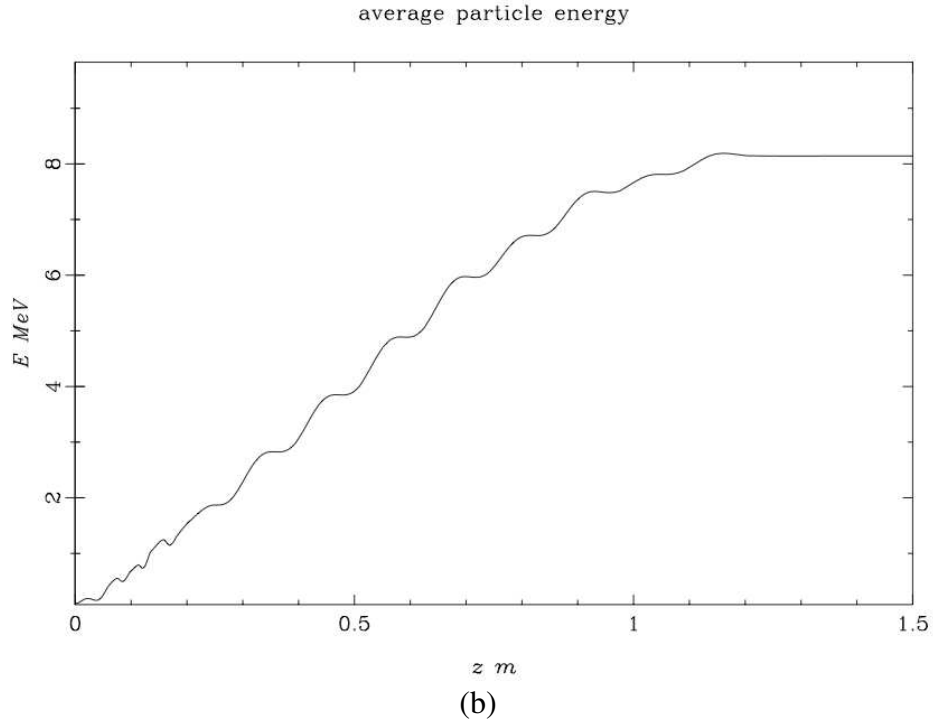
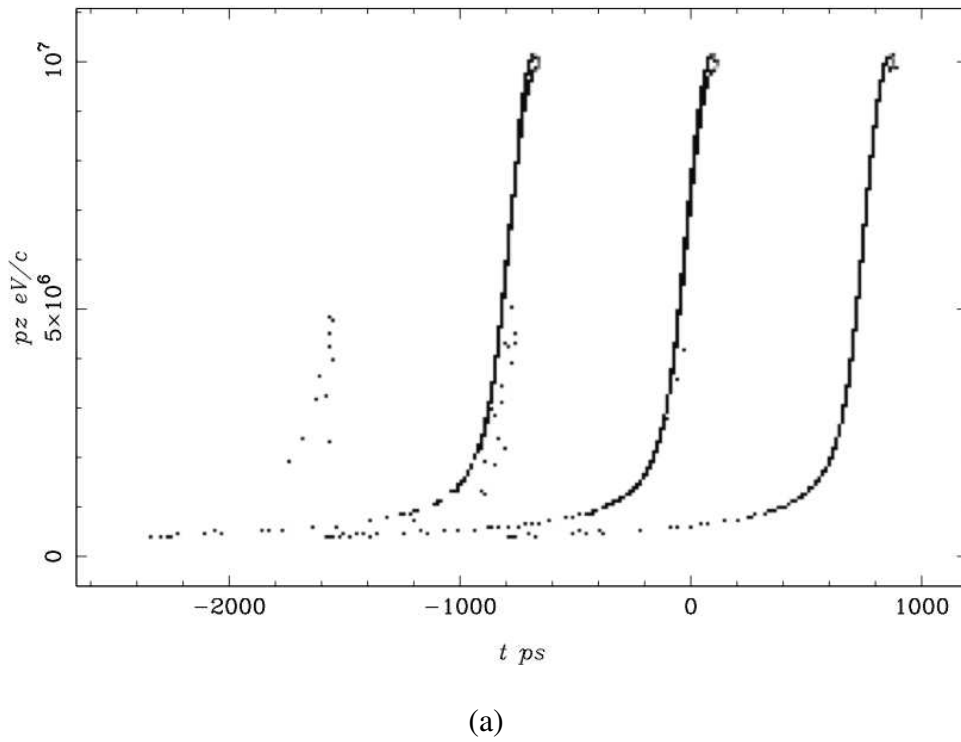


Figure D 2: a) The momentum of the reference particle along the z-axis. The final energy is 10 MeV at the end of 9th cell and b) The average energy of the beam along the z-axis. The final energy is 8.14 MeV at the end of the 9th cell.



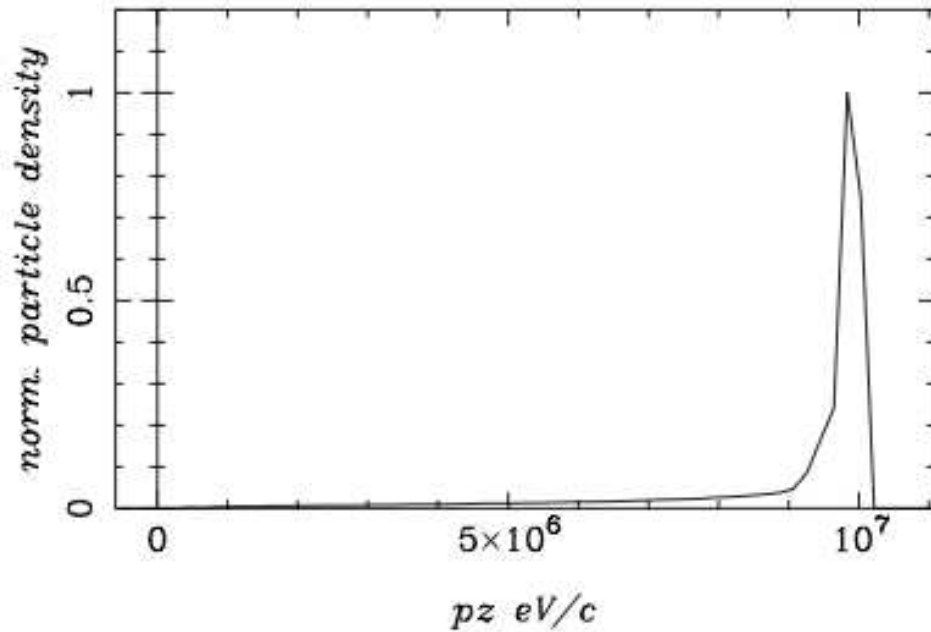


Figure D 3: a) The longitudinal phase space of the bunches at $z=1.5\text{m}$. b) The projection of the first bunch's phase space in Figure D 3 (a).

Figure D 3 shows the longitudinal phase space of a number of sequential bunches emitted off the cathode ($z=1.5$ meters). We used postpro file which is the graphic program in ASTRA and is used to display phase space plots of particle distributions and allows a detailed analysis of the phase space distribution to get this plots. According to this file, the reference particle is always at $t = z = 0$. Then all the particles coordinate are referred with respect to the reference particle. As the particle moves, the reference particle moves, but the convention is to refer to its position (or time) as zero. The plot shows the results at $z=1.50$, which is actually the laboratory position of the reference particle. So $t = 0$ on the plot shows to 1.5 m from the cathode position. These bunches have a maximum ~ 10 MeV energy, however, with a very large energy spread.

Clearly even though there is energy gain at the end of the structure, we still need to gate the field to prevent the large particle loss and large energy spread. Therefore, as a next step in our simulations, we studied gating the field inside the structure as we did in SMASON. The results are given in Figure D 4 and D 5.

Figure D 4 shows the average energy of the particles that are generated from the cathode and accelerated through the 8.3-cell accelerating structure with space charge turned on but this time with gating. Since we gate the field before the particles go through the accelerating structure, the average energy is now 9.49 MeV with virtually no particle loss.

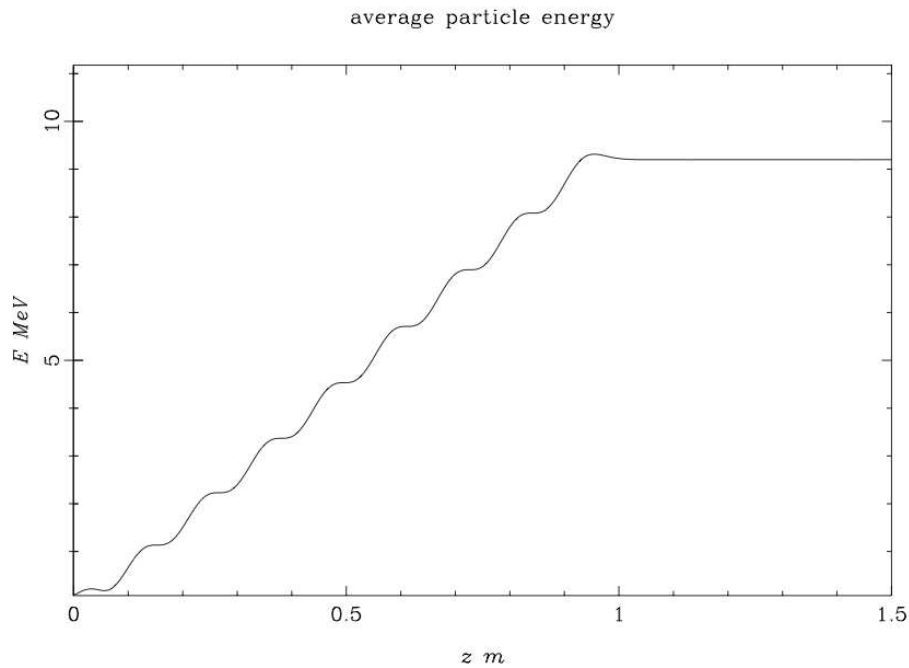


Figure D 4: The average energy of the beam along the z-axis. The final energy is 9.49 MeV at the end of 9th cell.

Figure D 5 shows the longitudinal characteristics of the bunches at the end of the accelerator but this time when we gate the fields and have space charge turned on. These bunches reach ~10 MeV

energy (as can be seen in Figure D 5 (b)) with a very small energy spread. As can be seen, when we gate the field, we can achieve higher average energies than without gating as the energy spread is a significantly smaller, and there appears to be no particle loss.

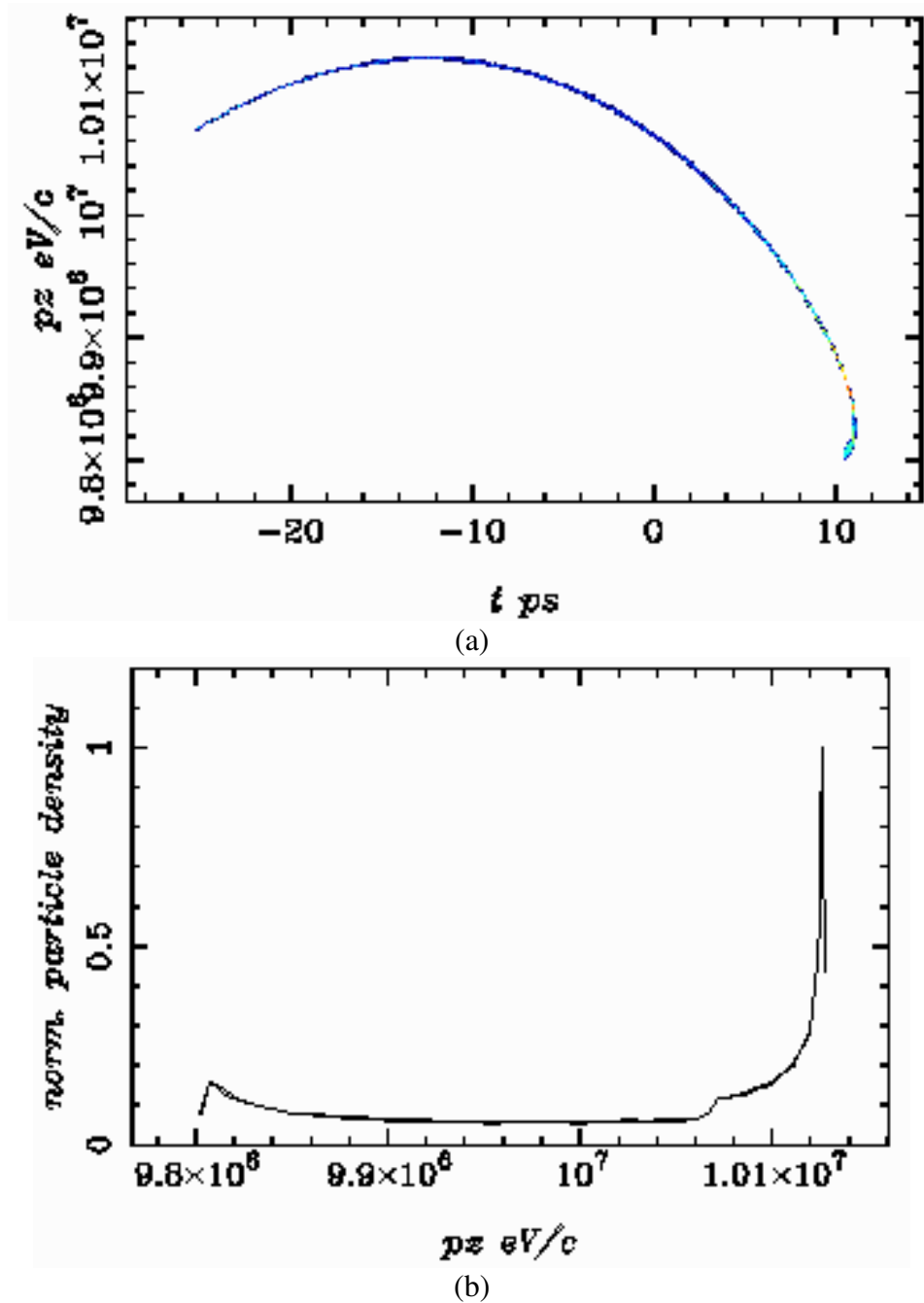


Figure D 5: a) The longitudinal phase space of the bunches, b) projection of the longitudinal momentum of Figure D 5 (a).